Inaugural Dissertation

for

obtaining the Doctoral Degree

of the

Combined Faculty of Mathematics, Engineering and Natural Sciences

of the

Ruprecht - Karls - University

Heidelberg

Presented by:

M.Sc. Daniela Avilés Huerta

Born in:

Mexico City, Mexico

Oral Examination:

9th of October of 2023

Dual Ribosome Profiling (DualRP) Uncovers Metabolic Vulnerabilities from Multiple Populations of the Tumor Microenvironment in Triple-Negative Breast Cancer

Referees: apl.Prof.Dr. Stefan Wiemann

Dr. Wilhelm Palm

Zusammenfassung

Triple-negativer Brustkrebs (TNBC) ist der aggressivste Brustkrebs-Subtyp mit begrenzten zielgerichteten Therapiemöglichkeiten. Die dichte Bevölkerung der Tumormikroumgebung (TME) mit Stroma- und Immunzellen spielt eine zentrale Rolle bei der metabolischen Neuprogrammierung von Krebs. Daher bietet die Aufklärung der wichtigsten metabolischen Schwachstellen der TME neue therapeutische Perspektiven für TNBC. In dieser Studie stelle ich die Verwendung von Dual Ribosome Profiling (DualRP) als neuartigen Ansatz zur Aufdeckung zelltypspezifischer Stoffwechsellimitationen in der naiven TME vor. Um DualRP zu etablieren, wurden zunächst Systeme zur ribosomalen Fluoreszenzmarkierung in TNBC-Zellen und Fibroblasten entwickelt und validiert. Zweitens zeigte DualRP deregulierte Signalmechanismen und metabolische Interaktionen in beiden gleichzeitig interagierenden Zellpopulationen auf, die *in vitro* und *in vivo* validiert wurden. Drittens bestätigten transgene DualRP-Mausmodelle die metabolische Anfälligkeit von T-Zellen in TNBC-Tumoren. Um schließlich die metabolischen Schwachstellen von TNBC für die Therapie auszunutzen, wurde die Kombination aus Checkpoint-Inhibition und Ernährungseinschränkung *in vivo* angewendet. Insgesamt stellt mein Projekt einen robusten Ansatz zur gleichzeitigen Untersuchung metabolischer Schwachstellen in mehreren Kompartimenten der TME dar.

Abstract

Triple negative breast cancer (TNBC) is the most aggressive breast cancer subtype with limited targeted therapy options. Stromal and immune cells densely populate the tumor microenvironment (TME) and are central players in the metabolic reprogramming of cancer. Therefore, elucidating the key metabolic vulnerabilities in the TME, offers new therapeutic perspectives for TNBC. In this study, I introduce the use of Dual Ribosome Profiling (DualRP) as a novel approach for uncovering cell-type specific metabolic limitations in the naïve TME. Firstly, to establish DualRP, systems of ribosomal fluorescent tagging in TNBC cells and fibroblasts were developed and validated. Secondly, DualRP revealed deregulated signaling mechanisms and metabolic interactions in both cell populations interacting simultaneously, which were further validated *in vitro* and *in vivo*. Thirdly, DualRP transgenic mouse models confirmed the metabolic vulnerabilities of T cells in TNBC tumors. Lastly, to exploit the metabolic vulnerabilities of TNBC for therapy, the combination of checkpoint inhibition and dietary restriction was applied *in vivo*. Collectively, my project presents a robust approach to study metabolic vulnerabilities in multiple compartments of the TME simultaneously.

Table of Contents

I. Introduction

1.1 Breast Cancer

1.1.1 Classification

Breast cancer (BC) is the leading cause of cancer related deaths in women and the fifth most lethal cancer type[1,2]. As the most commonly diagnosed cancer worldwide[3,4], BC burden by 2040 is estimated to increase to over 3 million new cases and 1 million deaths per year[3].

BC comprises different tumor subtypes with high heterogeneity at the cellular and molecular levels. A commonly used classification is based on the expression of hormone receptors and the epidermal growth factor receptor 2 (HER2), through which three categories are defined: oestrogen and/or progesterone receptor (ER/PR) positive, HER2 positive and triple negative breast cancer (TNBC)[5,6].

Tumors expressing ER/PR receptors generally respond well to hormonal interventions[7], while HER2 positive tumors tend to respond effectively to anti-HER2 therapy[8]. On the other hand, TNBC tumors lacking the expression of the three receptors are highly aggressive and have limited targeted-therapy options[9,10].

1.1.2 Triple Negative Breast Cancer

TNBC accounts for more than 15–20% of all breast cancers and encompasses different subtypes with characteristic metastatic patterns and poor prognosis[9,11,12]. At the transcriptional level, TNBC can be classified into four subtypes: two basal subtypes known as BL1 and BL2, a mesenchymal subtype M, and a luminal androgen receptor subtype[13]. Additionally, based on molecular heterogeneity, TNBC can be further categorized into six different subgroups: immunomodulatory, luminal androgen receptor expression, mesenchymal stem-like, mesenchymal-like, basal-like, and unstable[14,15]. Each TNBC-subtype harbors specific transcriptomic and genetic alterations that might be exploited for therapy[16]. For instance, germline mutations in the breast cancer- susceptibility protein type 1 or 2 (*BRCA1/2)* occur in ~10% of TNBC patients and serve as biomarker for DNA-targeting cytotoxic agents such as platinum-

based agents and poly(ADP-ribose) polymerase (PARP) inhibitors[17]. Conversely, driver alterations in genes of the phosphoinositide-3-kinase (PI3K)/AKT pathway occur in ~25% of TNBCs and provide sensitivity to PI3K pathway inhibitors[18]. Unfortunately, only a small proportion of TNBC patients are treatable based on oncogenic driver heterogeneity[19].

On the other hand, TNBC has the highest proportion of tumor-infiltrating lymphocytes (TILs) compared to other BC subtypes[20]. Within the tumor, TILs express the programmed cell death protein 1 (PD1) that binds to the PD1-ligand in cancer cells. This interaction leads to decreased T cell effector function and an increased immunosuppressive microenvironment[21]. In this context, the use of immune checkpoint inhibition yields promising results in patients with early-stage as well as advanced TNBC[22,23]. Moreover, there is a growing interest on understanding the complex interactions between cancer cells and other cell types within tumors[24,25], which may hopefully bring new therapeutic perspectives for TNBC.

1.2 The Tumor Microenvironment

1.2.1 Cellular and exogenic factors

The tumor microenvironment (TME) is a dynamic ecosystem composed of cancer cells, immune cells, and stromal cells (**Figure 1**). Together, they play a crucial role in promoting tumor development, metastasis, and therapy resistance[26,27]. The cellular components of the TME belong to distinct lineages of the surrounding host tissue, forming an intricate network that influences tumor behavior[28]. From the hematopoietic lineage, T cells, B cells, neutrophils, natural killers (NK) and macrophages primarily contribute to the tumor immune response[29]. On the other hand, the mesenchymal lineage including fibroblasts, adipocytes, endothelial cells, and pericytes, provides support for tumor growth and vascularization[30]. Together, these cellular components can make up to 50% of the total mass of a solid tumor[31,32]. The presence of exogenic factors like the extracellular matrix (ECM), chemokines, cytokines and metabolites, sustain the vascularized tumorigenic niche with gradients of oxygen, pH, and nutrient availability[27].

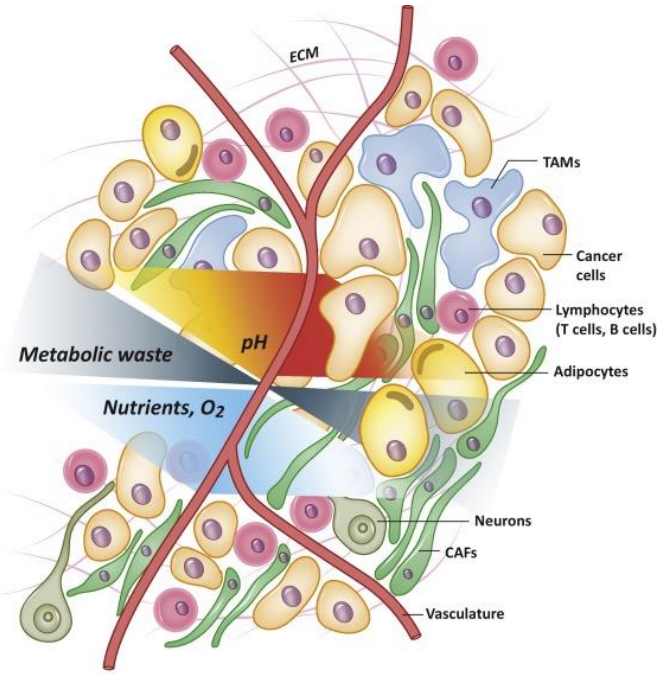

Figure 1 | Cellular and exogenic factors of the Tumor Microenvironment (TME). Cellular and exogenic components contribute to the deregulated metabolic profile of tumors. The TME comprises the heterogeneous distribution of different cellular along gradients of nutrients, oxygen and waste. CAF, cancer-associated fibroblast; TAM, tumor-associated macrophages[27].

1.2.2 Metabolic reprogramming in the Tumor Microenvironment

Reprogramming of cell metabolism is defined as a hallmark of cancer[33]. The intratumoral metabolic crosstalk provides cancer cells with selective advantages to enhance proliferation and survival[34]. The competition for nutrients in the TME, rewires multiple signaling pathways regulating the metabolism and trafficking of nutrient transporters. For example, master regulators such as c-Myc, hypoxia-inducible factor (HIF)-1α, AMP-activation protein kinase (AMPK), and mammalian target of rapamycin (mTOR), modulate the uptake of nutrients and the activity of several metabolic enzymes in the TME[35–38].

Furthermore, alternative mechanisms are activated in the TME to generate intracellular sources of nutrients under limiting conditions. One such mechanism is autophagy, a highly conserved catabolic process that involves the degradation of intracellular components in the lysosome[39]. Autophagy enables the turnover of

macromolecules and organelles, allowing tumors to counteract nutrient and oxidative stress[40].

The deregulated metabolic profile of tumors deeply impairs effective antitumor immunity[41]. Hence, characterizing the metabolic interplay of different cells in the TME can reveal key vulnerabilities of cancer[42].

1.2.2.1 Cancer cells

Cancer cell proliferation demands a higher rate of energy supply and building blocks compared to other cells in the TME[43]. Following malignant transformation, cancer cell survival is facilitated by the reprogramming of the metabolism[44]. This reprogramming is characterized by enhanced glycolysis and glutaminolysis, *de novo* lipid biosynthesis and alterations in amino acid metabolism[44–47].

As a first adaptation, the majority of glucose consumed by tumors is fermented to lactate, which is defined as aerobic glycolysis[48]. Unlike carbohydrate fermentation in response to oxygen limitation, aerobic glycolysis is characterized by high levels of fermentation even in the presence of oxygen[48,49]. This phenomenon, commonly known as the Warburg effect, occurs despite the presence of functioning mitochondria[49]. While aerobic glycolysis is less efficient for ATP production compared to oxidative phosphorylation[50], it has potential benefits that impact the TME. For example, the high rates of glycolysis in cancer cells limit the availability of glucose for the activity of tumor-infiltrating lymphocytes (TILs)[51]. Additionally, lactate present in the TME can mediate the polarization of tumor-associated macrophages (TAMs) towards the pro-tumorigenic M2-phenotype[52].

Furthermore, cancer cells have a strong dependence on lipids and cholesterol, which is compensated by their enhanced uptake from the environment and the activation of *de novo* lipid biosynthesis[47,53]. Lipid mediators, such as Prostaglandin E2 (PGE2) and fatty acids (FAs), are also known to contribute to the oncogenic signaling in the TME[54,55].

Cancer cells also heavily rely on glutamine as a nitrogen donor for the synthesis of lipids, essential amino acids, and nucleotides[45,56]. The dependency on glutamine

drives the process of glutaminolysis, which generates α-ketoglutarate, a crucial fuel for the tricarboxylic acid (TCA) cycle and energy production[57]. In addition to glutamine, the metabolism of other amino acids, including arginine, tryptophan, glycine, serine, and the branched-chain amino acids (BCAA: leucine, isoleucine, and valine) plays a pivotal role in tumorigenesis[58–62].

1.2.2.2 Fibroblasts

Fibroblasts within the TME, commonly referred as cancer associated fibroblasts (CAFs), are a major component of the tumor stroma[63]. CAFs may be derived from epithelial cells, endothelial cells, cancer stem cells, adipocytes, pericytes, or stellate cells[30]. In tumors, fibroblasts transform into a highly synthetic and metabolically active population that promotes the growth and invasion of cancer cells by the secretion of growth factors and pro-inflammatory mediators[64]. For instance, CAFs serve as the main producers of ECM components such as collagens, fibronectin, and matrix metalloproteinases[65]. Moreover, CAFs secrete cytokines, chemokines, growth factors, and exosomes, creating a rich milieu that promotes tumor progression and influences therapy response[64,66,67].

In the TME, CAFs produce high-energy nutrients such as lactate and ketones, via the upregulation of aerobic glycolysis and autophagy[68,69]. These nutrients provide energy for mitochondrial biogenesis and oxidative metabolism in cancer cells, which has been called the “reverse” Warburg effect[70].

In BC and other cancer types, the enrichment of CAFs correlates with poor patient survival and lymph node metastasis[71,72]. Surprisingly, CAFs also act as mediators of immunosuppression in the TME[73,74]. In the case of TNBC, CAFs may facilitate the recruitment of regulatory T cells[75] or induce the polarization of TAMs[76].

1.2.2.3 T cells

T cells in the TME, also referred as tumor infiltrating lymphocytes (TIL), reshape the immune microenvironment by orchestrating tumor immunity and therapy response[31,77]. There are different populations of T cells that exert various effects on the TME. First, CD8+ cytotoxic T cells recognize tumor associated antigens expressed on cancer cells to target cancer cell destruction[78]. Therefore, presence of cytotoxic T cells in the TME is often correlated with a positive prognosis in cancer patients[79–81]. In addition to their tumor-killing function, cytotoxic T cells suppress tumor angiogenesis by the secretion of interferon gamma (IFN-γ)[82]. Second, CD4+ T cells have the ability to differentiate into various subtypes that coordinate opposing immune responses in the TME[83]. For instance, T helper 1 (Th-1) cells, a subtype of CD4+ T cells, exhibit proinflammatory properties and provide support to CD8+ cells through the secretion of interleukin-2 (IL-2) and IFN-γ[84]. In contrast, regulatory T cells (Tregs) suppress inflammatory responses and contribute to tumor progression[85].

In terms of metabolic reprogramming, effector T cells upregulate glycolysis and use the metabolic intermediates of the TCA cycle to synthesize proteins, lipids, and nucleic acids[86,87]. In particular, helper CD4+ T cells enhance both glycolysis and oxidative phosphorylation, whereas CD8+ T cells mainly activate glycolysis making them more sensitive to glucose withdrawal[86,88].

The high demand for glucose and glutamine in cancer cells promotes a state of nutrient deprivation in T cells, leading to T cell exhaustion, tolerance to stimulation (anergy), and apoptosis[89]. The glucose-deprived TME inhibits the proliferation and cytokine production in CD8+T cells and reduces T cell glycolysis by blocking the PI3K/Akt/mTOR pathway[90]. Contrastingly, reduced glucose and elevated lactate benefit the mitochondrial oxidative metabolic pathways in Tregs to promote an immunosuppressive environment[91].

T cells are also affected by the competition for certain amino acids in the TME. For example, arginine depletion from arginase-I expression in the acidic TME, inhibits T cell activation and proliferation[92]. Similarly, tryptophan depletion by the expression of

indoleamine 2,3-dioxygenase (IDO) in cancer cells, results in the accumulation of the oncometabolite kynurenine in the TME that impairs T cell proliferation[93,94].

1.3 Ribosome Profiling

1.3.1 Principles

Ribosome profiling, also known as Ribo-seq, is a deep sequencing-based approach that enables global translation examination at nucleotide (nt) level resolution[95]. The principle behind Ribo-seq is based on the fact that translating ribosomes shield approximately 30 nt of mRNA from nuclease degradation. By mapping these ribosome-protected fragments (RPFs) to the genome, the precise position of the translating ribosome within specific codons can be determined[96]. Moreover, by quantifying ribosome-protected fragments (RPFs) on a specific transcript, it is possible to estimate the rate of protein synthesis[97]. The combination of Ribo-seq and mRNA sequencing data, allows the direct comparison between the rate of protein synthesis and the steady-state transcript levels, that together provide insights into the *in vivo* translation efficiency[96].

In Ribo-Seq protocols cells are rapidly harvested and lysed under conditions that are expected to preserve the original ribosome positioning[95]. This is achieved in the presence of cycloheximide, harringtonine, or by snap freezing the cells with liquid nitrogen[98]. The cell lysate is then subjected to nuclease footprinting using RNases with either broad-range specificity (e.g., RNase I) or nucleotide-specificity (e.g., RNase T1, A)[99]. As ‘gold standard’, ribosome fractionation is perfomed by ultracentrifugation through a sucrose density gradient. Nonetheless, Ribo-seq has also been adapted to retrieve cell-type–specific expression of tagged ribosomal proteins, such as translating ribosome affinity purification (TRAP)[100] and RiboTag[101].

For RPF recovery, the total RNA from ribosomes is size-selected from a denaturing gel. For next-generation sequencing (NGS) library preparation, the 3' ends of the RPFs are dephosphorylated using T4 PNK, allowing for the ligation of a pre-adenylated DNA linker (barcode) with T4 Rnl2(tr) K227Q. The resulting RNA-DNA hybrid molecule serves as a template for reverse transcription, and the full-length

cDNA products are purified using gel-based methods. The single-stranded cDNA can be circularized using CircLigase to increase amplification efficiency. Finally, the circularized product is amplified through PCR, resulting in a double-stranded DNA library[95,96,102].

1.3.2 Diricore

Differential Ribosome Codon Reading (diricore) is an analysis tool to unravel cell vulnerabilities for specific amino acids when applied to Ribo-Seq data[103]. In principle, the global occupancy of ribosomes in specific codons is used to detect alterations in the availability of certain amino acids for protein synthesis. Diricore is based in two complementary analyses. First, subsequence analysis to examine the abundance of codons at position 9, 12 and 15, corresponding to the E (exit), P (peptide bond), and A (tRNA recruitment and reading codon sites) of RPFs. Here, the specific accumulation of ribosomes in position 15 suggests the limitation in the corresponding amino acid (**Figure 2C**). The second analysis is on RPF density, where every instance of a codon throughout the transcriptome is analysed to inspect the local RPF 5′-end density surrounding that codon. With diricore, the accumulation of RPF in a particular codon pinpoints a potential limitation of the corresponding amino acid that can be exploited to impair cancer cell growth[103–105].

1.3.3 Dual Ribosome Profiling

A big proportion of the current techniques to study metabolism in heterogeneous cell populations, involve the disruption of the native cell interactions by flow cytometry or the use of antibody-based arrays coupled to mass spectrometry[106–109]. To overcome artifacts from tumor dissociation, Dual Ribosome Profiling (DualRP) is designed to elucidate cell-type specific metabolic limitations in the naïve TME.

In DualRP, the ribosomes of two different cell types are tagged with distinct fluorophores to retrieve the cell-type specific translatome from the heterogenous population (**Figure 2A**).

Ribosomal tags are incorporated by paired CRISPR-Cas9 genome editing or by its overexpression via lentiviral transduction. One main advantage of the CRISPR–Cas9 nickase method is the high homozygosity efficiency[110]. Here, a Cas9D10A nickase mutant and paired gRNAs are used for the introduction of DNA double-stand breaks in the ribosomal protein locus, while the fluorescent marker is integrated using the DNA template from a donor plasmid via homology-directed repair (HDR)[110].

Notably, DualRP allows not only simultaneous analysis of gene expression in two interacting cell populations, but also holds potential to uncover metabolic limitations in tumors in combination with diricore (**Figures 2B-C**).

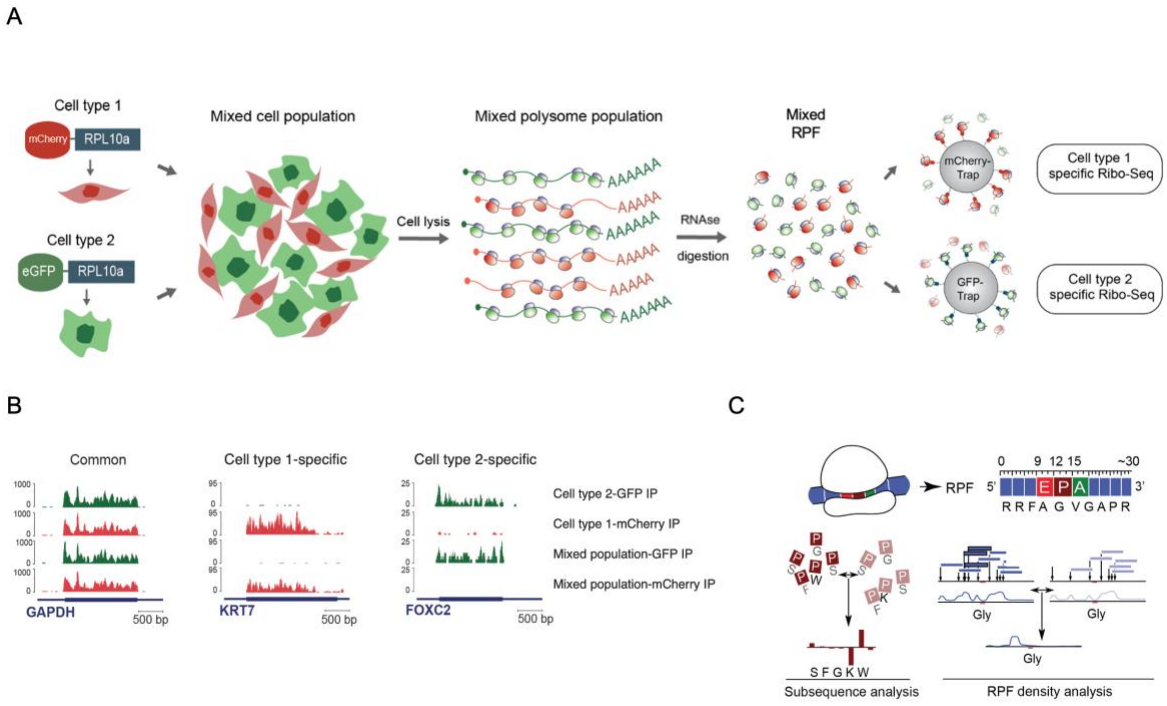

Figure 2 | Dual Ribosome Profiling (DualRP) for cell type-specific isolation of ribosomes in a mixed population. (**A**) Schematic representation of DuaRP shows the ribosomes of two different cell types tagged with eGFP and mCherry in the ribosomal protein L10a (RPL10a). Both cell populations are mixed, lysed, and the ribosomes from each cell type are immunoprecipitated using highly specific nanobodies. Ribo-seq libraries are subsequently prepared from recovered ribosome protected fragments (RPF). (**B**) Discrimination of gene expression data from a mixed population of cells with DualRP. (**C**) Differential ribosome codon reading (diricore). The RPF positions 9, 12, and 15 from the 5'-end of the RPF corresponding to the E (exit), P (peptide bond), and A (tRNA recruitment and reading codon) sites of the ribosome are indicated. In diricore two complementary analyses are performed: to the left subsequence analysis, the codons at 9, 12, and 15 nt of the 5'-ends of RPFs are examined; and to the right, RPF density analysis of every instance of a codon throughout the transcriptome provides the local RPF 5'-end density surrounding that codon[103].

II. Aims of the project

In order to dissect the cellular and metabolic interactions in the tumor microenvironment of triple-negative breast cancer the specific objectives of my project are:

- To generate Dual-RP tailored models of TNBC *in vitro* and *in vivo*.
- To study the signaling mechanisms in cancer cells and fibroblasts promoting cancer survival.
- To validate the cell interactions in the TME of solid tumors using mouse xenografts.
- To investigate the interactions between T cells and cancer cells in mouse genetic models and during checkpoint blockade.
- To exploit the metabolic vulnerabilities of tumors under checkpoint blockade in combination with dietary restriction.

III. Materials and Methods

3.1 Materials

Table 1. Devices and Instruments

Resource	Source
Adventurer Analytical Scale	Otthaus
Benchtop Centrifuge 5424r	Eppendorf
Digital Magnetic Stirrer D-6010	Neolab
Dry Block Heater Btd	Grant
Gel Doc Xr+	Biorad
Incubator Bbd6220	Heraeus
Innova U725	New Brunswick Scientific
Mediline Lcexv 4010	Liebherr
Mini-Vac-Power	Peqlab
Multifuge X312	Thermo Scientific
Nextseq2000	Illumina
Nu-437-600e	Nuaire
Powerpac Hc	Biorad
Precision Scale Ewj 300	Kern
Quantstudio 5rt Qpcr System	Thermo Fisher Scientifc
Qubit3	Invitrogen
Centrifuge Rotofix 32a	Hettich
T Professional Thermocycler	Biometra
T100 Thermal Cycler	Biorad
Thermomixer Comfort	Eppendorf
Trans-Blot Turbo	Biorad
Vortex Genie 2 G560e	Scientific Industries
Waterbath	Memmert
Dynamag Magnetic Rack	Thermo Fisher Scientifc
Ultracentrifuge Optima Xpn100	Beckman Coulter
Swinging Bucket Rotor Sw41 Ti	Beckman Coulter
Oyssey Clx Imaging System	Licor
FACS Canto II	Bd Biosciences
FACS Aria III Cell Sorter	Bd Biosciences
Mojosort Magnet	Biolegend

Leica Tcs Sp5 Confocal Microscope	Leica
Mikro Dismembrator S	B.Braun Biotech
Multiskan Fc	Thermo Scientific
Biophotometer	Eppendorf
Pipetboy	Integra Biosciences
Single Channel Pipettes	Gilson
Multichannel Lite Xls	Rainin
Single Channel E4 Xls Electronic	Rainin
Zeiss Axio Cell Observer	Zeiss
Nanodrop One C	Thermo Scientific
Incucyte S3	Essen Bioscience
Dual Lens System V850 Pro Scanner	Epson
Barnstead Genpure Xcad Plus Uv/Uf	Thermo Scientific

Table 2. Chemical reagents

Reagent	Source	Identifier
4x Laemmli Buffer	BioRad	1610747
Acrylamide 40%, Bis Solution, 19:1	BioRad	1610144
Acrylamide 40%, Bis Solution, 37.5:1	BioRad	1610148
Agar	Sigma Aldrich	A5306-250G
Agarose	Sigma Aldrich	A9539-500G
Ampicillin	Sigma Aldrich	A9518-25G
APS	Sigma Aldrich	A3678-100G
Boric acid	Sigma Aldrich	31146-2.5kg
Chloroform	VWR	22711.260
CHX	Sigma Aldrich	C7698-5G
cOmplete PI	Sigma Aldrich	11873580001
Crystal Violet	Santa Cruz	60662-33-1
DMSO	Sigma Aldrich	D186309-100ML
DTT	Sigma Aldrich	D0631-10G
EDTA	Sigma Aldrich	EDS-1kg
Ethanol	Sigma Aldrich	32221-2.5L-M
Formaldehyde 37%	Merck	252549
G418	Sigma Aldrich	A1720-5G

Glacial acetic acid	Fisher Chemical	A/0400/PB15
Glycerol	Sigma Aldrich	G6279-1L
Glycine	Sigma Aldrich	G8790-100G
GlycoBlue	Thermo Fisher Scientific	AM9516
KCl	Sigma Aldrich	P5405-250g
Beta-Mercaptoethanol	Sigma Aldrich	M6250-250ML
Methanol	Fisher Scientific	67-56-1
$MgCl_2$	Sigma Aldrich	M2393-500g
NaCl	Fisher Chemical	S/3160/60
NP40	Sigma Aldrich	74385-1L
Propan-2-ol	VWR	20842.330
SDS 20 % solution	Sigma Aldrich	05030-1L-F
Skim Milk Powder	Sigma Aldrich	70166-500G
Sulfuric acid 62 %	VWR	7664-93-9
SuperAse In	Thermo Fisher Scientific	AM2694
SYBR Gold	Thermo Fisher Scientific	S11494
TEMED	Sigma Aldrich	T7024-25ml
TRI Reagent	Zymo Research	R2050-1-200
Tris	Acros Organics	167620010
Triton X-100	Sigma Aldrich	T8787-250ml
Tryptone	Carl Roth	8952.3
Tween 20	Sigma Aldrich	P1379-250ML
UltraPure DNase/RNase-Free Water	Life Technologies	10977035
Yeast extract	Gerbu Biotechnik	1133.0500
Sucrose	Sigma Aldrich	S7903-1KG
Hydrochloric acid	VWR	1.09057.1000P
Sodium bicarbonate	Serva	30180.02
Retronectin	Takara	T100A
PEI max	Polyscience	24765-1
Polybrene	Santa Cruz	sc-255611
Puromycin	Sigma	P8833
Blasticidin	Santa Cruz	sc-495389

Table 3. General lab supplies

Product	Source	Identifier
Nitrocellulose 0.45 µm	Biorad	1620115
Amicon-15 columns	Merck	UFC900308
25 G x 4/5'' needle	Medoject	CH25045
Soft-Ject-F 1ml	B.Braun	SJ-9161406
Cell strainer 10 mm	PluriSelect USA	43-50010-50
Open-Top Thinwall Ultra-Clear Tube	Beckman Coulter	344059
X12 Bottle-Top Filter 0.2um PES	Fisher Scientific	10300461

Table 4. Bacterial strains

Product	Source	Identifier
Dh5α	Donated by Bethune Group (BZH, Heidelberg University Biochemistry Center)	18265017
Stbl3	Donated by Dr. Sun Chong at DKFZ	-

Table 5. Recombinant DNA

Plasmid	Source	Identifier
plentiCRISPR v2	Addgene	52961
pMSCV-U6sgRNA(BbsI)-PGKpuro2ABFP	Addgene	102796
pMDLg/pRRE	Addgene	12251
pRSV-Rev	Addgene	12253
VSV.G	Addgene	14888
pCDHblast-OVA	Loayza-Puch Lab	FLP229
px335-U6_Chimeric_BB-CBhSpCas9n(D10A)+ RPL10A_sgRNA1	Loayza-Puch Lab	FL010
pX335-U6-Chimeric-BB-CBh-hSpCas9nsgRNA-RPL10a#4	Loayza-Puch Lab	FL032
pBlue SK GFP-RPL10a	Loayza-Puch Lab	FL039

pBlue SK mCherry RPL10a	Loayza-Puch Lab	FL045
pCDH1-mCherry-RPL10a	Loayza-Puch Lab	FL043
pBlue SK Neongreen RPL10a	Loayza-Puch Lab	FL169
pMSCV-U6sgRNA(BbsI)-PGKpuro2ABFP	Addgene	102796
pX335-U6-Chimeric_BB-CBh-hSpCas9n(D10A)	Addgene	42335

Table 6. Kits and commercial assays

Resource	Source	Identifier
Oligo Clean&Concentrator	Zymo	D4060
DNA Clean&Concentrator	Zymo	D4013
Pierce Spin Cups	Thermo	69702
NucleoSpin (PCR/gel)	Machery-Nagel	740609.250
NucleoSpin (Plasmid)	Machery-Nagel	740588.250
GenElute HP Plasmid Midiprep Kit	Sigma Aldrich	NA0200-1KT
ZymoPURE II Plasmid Midiprep Kit	Zymo	D4201
SuperScript III First-Strand Synthesis System	Thermo Fisher Scientific	18080051
ELISA MAX Deluxe Set Mouse IFN-γ	BioLegend	430815
Granzyme B Mouse ELISA	Invitrogen	88-8022-22
NextSeq 1000/2000 P2 Reagents (100 Cycles)	Illumina	20046811
NextSeq PhiX Control Kit	Illumina	15051973
MojoSort Mouse CD8 T cell isolation kit	BioLegend	480007
Mycoplasma PCR Detection Kit	abm	G238
Protein Assay Dye Reagent Concentrate	Bio-rad	5000006

Table 7. Cell culture media and reagents

Reagent	Source	Identifier
DMEM High Glucose	Thermo Fisher Scientific	41966-029
DMEM w/o Glucose	Thermo Fisher Scientifc	11966-025
RPMI 1640	Thermo Fisher Scientifc	21875-034
D-Glucose solution	Sigma Aldrich	6844-100ml
FBS	Thermo Fisher Scientific	10270-106
dFBS	Thermo Fisher Scientific	2093867
Penicillin-Streptomycin	Thermo Fisher Scientific	15140-122
Sodium Pyruvate	Thermo Fisher Scientific	11360070
Trypsin - EDTA	Thermo Fisher Scientific	25300096
GlutaMAX	Thermo Fisher Scientific	35050061
RPMI 1640 powder (w/o amino acids, w/o glucose)	US Biological	R9010-01
HEPES	Sigma Aldrich	H4034-100G
D-Glucose monohydrate	VWR	24.371.297
Glycine	Sigma-Aldrich	G8790
L-Serine	Sigma-Aldrich	S4500
L-Arginine (free base) L-Asparagine x H_2O L-Aspartic Acid L-Cystine x 2 HCl L-Glutamic acid L-Glutamine L-Histidine (free base) Hydroxy-L-Proline L-Isoleucine L-Leucine L-Lysine x HCl L-Methionine L-Phenylalanine L-Proline L-Threonine L-Tryptophan L-Tyrosine x 2Na x $2H_2O$ L-Valine	Sigma-Aldrich	A5131 A0884 A9256 C6727 G1251 G3126 H8000 H5534 I2752 L8000 L5626 M9625 P2126 P0380 T8625 T0254 T3754 V0500

Table 8. Cell lines

Cell line	Background	Source
E0771	Mouse medullary breast adenocarcinoma, TNBC, C57BL/6	CH3 Biosystems
B16.F10 (GP33)	Mouse melanoma, C57BL/6J	Donated by Dr. Guoliang Cui at DKFZ
TC-1	Mouse primary lung epithelial cells, C57BL/6, expressing human c-Ha-ras oncogene	Donated by Dr. Chong Sun at DKFZ
Platinum-E cells	Retroviral Packaging Cell Line (293T based)	Donated by Dr. Chong Sun at DKFZ
SUM159 PT	Human TNBC	-
MRC5	Human Lung fibroblast	-
HEK293Tx	Human Epithelial Embryonic Kidney	-

Table 9. Peptides and Recombinant Proteins

Reagent	Source	Identifier
Ovalbumin peptide SIINFEKL (H-2 Kb)	IBA Lifesciences	6-7015-901
LCMV gp33 peptide KAVYNFATM (H-2 Db)	IBA Lifesciences	6-7016-901
Murine Interlukin 2 (mIL-2)	Biolegend	575404
Murine Interlukin 7 (mIL-7)	Peprotech	217-17
Murine Interlukin 15 (mIL-15)	Peprotech	210-15
Human Interferon B (IFN-β)	Peprotech	300-02BC
DQ green BSA	Invitrogen	D12050
Ghost Dye Red 780 Fixable Viability Dye	Cell signaling	18452

Table 10. Antibodies

Resource	Source	Identifier	Dilution
αGFP (B-2)	Santa Cruz	Sc-9996	1:1000
αNeonGreen	Chromotek	32F6	1:1,000
αmCherry	Abcam	Ab167453	1:1,000
RPL10a	Abcam	Ab174318	1: 10,000
GAPDH	Proteintech	60004	1:10000
Actin B	Santa Cruz	sc-47778	1:1000
PHGDH	Sigma	HPA021241	1:1000
SHMT1	Cell Signaling	80715	1:1000
RSP3	Cell Signaling	9538	1:1000
InVivomAb anti-mouse CD28, clone 37.51	Bio X Cell	BE0015-1	-
InVivomAb anti-mouse CD3ε, clone 145-2C11	Bio X Cell	BE0001-1	-
InVivoPlus anti-mouse PD-1 (CD279), clone 29F.1A12	Bio X Cell	BP0273	-
rat IgG2a isotype control, anti-trinitrophenol, clone 2A3	Bio X Cell	BP0089	-
IRDye 800CW Goat anti-Rabbit IgG	Licor	926-32211	1:10000
IRDye® 680RD Goat anti-Mouse IgG	Licor	926-68070	1:10000
APC anti-mouse CD8, clone 53-6.7	Invitrogen	17-0081-82	1:100
DAPI	Thermo Scientific	62247	1:1000
HA.11 Epitope Tag, clone 16B12	Biolegend	901501	
RPL22	Santa Cruz	sc-373993	
Normal mouse IgG	Santa Cruz	sc-2025	-
STAT1	Cell Signaling	9172	1:1000

Table 11. Magnetic beads

Reagent	Source	Identifier
GFP-Trap Magnetic Beads	Chromotek	gtma-20
RFP-Trap Magnetic Beads	Chromotek	rtma-20
Dynabeads MyOne Streptavidin C1	Invitrogen	65002
Pierce Protein A/G Magnetic Beads	Thermo Scientific	88802
HighPrep PCR Clean-up	Magbio	AC-60005

Table 12. Enzymes and master mixes

Product	Source	Identifier
RNase T1	Thermo Fisher Scientific	EN0541
RNase A	Thermo Fisher Scientific	EN0531
RNase 1	Thermo Fisher Scientific	AM2295
Proteinase K	Roche	3115828001
Mth RNA ligase	New England Biolabs	M2611AA
T4 PNK	New England Biolabs	M0201S
T4 Rnl2 K227Q	New England Biolabs	M0351L
5’ Deadenylase	New England Biolabs	M0331S
RecJf Exonuclease	New England Biolabs	M0264S
SuperScript III RT	Thermo Fisher Scientific	2232161
Circularization Ligase II	Lucigen	CL9021K
Q5 High fidelity Master Mix	New England Biolabs	M0494S
LunaScript RT Supermix	New England Biolabs	M3010L
Luna Universal qPCR Mix	New England Biolabs	M3003X
Esp3	New England Biolabs	R0734S
Quick Ligase	New England Biolabs	M2200S
Fast AP	Thermo Fisher Scientific	EF0654
Bbs1	New England Biolabs	R0539S
NEBuilder HiFi DNA Assembly Master Mix	New England Biolabs	E2621S
OneTaq Quick-Load 2X Master Mix	New England Biolabs	M0486S

Table 12. Commercial buffers

Product	Supplier	Catalog number
DPBS (no calcium, no magnesium)	Thermo Fisher Scientific	14190144
Tris-HCl pH 7.5	Thermo Fisher Scientific	15567-027
Sodium acetate solution	Thermo Fisher Scientific	AM9740
20x SSC	Thermo Fisher Scientific	15557-044
EDTA (0.5 M), pH 8.0	Thermo Fisher Scientific	AM9260G
4x Laemli Sample Buffer	Biorad	1610747

Table 13. Animal experiments: Strains and resources

Strain/ resource	Source / Identifier
C57BL/6J	Charles River
P14 x CD4-Cre x Rosa-Cas9-GFP	Donated by Dr. Chong Sun and Dr. Guoliang Cui at DKFZ; PMID: 25263330
Rpl22 X CD4 Cre	Loayza-Puch Lab; PMID: 31216392
OT-I	Donated by Dr. Darjus Tschaharganeh at DKFZ; PMID: 8287475
NSG	Provided by PD Dr. Karin Müller-Decker IMSR_JAX:005557
Baker amino control diet	TestDiet, cat. 5BQT
Baker amino serine and glycine free diet	TestDiet, cat. 5BQS

Table 14. Software and algorithms

Resource	Source / Identifier
Image Lab 6.1	Biorad
Imagestudio Lite	Licor
Quantstudio Design and Analysis v2.6.0	Thermo Fisher Scientific
Graphpad Prism 9	Dotmatics
R Studio, v3.6.2	Posit
Clusterprofiler, v3.14.3	https://bioconductor.org/
Flowjo 10.6.1	FlowJo LLC
Fiji	https://fiji.sc/
FASTX-toolkit	http://hannonlab.cshl.edu/fastx_toolkit/
umi_tools, v1.1.1	PMID: 28100584
Cutadapt, v3.4	https://doi.org/10.14806/ej.17.1.200.
BLAT, v36x2	PMID: 11932250
STAR, v2.5.3a	PMID: 23104886
DESeq2	https://doi.org/10.1186/s13059-014-0550-8
Diricore	PMID: 26878238
Ribowaltz	PMID: 30102689
CellPhoneDB	https://www.cellphonedb.org/
TIDE	http://tide.dfci.harvard.edu/

Table 15. Gel composition

Gel type	Composition	
12 % PAA denaturing gel	Urea	4.8 g
	10x TBE	1 ml
	40 % AA/Bis 19:1	3 ml
	dH_2O	2.5 ml
	10 % APS	50 µl
	TEMED	10 µl
8 % PAA denaturing gel	Urea	4.8 g
	10x TBE	1 ml
	40 % AA/Bis 19:1	2 ml
	dH_2O	3.5 ml
	10 % APS	50 µl
	TEMED	10 µl
8 % PAA non-denaturing gel	10x TBE	1 ml
	40 % AA/Bis 19:1	2 ml
	dH_2O	7 ml
	10 % APS	50 µl
	TEMED	10 µl

Table 16. Buffers composition

Buffer	Composition
PBS + CHX	• 1x PBS • 100 µg/ml CHX
NP40 lysis buffer	• 20 mM Tris-HCl pH. 7.5 pH • 10 mM MgCl2 • 150 mM KCl • 1 % NP40 Added fresh prior to use: • 2 mM DTT • 1x Complete Protease Inhibitor

	• 100 µg/ml CHX
NP40 wash buffer	• 20 mM Tris-HCl pH. 7.5 pH • 10 mM MgCl2 • 350 mM KCl • 1 % NP40 Added fresh prior to use: • 2 mM DTT • 1x Complete Protease Inhibitor • 100 µg/ml CHX
2x Wash/Bind buffer	• 2 mM NaCl • 1 mM EDTA • 5 mM Tris pH 7.5 • 0.2 % Triton-X100
LB medium	• 10 g Tryptone • 5 g Yeast extract • 10 g NaCl Filled up to 1 litre
10x TBE	• 108 g Tris • 55 g Boric acid • 7.4 g EDTA Filled up to 1 litre
10x TAE	• 48.4 g • 11.4 ml glacial acetic acid • 3.7 g EDTA Filled up to 1 litre
10x SDS running buffer	• 248 mM Tris • 1.92 M Glycine • 1 % SDS
10x TBS	• 0.2 M Tris • 1.5 M NaCl Adjusted pH to 7.5
TBS-T	• TBS 1:10 diluted • 0.1 % Tween 20
T cell isolation buffer	• PBS • 3% FBS • 2% EDTA (0.5 M), pH 8.0

MojoSort buffer	• PBS • 0.5% BSA • 2 mM EDTA
SDS/glycerol lysis-loading buffer	• 65mM Tris-HCl pH 6.8 • 2% SDS • 10% glycerol Added fresh prior to use: • 50 mM DTT (from stock 1M, prior use) • 1x Complete Protease Inhibitor

Table 17. Oligos for NGS library preparation

Identifier	Sequence (5'-3')	Source	Stock
3' linker, index ATCGT	/5Phos/NNNNNATCGTAGATCGGAAGAGCACACGTCTGAA/3ddC/	IDT	100 µM
3' linker, index AGCTA	/5Phos/NNNNNAGCTAAGATCGGAAGAGCACACGTCTGAA/3ddC/	IDT	100 µM
3' linker, index CGTAA	/5Phos/NNNNNCGTAAAGATCGGAAGAGCACACGTCTGAA/3ddC/	IDT	100 µM
3' linker, index CTAGA	/5Phos/NNNNNCTAGAAGATCGGAAGAGCACACGTCTGAA/3ddC/	IDT	100 µM
3' linker, index GATCA	/5Phos/NNNNNGATCAAGATCGGAAGAGCACACGTCTGAA/3ddC/	IDT	100 µM
3' linker, index GCATA	/5Phos/NNNNNGCATAAGATCGGAAGAGCACACGTCTGAA/3ddC/	IDT	100 µM
3' linker, index TAGAC	/5Phos/NNNNNTAGACAGATCGGAAGAGCACACGTCTGAA/3ddC/	IDT	100 µM
3' linker, index TCTAG	/5Phos/NNNNNTCTAGAGATCGGAAGAGCACACGTCTGAA/3ddC/	IDT	100 µM

Post ligation product	rUrGrUrUrArGrGrGrArUrArArCrArGrGrGrUrArArUrGrCrGrA NNNNNCGATCTGATCGGAAGAGCACACGTCTGAArC	IDT	1 µM
Reverse transcription primer	/5Phos/NNAGATCGGAAGAGCGTCGTGTAGGGAAAGAG/iSp18/GTGACTGGAGTTCAGACGTGTGCTC	IDT	100 µM
RT product control	/5Phos/NNAGATCGGAAGAGCGTCGTGTAGGGAAAGAG/iSp18/GTGACTGGAGTTCAGACGTGTGCTCTTCCGATCACAGTCNNNNNTCGCATTACCCTGTTATCCCTAACAT	IDT	100 µM
Circularization product control	GTGACTGGAGTTCAGACGTGTGCTCTTCCGATCAGCATGNNNNNTCGCATTACCCTGTTATCCCTAACATNNAGATCGGAAGAGCGTCGTGTAGGGAAAGAG	IDT	100 µM
34-mer marker	rArUrGrUrArCrArCrUrArGrGrGrArUrArArCrArGrGrGrUrArArUrCrArArCrGrCrGrA	IDT	100 µM
Forward library PCR primer	AATGATACGGCGACCACCGAGATCTACACTCTTTCCCTACACGACGCTC	Sigma	100 µM
Reverse library PCR primer - Index 1	CAAGCAGAAGACGGCATACGAGATCGTGATGTGACTGGAGTTCAGACGTGTG	Sigma	100 µM
Reverse library PCR primer - Index 2	CAAGCAGAAGACGGCATACGAGATACATCGGTGACTGGAGTTCAGACGTGTG	Sigma	100 µM
Reverse library PCR primer - Index 3	CAAGCAGAAGACGGCATACGAGATGCCTAAGTGACTGGAGTTCAGACGTGTG	Sigma	100 µM

Table 18. qPCR primers.

Identifier	Sequence (5'-3')	Source	Stock concentration
ASNS	fwd: CGACCAAAGAAGCCTTCAG rev: CCACTTGGGCATCCAGTAAT	Sigma	100 µM
CHOP	fwd: TGGAAGCCTGGTATGAGGAC rev: TGTGACCTCTGCTGGTTCTG	Sigma	100 µM
ATF3	fwd: GTGCCGAAACAAGAAGAAGG rev: TGGAGTCCTCCCATTCTGAG	Sigma	100 µM
GAPDH	fwd: GTCTCCTCTGACTTCAACAGCG rev: ACCACCCTGTTGCTGTAGCCAA	Sigma	100 µM
mActin B	fwd: TCGAGTCGCGTCCACC rev: GGGAGCATCGTCGCCC	Sigma	100 µM
mIFNy	fwd: GAGGAACTGGCAAAAGGATG rev: GACCTGTGGGTTGTTGACCT	Sigma	100 µM
mGZB	fwd: TCGACCCTACATGGCCTTAC rev: TTGCTGGGTCTTCTCCTGTT	Sigma	100 µM
mPHGDH1	fwd: ACAGGTGTGGACAATGTGGA rev: TGTCCCCATGAACTTCTTCC	Sigma	100 µM
mPSAT1	fwd: TGCTCGAAATGAGTCACAGG rev: CAGCACTCCTTCCAGCTTTC	Sigma	100 µM
mPSPH	fwd: AGGAAAACTTCCCAGGATGG rev: ATGGCTCTCCGTGTCATTTC	Sigma	100 µM
mSHMT1	fwd: ATGCCGAGGTTTACAGCATC rev: GGTCCCGCCATAATACCTTT	Sigma	100 µM
mSHMT2	fwd: AGCTCATCGCCTCAGAGAAC rev: CCTTGGAAGCCTTTGACCT	Sigma	100 µM
IFIT3	fwd: TGATGCGTGCCCTACTCTC rev: TCACTCATGACTGCCCTCTG	Sigma	100 µM
MX1	fwd: GACATCGCAAAAGCTGATCC rev: GGGAGTCAATGAGGTCGATG	Sigma	100 µM
ISG15	fwd: CTTTGCCAGTACAGGAGCTTG rev: CGATCTTCTGGGTGATCTGC	Sigma	100 µM
IRF7	fwd: AGCTGTGCTGGCGAGAAG rev: TGTGTGTGCCAGGAATGG	Sigma	100 µM

Table 19. sgRNA for genome editing (purchased from Sigma)

Identifier	Sequence
STAT1 ko1	fwd:CACCGGCTGTGACAGGAGGTCATGA rev: AAACTCATGACCTCCTGTCACAGCC
STAT1 ko2	fwd:CACCGGAGGTCATGAAAACGGATGG rev: AAACCCATCCGTTTTCATGACCTCC
PHGDH ko1	fwd: ACACATGGGTAATTAGGCTGTGT rev: AGAAAAAGGCCCAGAGGAAG
PHGDH ko2	fwd: TTTACCCATGAGGCAAGGAA rev: CCTCCAGATCCACATTGTCC
SHTM1 ko1 (Gibson bridging design)	ATCTTGTGGAAAGGACGAAACACCGTGTAGAATATCATAC CAGCAGTTTTAGAGCTAGAAATAGCAAGTTAAAAT
SHMT1 ko2 (Gibson bridging design)	ATCTTGTGGAAAGGACGAAACACCGTCGGCTGGCAAAAT TCTCCGGTTTTAGAGCTAGAAATAGCAAGTTAAAAT
Non Target Control (Gibson bridging design)	ATCTTGTGGAAAGGACGAAACACCGAAAAAGTCCGCGAT TACGTCGTTTTAGAGCTAGAAATAGCAAGTTAAAAT

Table 20. Human Biotinylated rRNA substraction oligos

Identifier	Sequence (5'-3')	Source	Stock concentration
18S rRNA 204-230	/5Biosg/rUrGrArUrCrUrGrArUrArArArUrGrCrCrGrCrArUrCrCrCrCrCrC	IDT	100 µM
18S rRNA 286-320	/5Biosg/rCrGrUrGrCrGrArUrCrGrGrCrCrCrGrArGrGrUrUrArUrCrUrArGrArGrUrCrArCrCrArA	IDT	100 µM
18S rRNA 836-871	/5Biosg/rArUrUrCrCrArUrUrArUrUrCrCrUrArGrCrUrGrCrGrGrUrArUrCrCrArGrGrCrGrGrCrUrC	IDT	100 µM
18S rRNA 1715-1745	/5Biosg/rUrCrCrGrArGrGrGrCrCrUrCrArCrUrArArArCrCrArUrCrCrArArUrCrGrGrU	IDT	100 µM
28S rRNA 183-216	/5Biosg/rGrGrGrCrCrUrCrGrArUrCrArGrArArGrGrArCrUrUrGrGrGrCrCrCrCrCrCrArCrGrA	IDT	100 µM

28S rRNA 919-950	/5Biosg/rUrCrGrCrUrCrCrCrUrCrGrGrCrCrCrCrGrGrGrArUrUrCrGrGrCrGrArGrUrGrC	IDT	100 µM
28S rRNA 4055-4090	/5Biosg/rCrCrGrCrCrUrCrArCrCrGrGrGrUrCrArGrUrGrArArArArArArCrGrArTrCrArGrArGrUrA	IDT	100 µM
28S rRNA 4100-4135	/5Biosg/rCrCrGrGrGrCrGrCrUrUrGrGrCrGrCrCrArGrArArGrCrGrArGrArGrCrCrCrCrUrCrGrGrG	IDT	100 µM
28S rRNA 4735-4770	/5Biosg/rGrArCrCrGrGrCrUrArUrCrCrGrArGrGrCrCrArArCrCrGrArGrGrCrUrCrCrGrCrGrGrCrG	IDT	100 µM
5.8S rRNA 125-157	/5Biosg/rArGrCrGrArCrGrCrUrCrArGrArCrArGrGrCrGrUrArGrCrCrCrCrGrGrGrArGrGrA	IDT	100 µM
18S rRNA 204-230	/5Biosg/rUrGrArUrCrUrGrArUrArArArUrGrCrCrGrCrArUrCrCrCrCrCrC	IDT	100 µM
18S rRNA 286-320	/5Biosg/rCrGrUrGrCrGrArUrCrGrGrCrCrCrGrArGrGrUrUrArUrCrUrArGrArGrUrCrArCrCrArA	IDT	100 µM
18S rRNA 836-871	/5Biosg/rArUrUrCrCrArUrUrArUrUrCrCrUrArGrCrUrGrCrGrGrUrArUrCrCrArGrGrCrGrGrCrUrC	IDT	100 µM
18S rRNA 1715-1745	/5Biosg/rUrCrCrGrArGrGrGrCrCrUrCrArCrUrArArArCrCrArUrCrCrArArUrCrGrGrU	IDT	100 µM
28S rRNA 183-216	/5Biosg/rGrGrGrCrCrUrCrGrArUrCrArGrArArGrGrArCrUrUrGrGrGrCrCrCrCrCrCrArCrGrA	IDT	100 µM
28S rRNA 919-950	/5Biosg/rUrCrGrCrUrCrCrCrUrCrGrGrCrCrCrCrGrGrGrArUrUrCrGrGrCrGrArGrUrGrC	IDT	100 µM
28S rRNA 4055-4090	/5Biosg/rCrCrGrCrCrUrCrArCrCrGrGrGrUrCrArGrUrGrArArArArArArCrGrArTrCrArGrArGrUrA	IDT	100 µM

Table 21. Mouse rRNA oligo data table. All sequences illustrated 5'-3'. Table adapted from (Ferhat Alkan et al., 2020)

Oligo	Sequence	rRNA target
S1opt-o1	UGAUCUGAUAAAUGCACGCAUCCCCCC	18S
S1opt-o2	CGUGCGAUCGGCCCGAGGUUAUCUAGAGUCACCAA	18S
S1opt-o3	AUUCCAUUAUUCCUAGCUGCGGUAUCCAGGCGGCUC	18S
S1opt-o4	GGGCCUCGAUCAGAAGGACUUGGGCCCCCCACGA	28S
S1opt-o5	UGGCUUCCUCGGCCCCGGGAUUCGGCGAAAGC	28S
S1opt-o6	ACGGACGCUUGGCGCCAGAAGCGAGAGCCCCUCGGG	28S
S1opt-o7	ACCCGGCUAUCCGGGGCCAACCGAGGCUCCUUCGGCG	28S
S1opt-o8	ACCGACGCUCAGACAGGCGUAGCCCCGGGAGGA	5.8S
S1opt-o9	GGCGGACGGGGGGAGAGGGAGAGCGC	28S
S1opt-o10	GGCGAGACGGGCCGGUGGUGCGCCCUCGGC	28S
S1opt-o11	CCAGAAGCAGGUCGUCUACGAAUGGUUUAG	28S
S1opt-o12	AUCCCCGAUCCCCAUCACGAAUGGGGUUCA	18S
S2o11423	GCUCUGCUACGUACGAAACCCCGACC	28S
S2o25014	GUGUCGAGGGCUGACUUUCAAUAGAUCG	28S
S2o12152	AGAUCCAACUACGAGCUUUUUAACUG	18S
S2o6146	AACGCCACUUGUCCCUCUAAGAAGU	18S
S2o13419	CAAGUGCGUUCGAAGUGUCGAUGAUC	5.8S

3.2 Methods

3.2.1 Cell culture

SUM159PT and MRC5 cells were cultured in DMEM High Glucose Medium (Thermo Fisher Scientific; cat. 41966-029) supplemented with 10 % FBS (Thermo Fisher Scientific; cat. 10270-106) and 100 units/ml penicillin and 100 mg/ml streptomycin (Thermo Fisher Scientific; cat. 15140-122). For glucose starvation experiments, cells were cultured for 72h in DMEM without glucose and pyruvate (Thermo Fisher Scientific; cat. 11966-025) supplemented with either 4.5 g/l (high glucose) or 0.45 g/l glucose (low glucose), 10 % dialysed fetal bovine serum (Thermo Fisher Scientific; cat. 2093867) and 100 units/ml penicillin and 100 mg/ml streptomycin (Thermo Fisher Scientific; cat. 15140-122).

For conditioned media (CM) experiments, MRC5 cells were incubated for 72h in low or high glucose medium in the presence or absence of 10 ng/ml IFN-β (Peprotech; cat. 300-02BC). Supernatant was sterile filtered at 0.45 µm, followed by fractionation with Amicon columns to get rid of reminiscent IFN (Merck; cat. UFC900308). 10 % dialysed FBS and 0.45 g/l glucose were added to the small faction of supernatant (<3Kd) before incubation with SUM159PT cells.

Mouse cell lines B16, E0771 and TC1 were grown in RPM1 1640 (Thermo Fisher Scientific; cat. 21875-034) supplemented with 10 % FBS, 100 units/ml penicillin and 100 mg/ml streptomycin (Thermo Fisher Scientific; cat. 15140-122), 1 mM sodium pyruvate (Thermo Fisher Scientific; cat. 11360-070), 20 mM HEPES (Sigma; cat.H4034) and 50 µM β-mercaptoethanol (Sigma; cat. M6250). Mouse lines expressing chicken ovalbumin (B16-OVA and TC1-OVA) or the lymphocytic choriomeningitis virus (LCMV) glycoprotein 33 (B16-GP33) were kindly donated by Dr. Guoliang Cui and Dr. Chong Sun. Platinum-E cells were used at low passage and cultured in DMEM (Thermo Fisher Scientific; cat. 41966-029) supplemented with 10 % FBS (Thermo Fisher Scientific; cat. 10270-106), 100 units/ml penicillin and 100 mg/ml streptomycin (Thermo Fisher Scientific; cat. 15140-122) and 1% GlutaMAX (Thermo Fisher Scientific; cat. 35050061). All cell lines were regularly tested for Mycoplasma contamination and kept at 37 °C in 5 % CO2.

3.2.2 Lentiviral overexpression and knock out generation

MRC5 fibroblasts expressing heterozygous ribosomal tagging (MRC5-mCherry-RPL10a) were produced via lentiviral overexpression. Virus was generated in HEK293Tx using PEI max transfection reagent (Polyscience; cat. 24765-1), lentiviral packaging plasmids (Addgene: 12251, 12253 and 14888) and the vector coding for the fluorescent chimera (pCDH1-mCherry-RPL10a). After viral transduction in presence of polybrene (Santa Cruz;cat. Sc-255611), cells were sorted for mCherry via FACS. sgRNA against STAT1 were purchased from Sigma (sgRNA, Table 15) and cloned into a lentiviral expression vector for Cas9 (plentiCRISPR v2; addgene 52961). SUM159PT and MRC5 knock outs were then prepared via lentiviral transduction as previously described (Shalem et al., 2014), and selected with 2 µg/ml puromycin (Sigma; cat. P8833) for 5 days. E0771 cells expressing chicken ovalbumin (E0771-OVA) were generated via lentiviral transduction as described above and selected with 10 µg/ml blasticidin (Santa Cruz; cat.sc-495389) for 3 days.

3.2.3 Homozygous knock-in of ribosomal fluorescent proteins

Endogenous fluorescent tagging of ribosomal proteins RPL10a and RPS3 was performed in human and murine cancer lines (SUM159PT-GFP-RPL10a, SUM159PT-GFP-RPS3 and E0771-GFP-RPL10a) via homozygous knock-in with paired CRISPR-Cas9 as previously described[110]. In brief, two Cas9D10A plasmids expressing nickase (Backbone Addgene: 42335) and gRNAs targeting the sense and antisense strands of the ribosomal protein locus, were transfected in the presence of the DNA repair template of a donor plasmid containing the fluorescent marker flanked by homology arms. Positive homozygous clones were tested for polysome incorporation of the endogenously expressed chimera, and proliferation was traced compared to the parental for 8 days with Incucyte S3.

3.2.4 Mice

6-8 weeks NSG, C57BL/6J, OT-1, Rpl22 x CD4 Cre and P14 x CD4-Cre x Rosa-Cas9-GFP were either purchased from the Charles River Laboratory or bred in our animal facility. All mice were maintained in a pathogen-free facility and used according to the

German Cancer Research Center and following permission by the controlling government office (Regierungspräsidium Karlsruhe) according to the German Animal Protection Law, and in compliance with the EU Directive on animal welfare, Directive 2010/63/EU.

3.2.5 Animal experiments

For tumor xenografts, orthotopic injection in the fat pad of NSG mice was performed with 2 million SUM159-eGFP-RPL10a breast cancer cells and/or in combination with MRC5-mCherry-RPL10a fibroblasts, at least 6 mice per condition were evaluated. To evaluate the effect of checkpoint inhibition in a T cell ribotag transgenic model, Rpl22 X CD4 Cre mice were injected in the fat pad with 2 million E0771-eGFP-RPL10a syngeneic breast cancer cells. Upon tumor formation, mice received two intraperitoneal injections with 3 days gap of 2 µg/µl of mouse anti-PD1 (BioXcell, BP0273) or rat IgG as control (BioXcell, BP0273), at least 4 mice per condition were evaluated. For xenografts and transgenic models, tumor growth was measured every 2-4 days until a maximum size of 1.5 cm in one dimension and cryopreserved for DualRP library preparation. For dietary intervention experiments, C57BL/6J mice received serine-glycine free diet (TestDiet, cat. 5BQS) or full control diet (TestDiet, cat. 5BQT) after one week injection with the same syngeneic E0771-eGFP-RPL10a line. Mice were treated with 5 rounds of anti-PD1 or IgG with 2 days apart using concentrations above. At least 9 mice were tested per group. Experiment was ended until tumors reached a maximum size of 1.5 cm in one dimension.

3.2.6 Immunoblotting

For immunoblotting of polysome fractions, cells were washed with ice-cold PBS with 100 µg/ml cycloheximide (CHX) and lysed in NP40 lysis buffer (20 mM Tris-HCl pH. 7.5 pH, 10 mM MgCl2 ,150 mM KCl, 1 % NP40, 2 mM DTT, 1x EDTA-free complete protease inhibitors and 100 µg/ml CHX) for 15 min on ice and centrifuged at 1300 g for 10 min. The supernatant was pipetted on top of a sucrose gradient and centrifuged for 2 hours at 36.000 rpm and 4°C in the Optima XPN 100 ultracentrifuge with swinging bucket rotor SW41 Ti (Beckman Coulter). Each fraction was loaded with 1x Laemmli buffer (Biorad; cat. 1610747) in a 12 % SDS gel.

For STAT1, PHGDH and SHMT1 blotting, cell pellets were directly suspended in SDS/glycerol lysis-loading buffer and denatured at 95°C for 10 min. Protein concentrations were determined via Bradford assay (Bio-Rad, cat. 5000006) and equal protein amounts analysed by SDS gel electrophoresis.

Western blotting was performed with 0.45 µm nitrocellulose membranes using the Trans-blot turbo system (Bio-rad). The membranes were blocked for 1 h with 5 % skimmed milk in TBST. Primary antibodies and dilutions were used according to Table 10. After overnight incubation at 4°C, secondary antibodies were added for 1 h and blots were imaged using Oyssey Clx imaging system operated by ImageStudio Lite (Licor).

3.2.7 Dual Ribosome Profiling

The DualRP protocol involves two main steps: immunoprecipitation of the ribosomal fusion proteins and library preparation from the isolated RPFs. For co-culture experiments, SUM159-eGFP-RPL10a and MRC5-mCherry-RPL10a cells were plated one million each in 15 cm dishes, and cultured for 72 h. On the day of harvesting, cells were washed with ice-cold PBS supplemented with 100 µg/ml CHX, scraped, and centrifuged at 1300 x g for 5 min.

Cells were lysed in 1 ml of NP40 lysis buffer (20 mM Tris-HCl, pH 7.8, 10 mM MgCl2, 150 mM KCl, 1% NP40, 2 mM DTT, 1× Complete protease Inhibitors, 100 ug ml−1 CHX) for 15 min on ice. For *in vivo* experiments, tumors were snap frozen in liquid nitrogen upon surgical removal and lysed in a tissue homogenizer for 30 s at 2500 rpm (Mikro dismembrator-S), in the presence of ice-cold lysis buffer. The lysate (cell or tumor) was centrifuged at 4ºC for 10 min at 1300 x g and the supernatant subjected to RNAse digestion for 30 min at room temperature under constant rotation.

A combination of RNase T1 (2000 U) and RNase A (20 ng), or only RNase I (1000 U) were used for nuclease foot-printing. Resulting monosomes were purified with 40 ul GFP-Trap-Magnetic beads (Chromotek) for cancer cells, RFP-Trap-Magnetic beads (Chromotek) for fibroblasts, or protein A/G beads (Thermo Scientific) pre-loaded with

HA epitope (Biolegend) for tumor-infiltrating T cells. After 1 h incubation at room temperature, beads were washed per triplicate with 1 ml of NP40 Lysis buffer and with NP40 wash buffer (20 mM Tris-HCl pH 7.8, 10 mM MgCl2, 350 mM KCl, 1% NP40, 2 mM DTT, 1× Complete protease Inhibitors, 100 µg ml−1 CHX). To cleave immunoprecipitated ribosomes, beads were incubated for 1 h at 45 °C in 300 µl of NP40 Lysis Buffer supplemented with 1 % SDS and 15 µl of PCR-grade proteinase K (Roche).

The supernatant was resuspended in 1 ml TriReagent (Zymo) and libraries prepared according to the previously described ribosome profiling protocol[102]. In brief, RPF were isolated via phenol-chloroform and size-selected (17-34 nt) from a 12% PAA-Urea denaturing gel. After RNA gel extraction with sodium acetate and ethanol precipitation, the 3' ends of the RPF were dephosphorylated with T4 PNK (NEB) to allow the ligation of a pre-adenylated DNA linker with T4 Rnl2(tr) K227Q (NEB). Excess of unbound linker was removed with 5' Deadenylase and RecJf (NEB) allowing linker 5' deadenylation and DNA degradation from the 5' end. Samples were pooled and rRNA was depleted with either mouse or human-specific rRNA biotinylated oligo cocktail (Sequences in Tables 20-21) and MyOne Streptavidin C1 DynaBeads (Invitrogen). The produced RNA-DNA hybrid molecule was used as a template for reverse transcription with the SuperScript III RT system (Thermo Fisher Scientific), and purified on an 8 % PAA-Urea gel. Full-length produced single-stranded cDNA was circularized with CircLigase II (Lucigen) to increase amplification efficiency. For optimal DNA concentration the circularized product was amplified via PCR with Q5 High Fidelity Master Mix (NEB), resulting in a double-stranded DNA library. After DNA cleaning (Zymo) and purification in a 8 % PAA-gel, library DNA concentrations were determined by Qubit HS DNA kit and adjusted to 2nM before sequencing.

3.2.8 Illumina sequencing

Ribo-Seq libraries were sequenced in the NextSeq2000 (Illumina) using the 100 cycles cartridge and P2 flow cell, at the DKFZ Sequencing Open Lab. According to the Illumina Systems Guide, library was diluted and loaded at a concentration of 650 pM by diluting 7.8 µl of the 2 nM library with 16.2 µl of supplied RSB. To monitor the quality of the sequencing run, 1 µl of 1 nM PhiX (Illumina) was added to the mixture,

resulting in a ~2% PhiX spike-in. The runs were set up for single-read and 110 cycles. The DKFZ Genomics & Proteomics Core Facility provided the demultiplexed FASTQ data for further processing.

3.2.9 Sequencing data analysis

Bioinformatic analysis was performed by Alexander Kowar and Ekaterina Stepanova from the Translational Control and Metabolism group at DKFZ. For data preprocessing and alignment, the adaptor sequences were trimmed using cutadapt (v3.4) and demultiplexed with barcode splitter from FASTX-toolkit (Cold Spring Harbor Laboratory, Hannon Lab, by Assaf Gordon). rRNA, tRNA, and sequences shorter that 30nt were filtered out. Unique molecular identifiers (UMIs) were extracted with umi_tools (v1.1.1) and the rRNA discarded with BLAST-Like Alignment Tool (BLAT, v36x2). The remaining reads were aligned to the GRCh37/hg19 human genome or to GRCm38/mm10 mouse genome by Spliced Transcripts Alignment to a Reference (STAR, v2.5.3a). PCR duplicates were removed for differential gene expression analysis using umi_tools. The data was subjected to differential expression analysis with DESeq2 and transcripts sorted by fold change with a Benjamini-Hochberg adjusted p-value of ≤ 0.05. Gene Ontology enrichment (GO term) analysis was conducted with clusterProfiler (v3.14.3) and R (v3.6.2). Diricore analysis was performed to determine amino acid codon occupancies from RPFs between samples. Gene expression mediated biases in codon frequencies was ruled out by gene-level normalization. Reads with unambiguous gene IDs and reading frames were counted for codons 12 and 15 nt downstream of the 5'end, resembling the A- and P-site. In-frame periodicity was evaluated by Ribowaltz, which identifies annotated translation initiation sites (TIS) within the reads and calculates the 3' and 5' distances from TIS to estimate the P-site location within the 5' UTR, CDS and 3' UTR.

3.2.10 Fluorescence microscopy and image analysis

Lysosomal proteolysis assays were carried out by Edoardo Ratto from the Cell Signaling and Metabolism Group at DKFZ. WT and STAT1 knock out versions from MRC5-mCherry-RPL10a and SUM159-eGFP-RPL10a cells were plated on 8-well chambered coverslips (IBIDI) and left to attach overnight. Lysosomal proteolysis was

investigated by live cell imaging with DQ BSA green or red (Invitrogen). In brief, cells were incubated with 0.1 mg/ml DQ BSA for 4–6 h, washed two times and chased for 3 h in fresh media to allow lysosomal accumulation of DQ BSA. 0.5 µg/ml Hoechst were added prior imaging. Imaging was performed in a humidified chamber at 37 °C and 5% CO2 with a Leica TCS SP5 confocal microscope using a ×40 or ×63, 1.40 oil objective.

Fluorescence was quantified using the particle analyzer function of Fiji in randomly chosen fields of view across the entirety of each sample. Mean cellular fluorescence was determined by normalizing the integrated signal density of the respective fluorescent probe to cell number. To quantify lysosomal DQ BSA fluorescence dequenching, DQ BSA integrated density was normalized to the total cell area.

3.2.11 RNA isolation and quantitative real-time PCR

Total RNA isolation was performed via phenol-chloroform extraction using TRI Reagent (Zymo Reseach; cat. R2050-1-200), followed by ice-cold isopropanol precipitation and centrifugation at 20,000 x g for 45 min at 4°C. RNA pellet was washed twice with 75 % ethanol, and resuspended in nuclease- free water. The concentration was determined at 280 nm with NanoDrop One C (Thermo). 600 ng of total RNA was reversed transcribed using LunaScript RT Supermix (NEB; cat. M3010L) and quantitative real-time PCR was performed using Luna Universal qPCR Mix (NEB; cat. M3003X) following manufacturer's instructions. Ct values were obtained with Quantstudio 5RT qPCR System and analysed using Quantstudio Design and Analysis Software 2.6.0. mRNA fold change of target genes (Table 14. qPCR primers) was calculated by ΔΔCt method.

3.2.12 Flow cytometry and flow sorting

Flow cytometry was performed on BD Canto or Fortessa HTS FACS machines. FACS sorting was conducted on a BD Aria II and flow analyses were performed with FlowJo 10.6.1 software (LLC). For GFP-RPL10a clone selection and enrichment of mCherry-RPL10a fibroblasts a 100 µM nozzle was used. For rapid separation of CD8 T cells and tumor cells from co-culture plates, CD8 T cells were transferred from the co-

culture plates to a 10 mm cell strainer (PluriSelect) to retain any tumor cells detached from the plate as previously described[111]. Staining with 1:100 APC anti-mouse CD8, clone 53-6.7 (Invitrogen) and 1:1000 DAPI (Thermo Scientific) was carried out for 1 h at 37°C and living cells were sorted with a 100 µM nozzle for GFP (cancer cells) and APC (T cells). Positive transduced T cells for SHMT1 and PHGDH knock outs were sorted for GFP+ BFP+ population using the 85µm nozzle.

3.2.13 CD8+ T cell isolation and culture

Primary naive CD8+ T cells were isolated from spleens of OT-1 mice in the presence of 25nM ovalbumin peptide SIINFEKL for 72h (IBA; cat. 6-7015-901). T cells were kept in RPM1 1640 (Thermo Fisher Scientific; cat. 21875-034) supplemented with 10 % FBS and 1 % penicillin-streptomycin, 1mM sodium pyruvate (Thermo Fisher Scientific; cat. 11360-070), 20 mM HEPES (Sigma; cat. H4034), 50 µM β-mercaptoethanol (Sigma; cat.M6250) and 10 ng/ml murine IL-2 (Biolegend; cat. 575404). For serine/glycine starvation experiments, medium was prepared fresh from RPMI 1640 powder without amino acids (US Biological; cat. R9010-01) and each component added individually according to the ATCC formulation (Table 6).

3.2.14 T cell knock out generation

Platinum-E cells were transfected with pMSCV vectors (Addgene:102796) containing a BFP selection marker and sgRNA for PHGDH or SHMT1. Transfection was performed using PEI max transfection reagent (Polyscience; cat. 24765-1) and 10µg DNA for 16h at 37 °C and 5% CO2. Retroviral supernatants were collected after 48 and 72 hours transfection and filtered through 0.45µm. Naive CD8+ T cells were isolated from P14 x CD4-Cre x Rosa-Cas9-GFP mice using the MojoSort Mouse CD8 T cell isolation kit (BioLegend; cat. 480007) and activated on plates coated with 0.5 µg/ml anti-CD3 (BioXCell; cat. BE0001-1) and 2.5 µg/ml anti-CD28 (BioXCell; cat. BE0015-1) including mouse interleukins at 1 ng/ml IL-2 (Biolegend; cat. 575404), 5 ng/ml IL-7 (Peprotech; cat. 217-17) and 5 ng/ml IL-15 (Peprotech; cat. 210-15). After 24 h activation, transduction was performed by spinfecting T cells at 2000 x g for 90 min at 30°C in presence of the retroviral supernatants and retronectin (Takara; cat. T100A). The cells were incubated at 37°C, 5% CO2 for 24 h before washing off the

virus and expanded for 48h in medium containing 1 µg/ml anti-CD3 (BioXCell; cat. BE0001-1), 0.5 µg/ml anti-CD28 (BioXCell; cat. BE0015-1) and mouse interleukins at the concentrations mentioned above. Transduced CD8+ T cells were selected by sorting by FACS based on GFP and BFP expression.

3.2.15 T cell killing and gene expression assays

OT-I T cells were co-cultured with mouse cancer cells expressing chicken ovalbumin (B16-OVA, TC1-OVA and E0771-OVA) with increasing concentrations of serine. After 24h, cells were washed with PBS and stained with crystal violet to assess killing efficiency. Imaging was performed with Dual Lens System V850 Pro Scanner (Epson) and colony area was quantified with a previously published ImageJ plugin[112]. To determine gene expression, OT-1 T cells were co-cultured with OVA cells for 24h and sorted for viable CD8+ cells by FACS, pellets were subjected to RNA isolation and qPCR for serine and one carbon metabolism pathway genes. P14 T cells knock outs were co-cultured for 24h with mouse cancer cells expressing the lymphocytic choreomeningitis virus (LCMV) glycoprotein 33 (B16-GP33) or with E0771 cells preloaded with LCMV gp33 peptide (IBA; cat. 6-7016-901), crystal violet staining and imaging was performed as described above.

3.2.16 ELISA assays

Cytokine release in CD8+ T cells was quantified from cell supernatant using ELISA MAX Deluxe Set Mouse IFN-γ (BioLegend; cat. 430815) and Granzyme B Mouse ELISA (Invitrogen; cat. 88-8022-22) according to manufacturer's instructions. Each sample was measured with the Multiskan FC (Thermo) plate reader as the 450nm-570nm absorbance's subtraction and final concentrations were calculated with the 4-parameter logistic curve-fitting algorithm in GraphPad Prism.

3.2.17 Metabolomics

Metabolomic analysis was carried out in collaboration with Dr. Ilaria Elia and Silvia Cadenas at KU Leuven. In brief, CD8+ T cells were isolated from the spleen of eight-

week-old OT-1 female mice and activated as previously described (PMID: 35820416). For the co-culture assay, 1,000,000 E0771-OVA cells/replicate were plated in 15 cm dishes 48 hours before the co-culture to let them adhere. Pre-activated OT-1 CD8+ T cells were transferred on top of the E0771-OVA cells in a 1:5 ratio (CD8+ T cells : tumor cells). For T cell-only assays, 2,000,000 pre-activated CD8+ T cells/replicate were cultured in 6-well plates. For tumor-cell-only assays, 200,000 E0771-OVA cells/replicate were plated in 6-well plates 48 hours before the assay to let them adhere. Finally, 800,000 naïve CD8+ T cells/replicate were cultured in 24-well plates. All metabolic assays were conducted in full RPMI or RPMI without serine (Bioquote, R9660). In both media, ^{12}C glucose was replaced by $^{13}C_6$ labelled glucose (Cambridge Isotope Laboratories, 110187-42-3). After six hours of culture in media with or without serine and in the presence of $^{13}C_6$ glucose, CD8+ T cells and tumor cells were collected for further metabolic analysis. Collection, quenching, and metabolite extraction were performed as previously described (PMID: 35820416). Metabolites were measured using gas chromatography-mass spectrometry as previously described (PMID: 35585241).

IV. Results

4.1 Fibroblasts and breast cancer interactions

4.1.1 Cellular models of ribosomal protein tagging

To establish Dual-RP *in vitro*, the triple negative breast cancer line SUM159 PT was tagged with GFP in the ribosomal protein L10a (RPL10a) locus via homozygous CRISPR-mediated knock-in. This method allows the endogenous fluorescent tagging of RPL10a (**Figure 3A**), which is efficiently incorporated into polysomes (**Figure 3B**). In the case of human fibroblasts, lentiviral transduction of the MRC5 line with mCherry-RPL10a drives the chimera overexpression. The chimera is subsequently enriched by FACS and also showed proper polysome incorporation. Similar proliferation patterns were observed for the tagged versions of both cell types over the period of 8 days (**Figures 3C-D**).

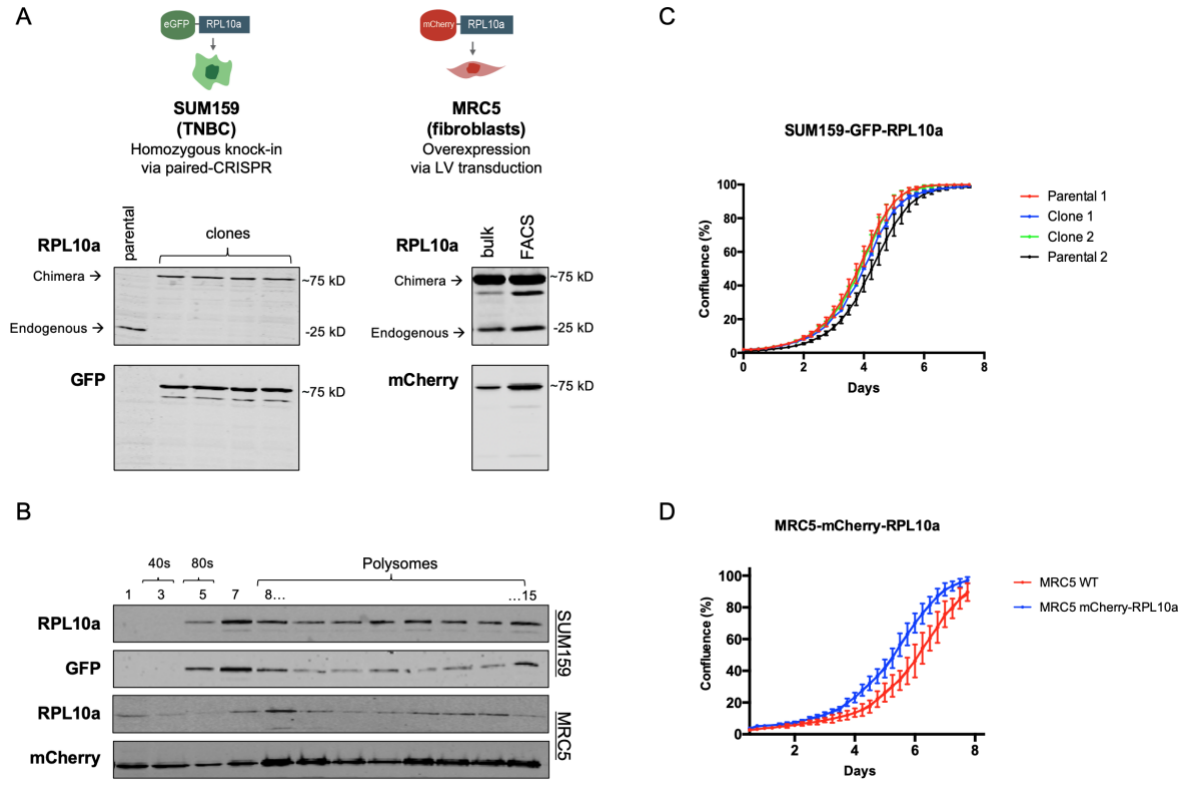

Figure 3 | Ribosomal tagging models for Dual-RP. (**A**) Cellular models of RPL10a tagging depict the homozygous expression of RPL10a-GFP in SUM159 cells (upper left) and the enriched expression of RPL10a-mCherry in MRC5 fibroblasts (upper right). (**B**) The incorporation of the chimera into translating polysomes is also confirmed via sucrose gradient on both cell types. (**C**) Proliferation curves on SUM159 clones and (**D**) MRC5 fibroblasts compared to its tagged version resemble parental controls. (SD, N=5).

4.1.2 Gene expression of ribosome-tagged clone positively correlates with its parental control

To validate the gene expression patterns from the pull-down of tagged ribosomes, I tested the classical ribosome separation via sucrose gradient in both parental control and the endogenously tagged RPL10a clone. The analysis showed a good correlation (*R*=0.963, **Figure 2**) of both ribosome isolation methods and cell types, with few outliers for genes translated by the mitochondrial ribosomes, which are co-purified in the sucrose gradient but not considered in the pull-down.

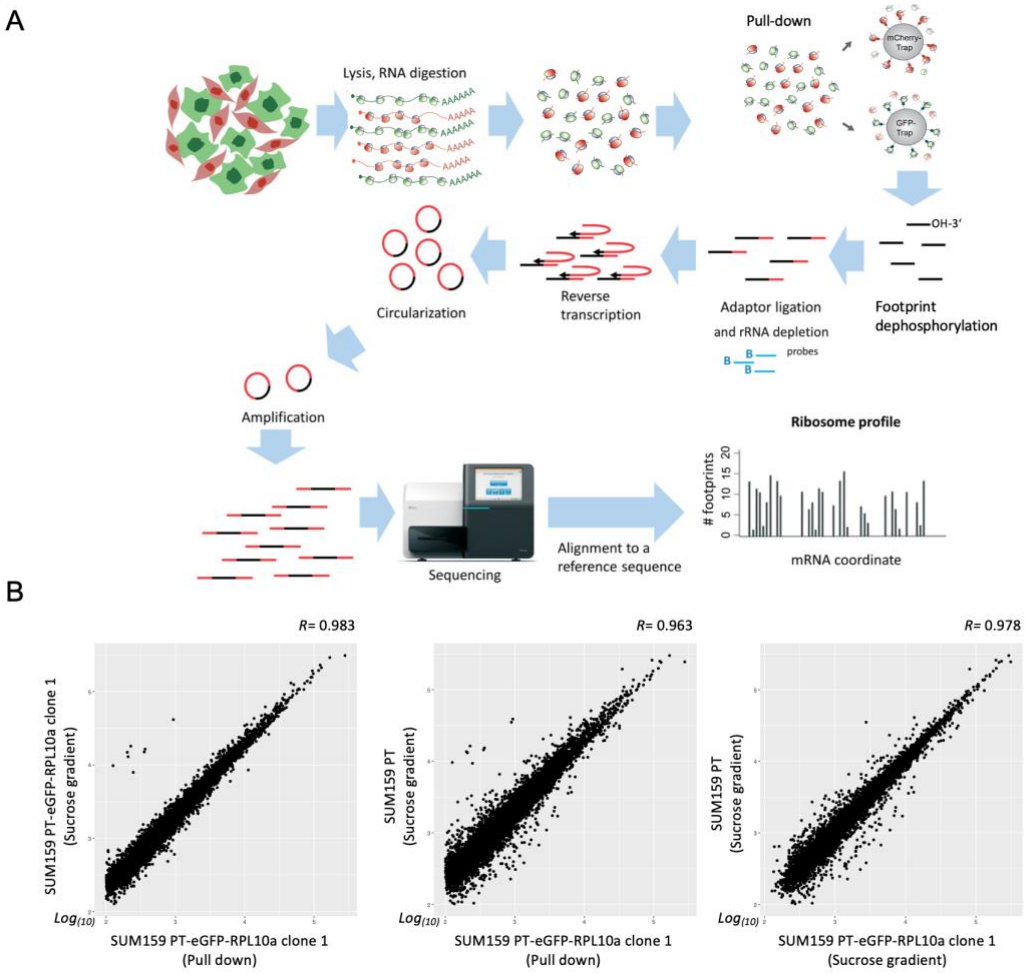

Figure 4 | Gene expression of ribosome-tagged clone and parental control using different ribosome isolation methods. (**A**) Schematic representation of Dual-RP library preparation with trapping of fluorescent ribosome-protected fragments followed by Ribo-seq standard protocol. (**B**) Correlation matrix of ribosome profiling by sucrose density ultracentrifugation versus Dual-RP pull-down for SUM159-GFP-RPL10a clone 1 (left), clone 1 and parental control (middle) and the same method in both cell types (right). Pearson correlation coefficients (*R*) are obtained from all genes on each data set.

4.1.3 Global gene expression changes detected by DualRP are orchestrated by cell-to-cell interactions

To test Dual-RP *in vitro*, cells were co-cultured in a monolayer for three days. Subsequently, Ribo-Seq libraries were prepared from the immunoprecipitated ribosome-protected fragments (RPFs) of each fluorescent tag (**Figure 5A**). Cross contamination effects were excluded by immunoblotting of the pull-downs (**Figure 5B**). Importantly, the global gene expression analysis of the co-culture demonstrated the highest variance compared to that of the single cultures and their combined lysates (**Figure 5C**). This finding confirms that Dual-RP successfully captures the global gene expression derived from cell-to-cell contact interactions.

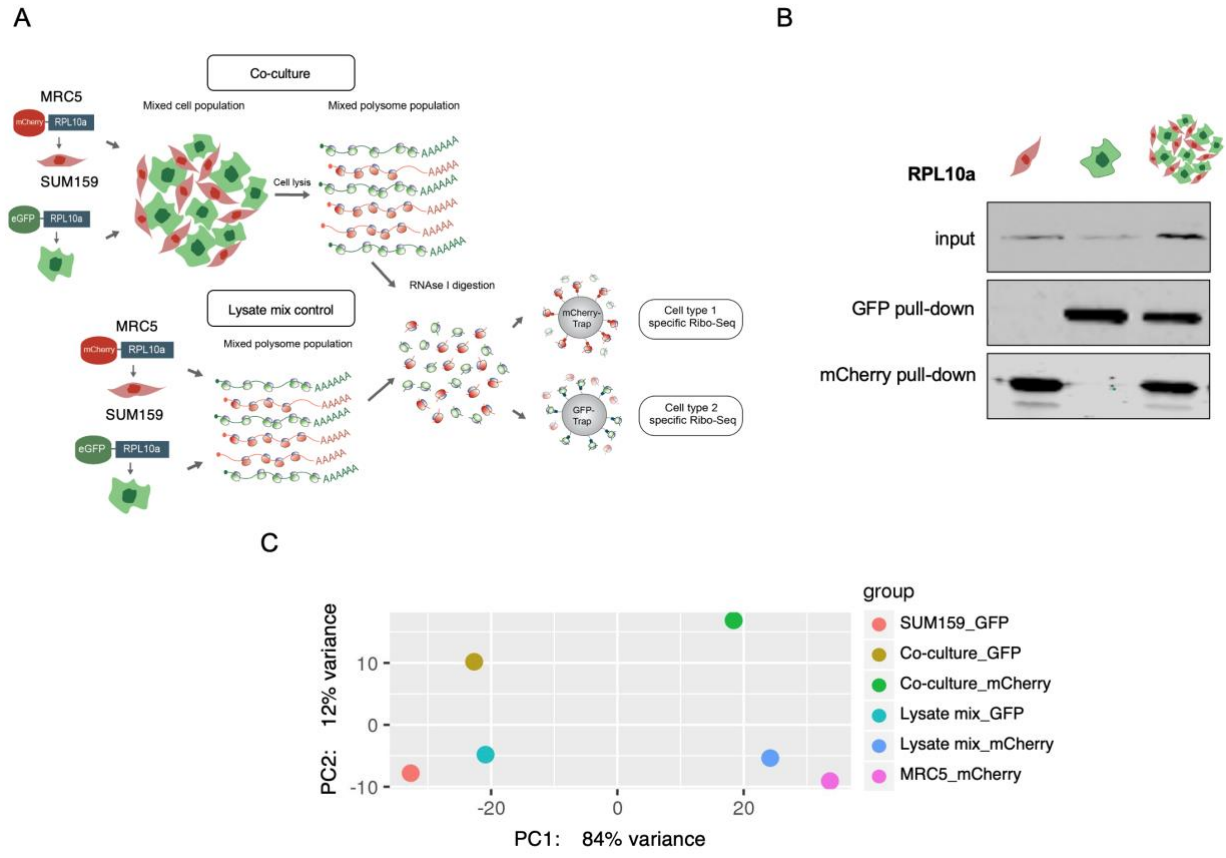

Figure 5 | The establishment of Dual-RP *in vitro*. (**A**) Schematic representation of Dual-RP prior Ribo-Seq library preparation including the control after lysis. (**B**) RPL10a immunoblotting of fluorophore pull-down excludes unspecific binding in co-culture. (**C**) PCA portrays similar correlation of global gene expression for single controls and in controls after lysis, in contrast to both clusters of cancer cells and fibroblasts in co-culture.

4.1.4 Signaling pathway alterations in fibroblasts and breast cancer cells under nutrient stress

One of the main advantages of DualRP is its ability to measure gene expression profiles of two interacting cell populations simultaneously. To gain deeper insights into the affected signaling pathways in cancer cells and fibroblasts under nutrient stress, cells were grown under low glucose concentrations. At first glance, there was a pronounced upregulation of interferon type I (IFN) signaling triggered by cell-to-cell contact in co-cultured cancer cells and fibroblasts, independently of glucose concentrations (**Figures 6A and S1A**).

In contrast, pathways such as ECM organization, Wnt, and Notch signaling, were uniquely activated in cancer cells in co-culture. Meanwhile, the nuclear Factor-kappa B (NFκβ) and vascular endothelial growth factor (VEGF) signaling were activated exclusively in fibroblasts growing with cancer cells (**Figure 6A**). On the other hand, while the downregulation of cell cycle and DNA replication genes had an impact on cancer cells growing in monoculture under low glucose conditions, it did not affect them when they were in co-culture (**Figures 6A,C**). Notably, the co-culture interactions alone had a remarkable effect in restoring the response to nutrient stress. This was evident through the rescue of genes associated with branches of the integrated stress response, such as ER-stress, which were initially induced by glucose starvation in both cell types independently (**Figures 6A,B**).

At the same time, the pathway alterations obtained with DualRP were corroborated by CellPhoneDB[113], a publicly available repository of curated receptor-ligand interactions used for analyzing single-cell transcriptomics data (**Figure S1B**). Moreover, to discard any potential bias in codon occupancy with specific ribosomal proteins, an alternative approach involving endogenous tagging of the ribosomal protein S3 (RPS3) within the 40S ribosome core was employed. This method also confirmed the signaling pathway alterations in breast cancer cells (**Figure S2**).

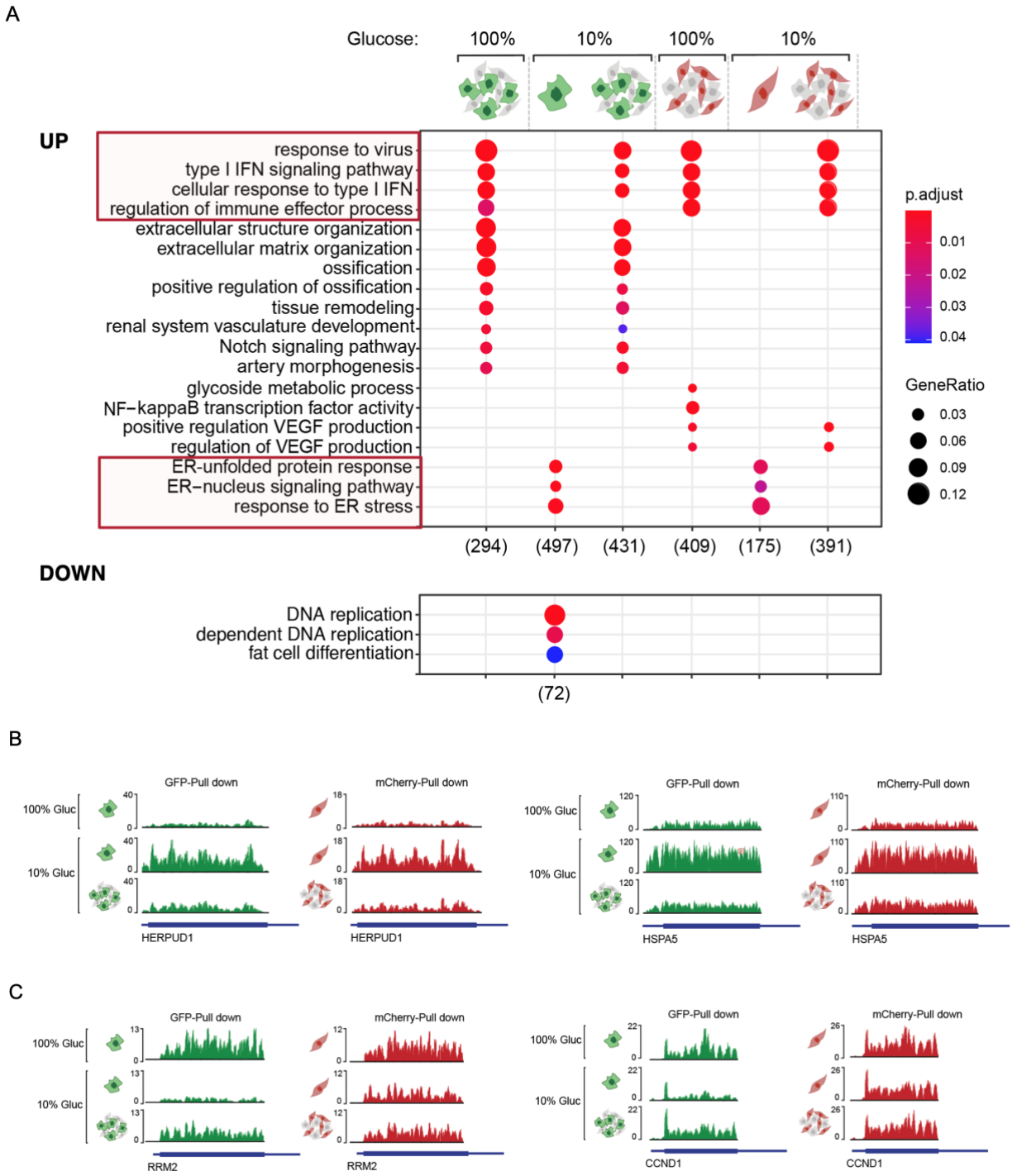

Figure 6 | DualRP unravels signaling pathway deregulation under glucose starvation *in vitro*. (**A**) Landscape of signaling pathway alterations determined by DualRP using clusterprofiler. Red regions indicate the activation of IFN signaling and rescue of ER-stress under glucose starvation in co-cultured cells. Dot size: number of differentially expressed genes for each pathway (gene ratio). Color: adjusted P value to the set of all family comparisons. (**B**) Expression of specific ER-stress genes is restored in co-culture. (**C**) Downregulation of cell cycle and DNA replication genes in cancer cells is alleviated by co-culture interactions.

4.1.5 IFN signaling modulates lysosomal activity and the nutrient stress response

Since both signaling pathway alterations derived from the co-culture, I evaluated the contribution of IFN-type I signaling in the rescue of the nutrient stress response. First, conditioned media from fibroblasts was collected under low glucose and in the presence of recombinant interferon beta (IFNβ) (**Figure 7A**). In breast cancer cells, IFN was able to rescue the expression of the activating transcription factor 4 (ATF4) targets: DNA damage-inducible transcript 3 (DIIT3, also known as CHOP) and asparagine synthetase (ASNS) that were used as read out for the nutrient stress response. In line with these results, impairment of IFN-I signaling via STAT1 in fibroblasts, led to the increased expression of the same target genes (**Figure 7B**). Moreover, using the same DualRP dataset, a group of IFN target genes linked to lysosomal activity was upregulated exclusively in co-cultured cells (**Figure S3**).

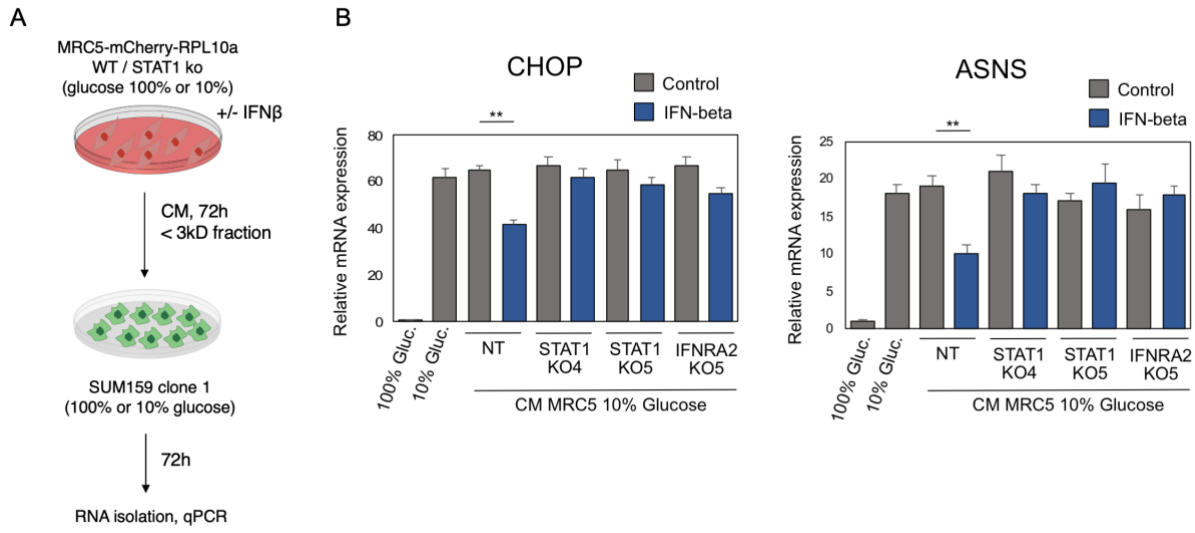

Figure 7 | IFN signaling in fibroblasts impacts the rescue to nutrient stress in breast cancer cells. (**A**) Diagram of conditioned media (CM) collection from wild-type and STAT1 knock out MRC5 fibroblasts after IFNβ treatment. Upon incubation in CM, total RNA was extracted from SUM159 cells for qPCR analysis. (**B**) Expression of ATF4 target genes CHOP and ASNS in breast cancer cells under low glucose levels is attenuated by IFNβ, and increased when IFN signaling is blocked in fibroblasts.

To explore the role of IFN signaling in lysosomal activity, fibroblasts were co-cultured with breast cancer cells and the pH-dependent fluorescent cleavage of an extracellular protein source (dqBSA) was quantified in collaboration with Edoardo Ratto at DKFZ. Once internalized into lysosomes, the dqBSA fluorescent cleavage reflected the extent of lysosomal proteolysis, that was substantially increased when fibroblasts were in contact with cancer cells but blocked when IFN signaling was impaired.

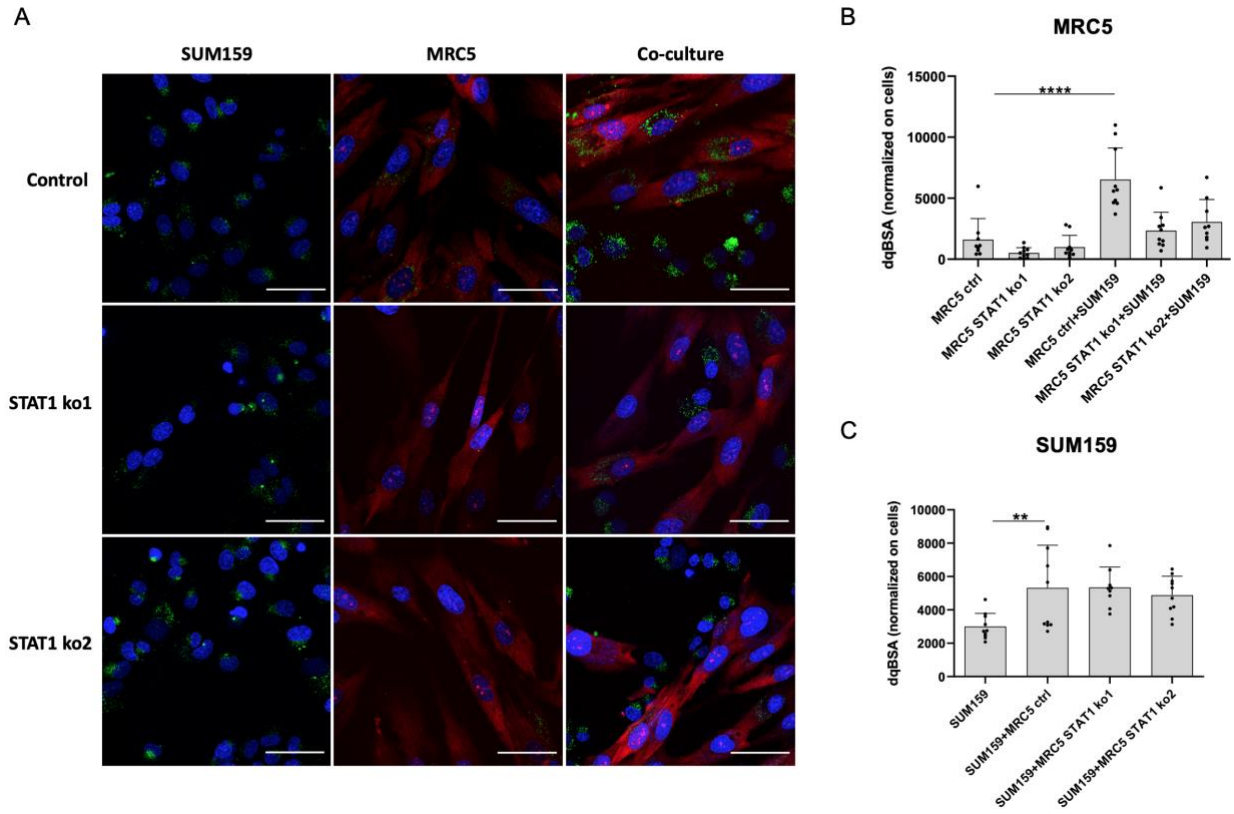

Figure 8 | IFN signaling via STAT1 constraints lysosomal activity in co-culture. (**A**) Representative confocal microscopy images of dqBSA (green) cleavage in lysosomes, showing increased lysosomal activity in co-culture, which is reduced in STAT1 knock outs. Scale bar: 50 µm. (**B**) Quantification of dqBSA fluorescence normalized to cell number in MRC5 fibroblasts and (**C**) SUM159 cancer cells in co-culture. SD from 10 different fields of view.

4.1.6 Diricore reveals amino acid limitations in fibroblasts and breast cancer cells

To uncover potential amino acid limitations from glucose deficiency, differential ribosome codon reading (diricore) was applied to the current DualRP *in vitro* system. Sub-sequence analysis revealed ribosome stalling in glycine codons under low glucose in both cancer cells and fibroblasts, with no evident rescue upon co-culture. In contrast, glucose-deprived cancer cells displayed ribosomal stalling in alanine codons, which was rescued in co-culture with fibroblasts (**Figure 9**). Meanwhile, the addition of alanine or extracellular protein (BSA) alone had minimal impact on the occupancy of alanine codons in glucose-starved breast cancer cells. Conversely, extracellular vesicles (EV) isolated from fibroblasts led to a more pronounced alanine rescue in cancer cells (**Figure S4**).

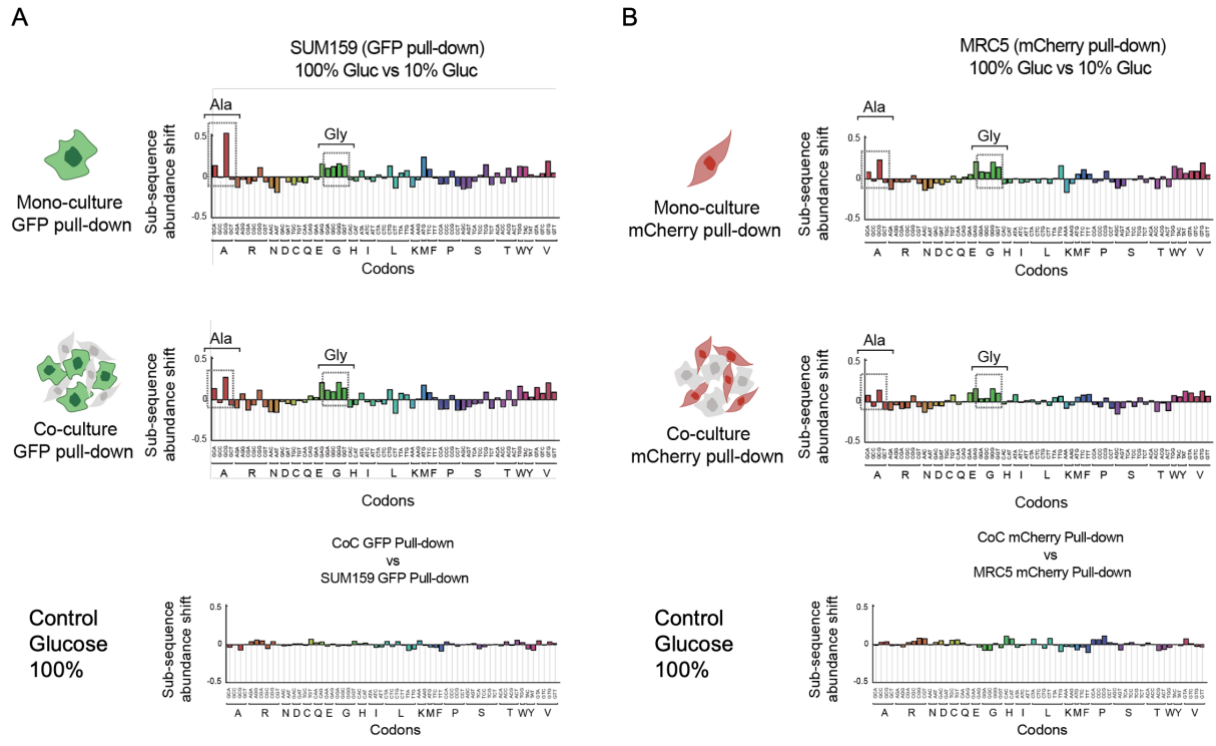

Figure 9 | Diricore uncovers amino acid limitations in fibroblasts and breast cancer cells from DualRP *in vitro*. Diricore sub-sequence analysis depicts ribosome stalling in glycine codons upon glucose starvation in single and co-culture, whereas stalling in alanine codons is rescued in co-culture in (**A**) breast cancer cells and (**B**) fibroblasts.

4.1.6 Validation of amino acid limitations with Dual-RP in vivo

To translate Dual-RP *in vivo*, mice tailored-xenografts were injected with the human ribo-tag lines (**Figure 10A**). Remarkably, tumor growth was benefited from the co-injection of breast cancer cells with fibroblasts, as opposed to only injecting cancer cells. Moreover, the largest tumor volumes were observed after injecting "primed" cells that had been co-cultured with fibroblasts for three days (**Figure 10B**). In terms of diricore analysis, the tumors resembled the alanine limitation already seen in cancer cells, which was also rescued by co-injection with fibroblasts (**Figure 10C**). At this stage, the validation of DualRP has extended to *in vivo* experiments, yielding consistent results that closely resemble the findings observed *in vitro*.

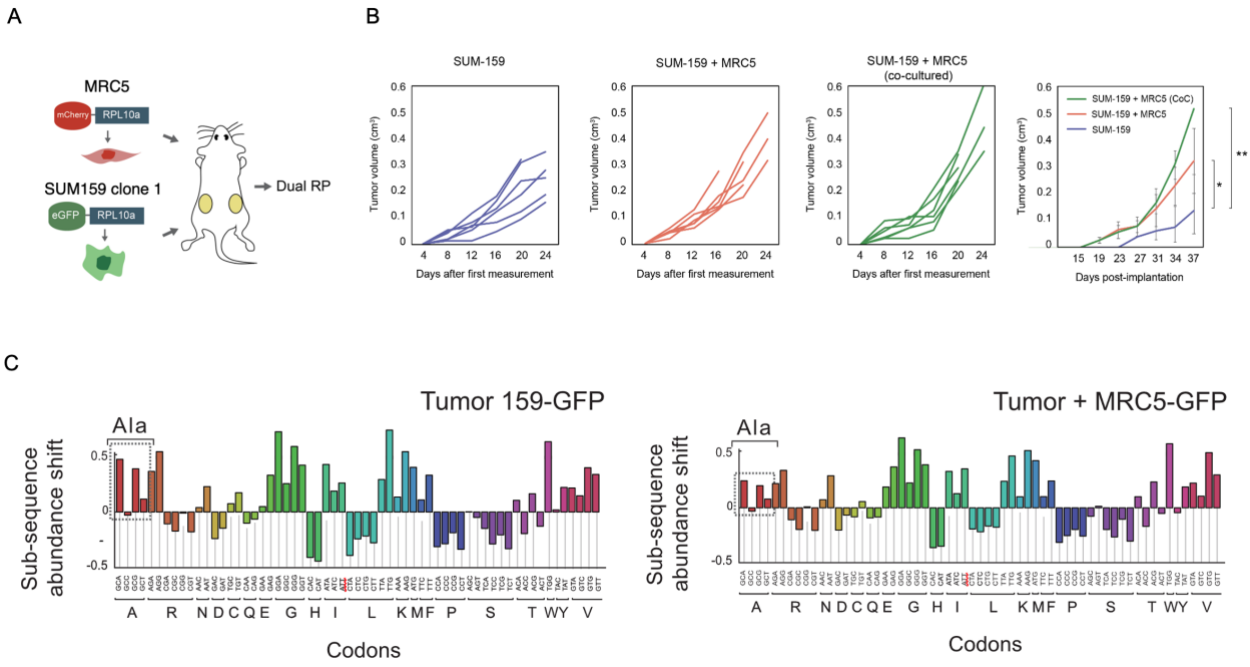

Figure 10 | Evolution of tumor growth and amino acid limitations in vivo. (**A**) Schematic representation of DualRP tailored xenografts. (**B**) Progression of tumor volume overtime in mice injected with SUM159 cells alone, co-injected with MRC5 fibroblasts (1:2 ratio) or after 72h co-culture (1:2 ratio). (**C**) Diricore sub-sequence analysis of tumor tissue shows stalling in alanine codons in cancer cell fraction (left panel) that is compensated in tumors where cancer cells and fibroblasts were co-injected (right panel).

4.2 T cells and breast cancer interactions

4.2.1 Characterization of the immune response with DualRP

In order to uncover metabolic limitations in T cells from TNBC tumors, I employed a previously characterized Ribo-Tag transgenic mouse model. In this model, a Ribo-tag mutation of the ribosomal protein L22 (RPL22) locus allows for Cre-mediated hemagglutinin (HA) epitope tagging of ribosomes when crossed with a Cre recombinase driver mouse. Here, transgenic Ribo-Tag mice were crossed with CD4-Cre mice to specifically investigate the T cell population. The resulting offspring, RPL22HA:CD4Cre, were injected with the syngeneic TNBC E0771 cell line carrying the homozygous expression of GFP-RPL10a (**Figure 11**).

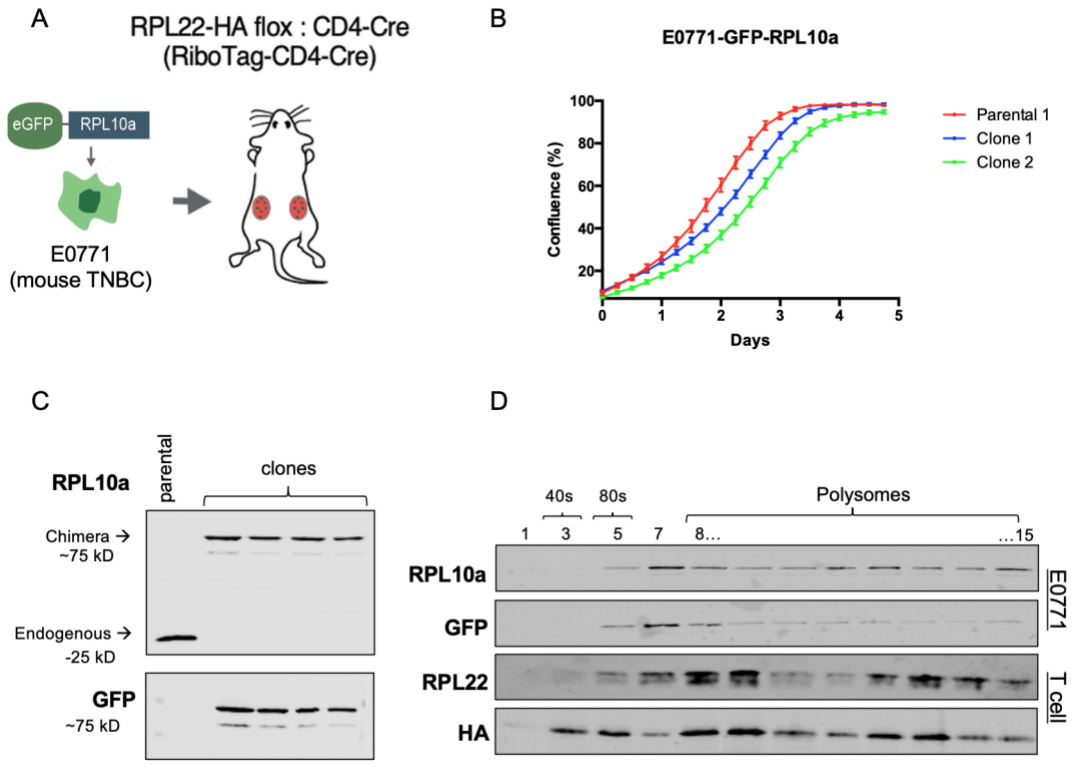

Figure 11 | DualRP-tailored mouse model to evaluate the immune response. (**A**) The Dual-RP transgenic harbors RPL22 tagged with HA in CD4+ T cells (RPL22HA : CD4Cre) and TNBC syngeneic tumors expressing eGFP-RPL10a. (**B**) Proliferation curves of E0771 clones, SD are plotted from 5 technical replicates. (**C**) Endogenous expression of fluorescent RPL10a in clones of E0771 (**D**) Ribosomal tagging is incorporated into translating polysomes on E0771 cancer cells and T cells from RPL22HA : CD4Cre mouse.

After comparing the diricore profiles of tumor cells to the E0771 cell line in culture, ribosome stalling was observed in proline, aspartic acid, glutamic acid, and isoleucine codons. In contrast, when comparing tumor-infiltrating T cells to naive splenocytes, limitations in alanine, aspartic acid, glycine, and serine were found (**Figure 12**). Furthermore, the analysis of the global gene expression of the syngeneic tumors indicated that the transcriptional programs of the T cell fraction differ from those of the cancer cell counterpart (**Figure S5A**). For instance, only the T cells within the tumor showed downregulation of activation and proliferation programs. (**Figure S5B**). Taken together, DualRP serves to simultaneously address metabolic vulnerabilities in tumor-infiltrating T cells and cancer cells.

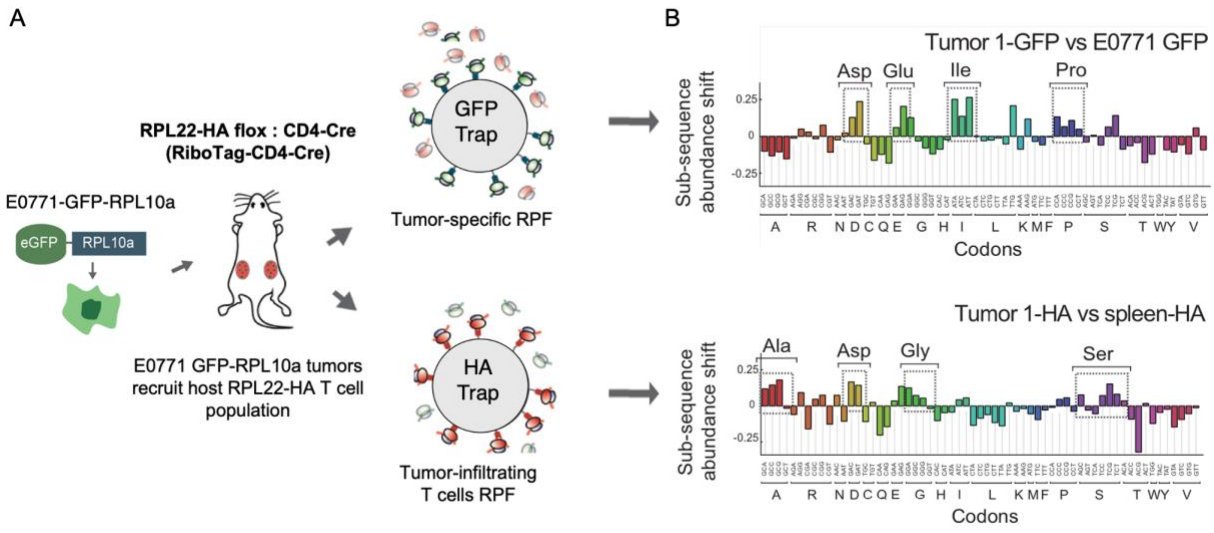

Figure 12 | T cells and breast cancer cells show distinct amino acid limitations *in vivo*. (**A**) Schematic representation of DualRP transgenic model and RPF isolation from T cell and cancer cell compartments in TNBC tumors. (**B**) Diricore sub-sequence analysis of tumor tissue shows stalling in different codons in cancer cell fraction (upper panel) and T cell fraction (right panel).

4.2.2 DualRP reveals amino acid limitations in breast cancer and tumor-infiltrating T cells in response to check-point inhibition

To further explore the metabolic vulnerabilities of T cells and cancer cells in a therapeutic setting, I studied the same DualRP transgenic model under anti-PD1 treatment (**Figure 13A**). In comparison to the IgG control, tumors from mice receiving

anti-PD1 displayed ribosome stalling in alanine, aspartic acid, serine and glycine codons in T cells, whereas cancer cells presented limitations in phenylalanine and leucine (**Figure 13B**). The connections between amino acid metabolism and the exposed limitations of each tumor compartment will take part of the discussion of this thesis. However, based on the current experiment, there is a high demand for specific amino acids such as serine and glycine in tumor-infiltrating T cells following checkpoint inhibition. In this regard, I continued to validate the effects of these limitations in overall T cell function.

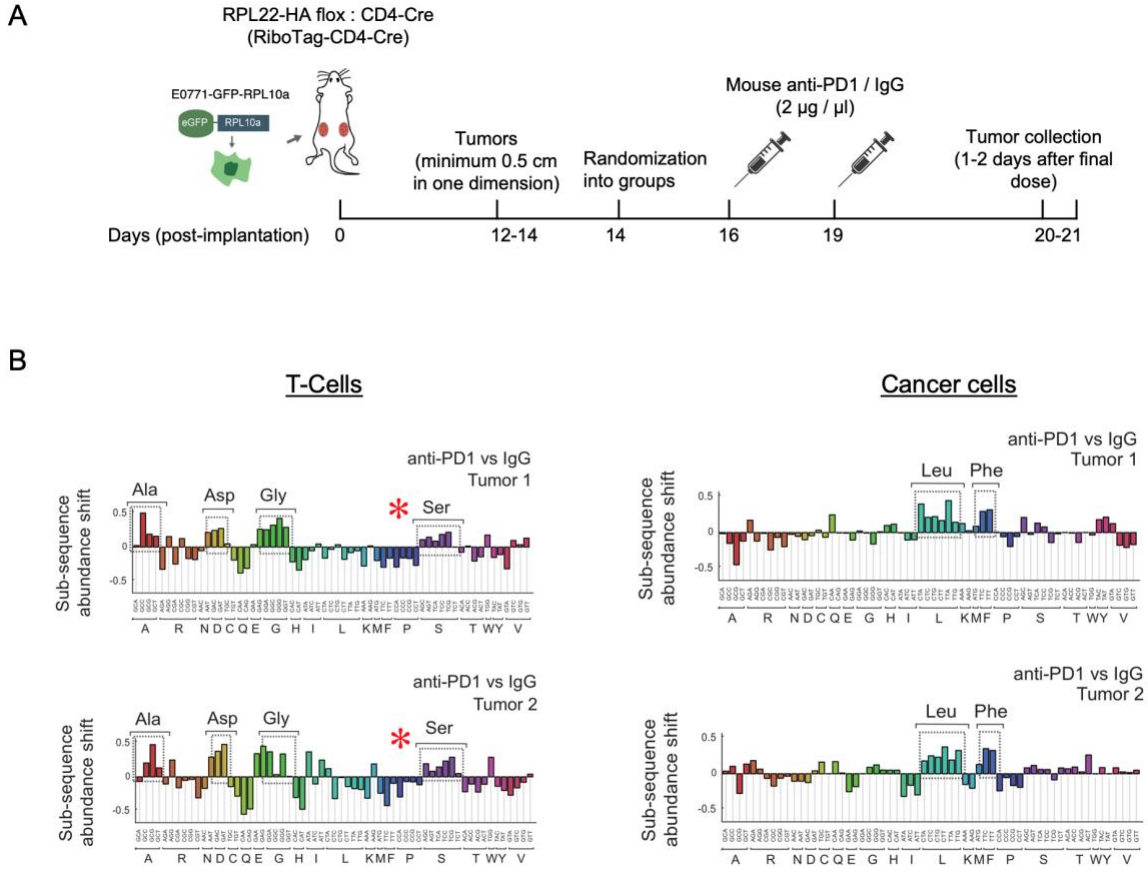

Figure 13 | DualRP uncovers amino acid limitations in tumor bearer mice after checkpoint inhibition. (**A**) Experimental design of the transgenic Dual-RP model treated with checkpoint inhibitor (anti-PD1) or control (IgG). (**B**) Diricore sub-sequence analysis shows ribosomal stalling in specific amino acid codons of cancer and T cell tumor compartments treated with anti-PD1 versus IgG. Two biological replicates are presented.

4.2.3 Serine supports T cell activation and their killing efficiency

To evaluate if T cell-dependent cancer killing is benefited from increasing serine supply, I worked with an antigen-specific T cell assay *ex vivo*. For this assay, T cells were freshly isolated from OT-I transgenic mice expressing a T cell receptor (TCR) that recognizes ovalbumin (OVA) residues 257-264 in the context of H2Kb. After T cell co-culture with OVA-expressing murine cancer lines, cancer cell survival was quantified by crystal violet staining and converted to T cell killing efficiency, where the negative control (only cancer cells) represents no killing (**Figure 14**). Notably, serine improved T cell killing efficiency of cancer cells in TNBC, lung cancer and melanoma lines.

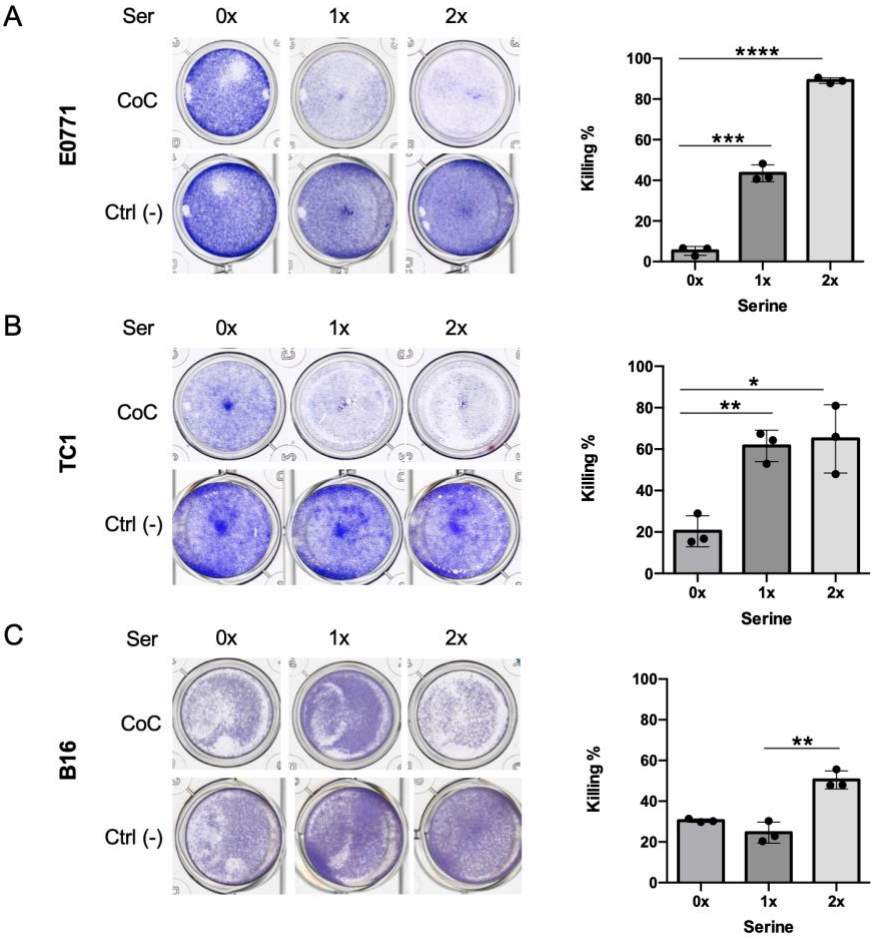

Figure 14 | Impact of serine in T cell killing efficiency. Cancer cell survival of OVA expressing (**A**) TNBC (**B**) lung cancer and (**C**) melanoma lines after co-culture with OT-I T cells for 24h. Cell killing assay is performed at increasing concentrations of serine. 1x in RPMI: serine (285 uM) and glycine (133 uM). Note: 0x represents absolute serine/glycine withdrawal, since serine is also synthesized from glycine. Crystal violet staining of representative wells (left) and quantification of killing efficiency of biological triplicates (right). P<0.0001 (****), P=0.0001 (***), P< 0.01 (**), P= 0.01 (*).

Moreover, T cell activation was enhanced in the presence of serine and glycine, as evidenced by the increased release of inflammatory cytokines such as interferon gamma (IFNγ) and granzyme B (GZB) during co-culture with cancer cells compared to naïve T cells (**Figure 15**).

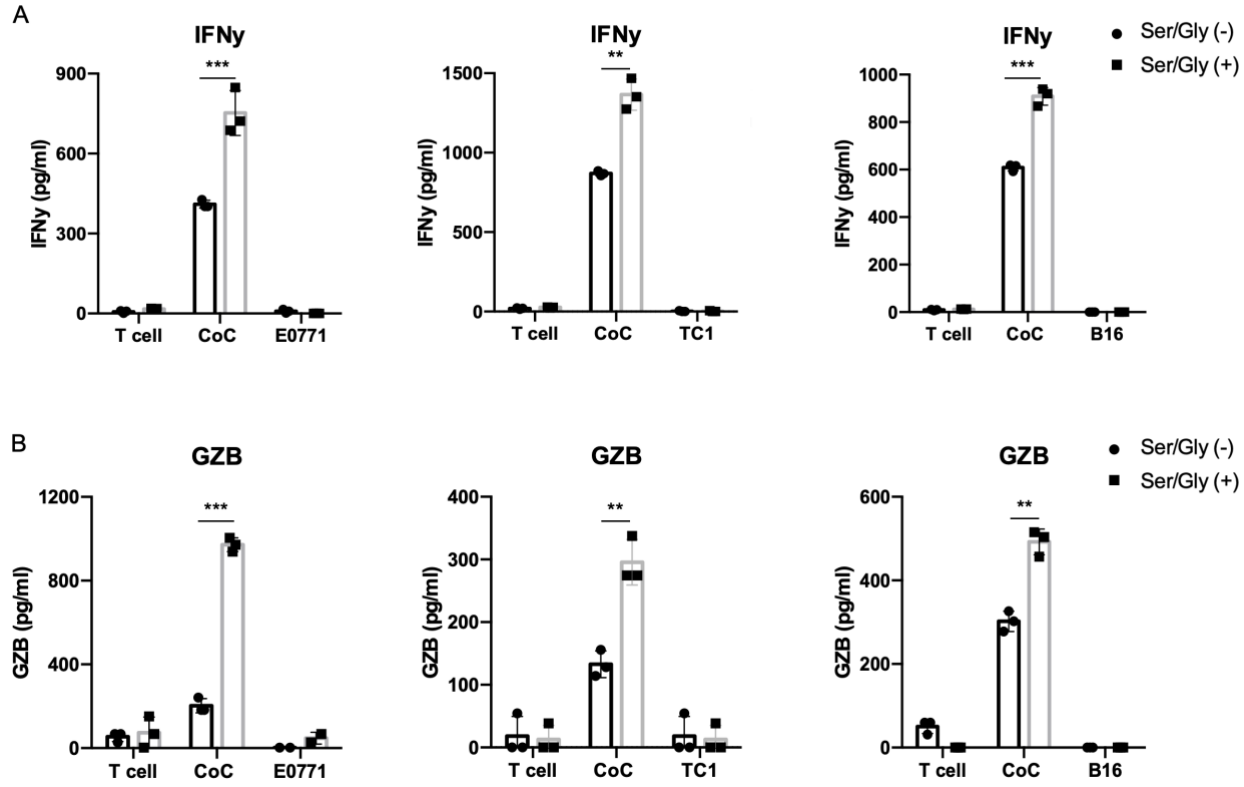

Figure 15 | Serine and glycine support cytokine release in activated T cells. Quantification of cytokine release by ELISA in cell supernatant with and without serine/glycine in naïve OT-I T cells and after co-culture with cancer cells. 1x in RPMI: serine (285 uM) and glycine (133 uM) (**A**) Interferon gamma (IFNγ) and (**B**) Granzyme B (GZB) in pg/ml of cell supernatant from 3 independent measurements. P<0.001 (***), P< 0.005(**).

4.2.4 T cells upregulate serine and glycine metabolism after cancer cell presentation

The key metabolic enzymes in serine and glycine metabolism include phosphoglycerate dehydrogenase (*PHGDH*), phosphoserine aminotransferase 1 (*PSAT1*), phosphoserine phosphatase (*PSPH*) and serine hydroxymethyltransferase (*SHMT*) (**Figure 17B**). To continue investigating alterations in the serine biosynthesis pathway, I adapted a co-culture system to retrieve the gene expression signatures from T cells and cancer cells (**Figure 16A**).

This experiment underlines the activation of serine biosynthesis genes *PHGDH*, *PSAT* and *PSPH* in T cells but not in cancer cells upon co-culture (**Figure 16D**). In addition, *SHMT1* and *SHMT2*, which are responsible for the interconversion of serine and glycine entering the folate cycle in the cytoplasm and mitochondria, showed a sustained increase in co-cultured T cells but not in cancer cells (**Figure S6A**).

The observed effects in serine and glycine metabolism are consequence of T cell activation, since the mRNA expression levels of *IFNγ* and *GZB* were upregulated in co-culture conditions but not in naïve T cells. (**Figure S6B**). In line with the gene expression levels, protein levels of PHGDH and SHMT1 were upregulated in co-culture with cancer lines (**Figure 17C**). Notably, DualRP *in vivo* showed a pronounced upregulation of both genes in the T cell fraction from syngeneic tumors of mice receiving check-point inhibition (**Figure 17A**).

In addition, the potential of PHGDH as a biomarker to predict the response to immunotherapy was tested using a publicly available T cell signature framework called TIDE[114]. The outcome of checkpoint inhibition was monitored in the METABRIC patient repository. Interestingly, TIDE analysis revealed that high expression of PHGDH in cytotoxic T cells within breast tumors correlated with better patient survival rates (**Figure 17D**).

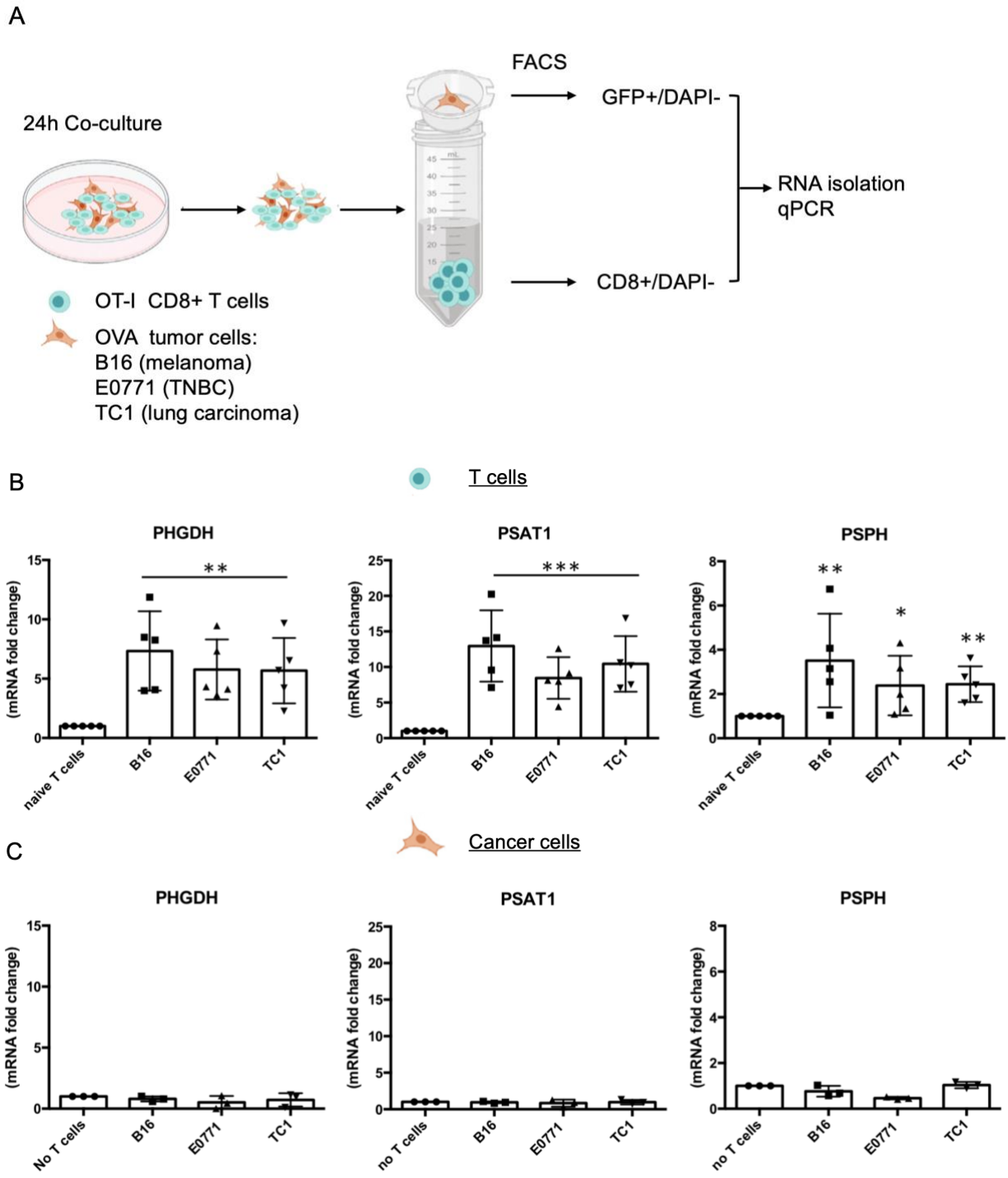

Figure 16 | T cells upregulate serine biosynthesis upon cancer cell presentation. (**A**) Schematic representation of cancer cell and T cell separation in co-culture adapted from Elia *et al*., 2022. (**B**) mRNA expression of serine biosynthesis genes in naïve T cells versus co-cultured T cells with cancer lines (**C**) mRNA expression of the same genes in cancer cells and after co-culture with T cells. Fold change is plotted from at least 3 biological replicates. P<0.001 (***), P< 0.005(**), P< 0.05(*)

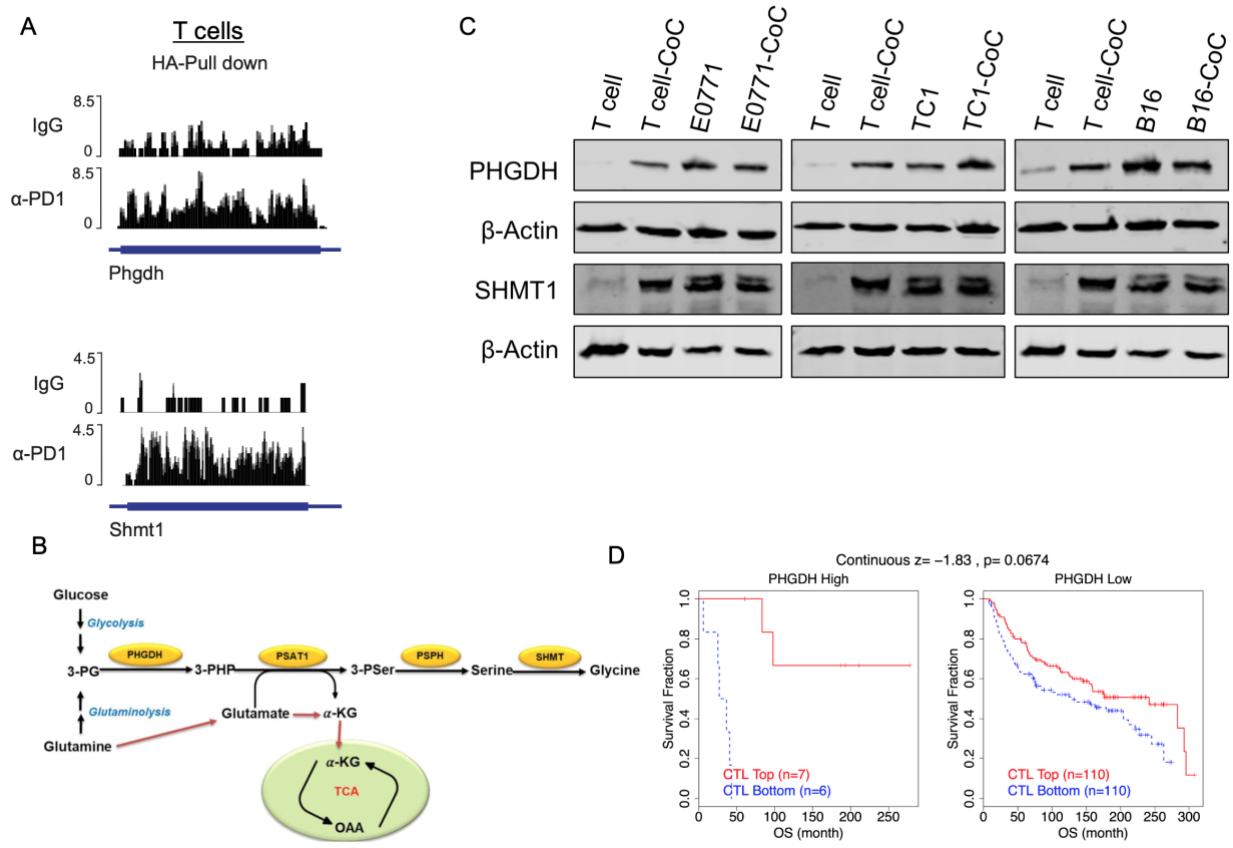

Figure 17 | Active T cells upregulate PHGDH and SHMT1 . (**A**) Upregulation of *PHGDH* and *SHMT1* in tumor-infiltrating T cells in mouse TNBC tumors. (**B**) Immunoblots of PHGDH and SHMT1 overexpression in T cells co-cultured with TNBC, lung cancer and melanoma lines. (**C**) The serine biosynthesis pathway adapted from Pan S. *et al.,* 2021. (**D**) Kaplan-Meier survival curves from METABRIC breast cancer patient repository analyzed using TIDE framework, Jiang P. *et al.,* 2018. Better survival rates were observed in patients with signatures of high infiltration of cytotoxic T lymphocytes (CTL) and high *PHGDH* expression.

4.2.5 Glucose tracing reveals increased serine/glycine biosynthesis in co-culture

To validate the contribution of glucose in serine and glycine production from T cells and cancer cells upon co-culture, $^{13}C_6$ Glucose tracing was performed in collaboration with Ilaria Elia at KU Leuven (**Figure 18**). Here, the increased serine and glycine production from glucose was observed only upon T cell activation. On the other hand, cancer cells maintain an evenly sustained glycine/serine biosynthesis in monoculture and co-culture.

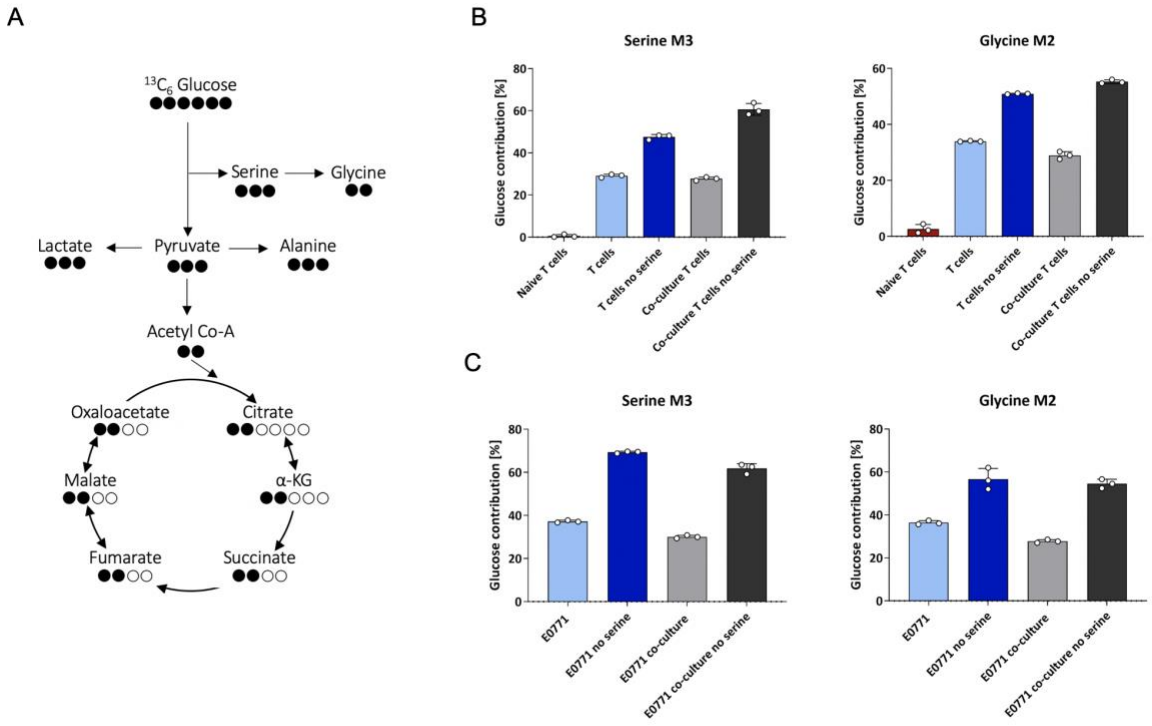

Figure 18 | T cell activation in co-culture triggers serine/glycine *de novo* biosynthesis. (**A**) Schematic representation of $^{13}C_6$ Glucose. Glucose contribution to serine and glycine production in T cells (**B**) and breast cancer cells (**C**) in co-culture.

4.2.6 Blocking PHGDH and SHMT1 impairs T cell killing efficiency

I continued to evaluate the role of PHGDH and SHMT1 in the overall killing capacity of T cells. This time, CRISPR-Cas9-mediated knockout of each target was performed using P14 x CD4-Cre x Rosa-Cas9-GFP mice (P14;Cas9). In this antigen-specific system, the P14 TCR recognizes the lymphocytic choriomeningitis virus (LCMV)-derived peptide, gp33 residues 33–41, presented in the context of H-2Db (**Figure 19A-C**). Indeed, blocking PHGDH or SHMT1 disrupted T cell-mediated killing of TNBC, melanoma, and lung carcinoma cell lines. (**Figure 19D-E**).

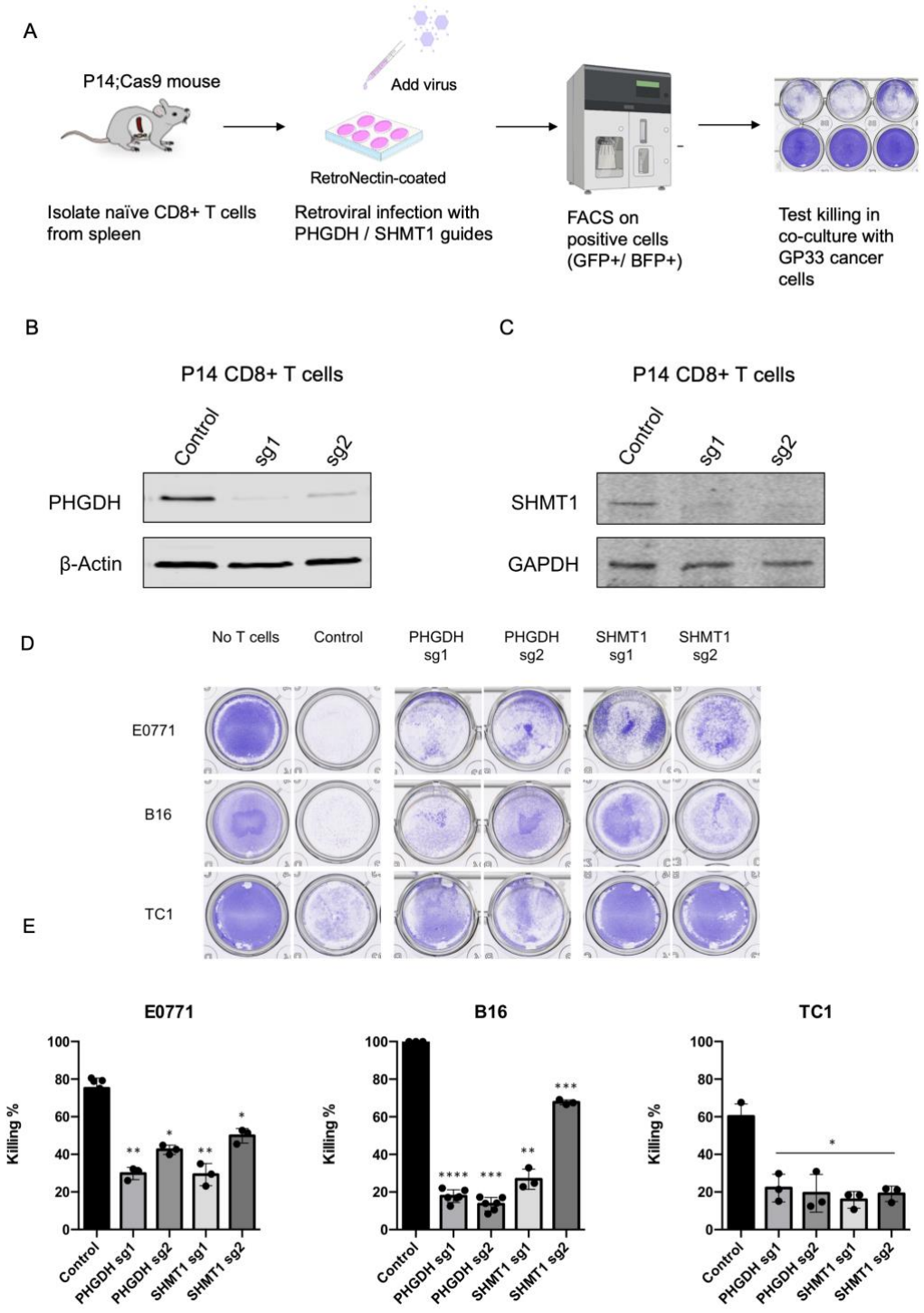

Figure 19 | Blocking of PHGDH and SHMT1 impairs T cell-dependent cancer killing. (**A**) T cell knock out generation in isolated T cells from P14;Cas9 mice. Immunoblots of (**B**) PHGDH and (**C**) SHMT1 from T cell knock outs. (**D**) Cancer cell survival from representative wells and (**E**) quantification of T cell killing efficiency from at least 3 replicates. T test values: P<0.0001 (****), P< 0.0005(***), P< 0.005(**), P< 0.05(*).

4.2.7 Serine/glycine dietary restriction in tumor-bearer mice has a negative effect on the response to checkpoint inhibition

As the previous results indicate, there is a notable contribution of serine and glycine metabolism to T cell function. Therefore, the impact of serine/glycine deprivation was tested in combination with checkpoint blockade in tumor-bearing mice (**Figure 20A**). As anticipated, the exclusion of serine and glycine from the diet had a detrimental effect on the response to immunotherapy. Specifically, animals on serine/glycine restriction developed larger tumors despite the use of anti-PD1, resulting in poor survival rates compared to animals on a full diet (**Figure 20B-C**). Importantly, the effect of the diet alone did not affect the overall survival of the animals, as both formulations were equicaloric, and serine and glycine can still be synthesized from glucose or glutamine.

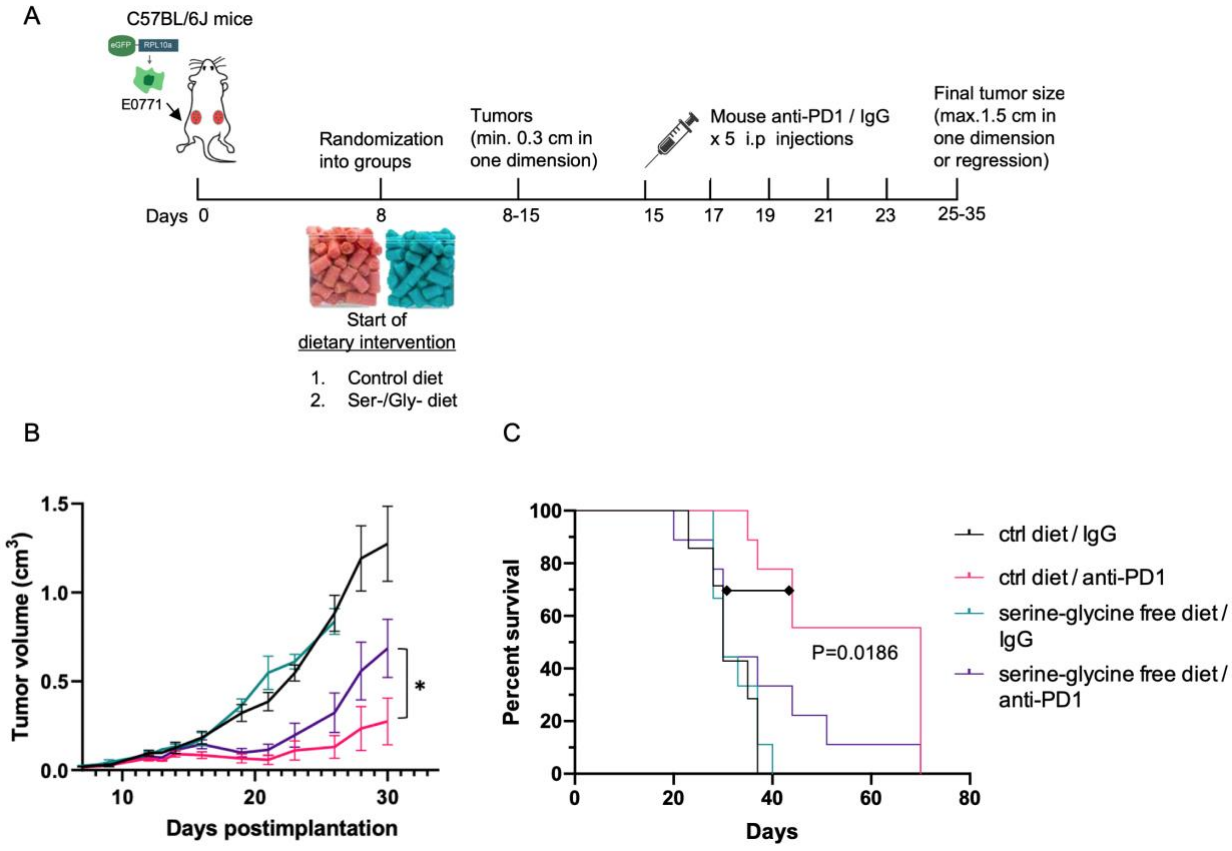

Figure 20 | Serine/glycine dietary restriction negatively affects the response to checkpoint blockade. (**A**) Therapy scheme showing the combination of dietary restriction and anti-PD1 in immunocompetent mice with TNBC tumors. (**B**) Evolution of tumor growth after E0771 injection, (*) $P<0.05$ by two-way ANOVA for tumor volumes of at least 5 mice receiving anti-PD1 treatment with different diets. (**C**). Mice survival curves with P value calculated by Gehan Breslow Wilcoxon test. Same color code is assigned to B and C.

V. Discussion

5.1 Establishing DualRP for the study of TME interactions

The quest for novel approaches to investigate the metabolic reprogramming in the naïve state of the tumor microenvironment (TME) has inspired the concept of dual-ribosome profiling (DualRP). Here, I present DualRP as a system for uncovering cell-type specific metabolic limitations in interacting populations, that does not require cell sorting or disruption of the naïve cell interactions.

Since DualRP is based on ribosome profiling, it offers a snapshot of the translatome from different TME populations that may reveal important regulatory cues for cancer therapy. One type of cancer that lacks targeted therapy options is triple-negative breast cancer (TNBC), that accounts up to 20% of the most commonly diagnosed cancer worldwide[3,9]. Fibroblasts are predominant component of the TME and play an essential role in tumor growth and metastasis[64]. Therefore, I started a DualRP co-culture system using the human TNBC cell line SUM159 PT and MRC5 fibroblasts.

For breast cancer cells, eGFP-tag was introduced via homozygous CRISPR knock-in[110] of the 60S ribosomal protein L10a (RPL10a). This method required a Cas9D10A nickase mutant and paired gRNAs for the introduction of DNA double-stand breaks (DSB) in the RPL10a locus while GFP was integrated via homology-directed repair (HDR). As a consequence, several cancer cell clones were obtained expressing endogenous eGFP-RPL10a (**Figure 3**). However, generating homozygous clones in fibroblasts proved to be technically challenging. This could be due to lower HDR efficiency compared to cancer cells, as healthy mammalian cells preferentially employ non-homologous end joining (NHEJ) over HDR to repair DSB throughout the cell cycle[115]. As an alternative to tag fibroblasts, lentiviral transduction with mCherry-RPL10a was performed.

Regardless of the tagging method, proper incorporation of the RPL10a chimera into polysomes was observed in fibroblasts and cancer cells. Importantly, the introduction of the ribosomal tag did not significantly impaired cell proliferation (**Figure 3**). Furthermore, the global gene expression patterns from the endogenously-tagged

clone resembled the parental control. At the same time, the ribosome pull-down method positively correlated with the 'gold standard' of ribosome isolation via sucrose gradient (**Figure 4**). The most significant aspect of this validation, was that DualRP successfully captured the global gene expression from cell-to-cell contact interactions. This was evident from the principal component analysis, where the gene expression profiles of co-cultured cells exhibited a distinct separation from those of the after-lysis mix and single controls (**Figure 5**).

5.2 DualRP exposes signaling pathway alterations in fibroblasts and breast cancer cells under nutrient stress

The competition for nutrients in the TME rewires a plethora of signaling pathways to sustain tumor growth[27]. To mimic the limited availability of glucose in the TME, breast cancer cells and fibroblasts were co-cultured under low glucose concentrations. Here, DualRP revealed the deregulation of multiple signaling pathways on fibroblasts and breast cancer cells simultaneously (**Figure 6**).

At first glance, the pronounced upregulation of interferon (IFN) responses, particularly IFN type I and antiviral signaling, was triggered in both cell types in co-culture. This aligns with previous findings, where RNA within exosomes is transferred from stromal to breast cancer cells and stimulates the pattern recognition receptor (RIG-I) to activate STAT1-dependent antiviral signaling[116]. Specifically in TNBC, CAFs induced the activation of IFN signaling to confer chemotherapy resistance[117].

In breast cancer cells, contact with fibroblasts led to the upregulation of multiple pathways, including extracellular matrix (ECM) organization, Wnt signaling, and Notch signaling. It is well known that cancer cells remodel the ECM through the production of metalloproteinases, favouring metastasis[118]. Furthermore, the induction of Notch signaling by cell-cell contact plays a pivotal role in promoting angiogenesis and therapy resistance[119]. Meanwhile, aberrant Wnt signaling is a hallmark of many cancers, and exerts significant influence on cell fate, differentiation, proliferation, and stem cell pluripotency[120].

In contrast, fibroblasts in contact with breast cancer cells enhanced the activity of the nuclear Factor-kappa B (NFκβ) and the vascular endothelial growth factor (VEGF) signaling. Indeed, cancer cells promote NF-κB activation in adjacent fibroblasts, which is crucial for tumor inflammation and macrophage recruitment mediated by CAFs[121]. Likewise, VEGF signaling in fibroblasts exerts angiogenesis and tumor neovascularization[122]. Furthermore, the downregulation of cell cycle and DNA replication genes under glucose deprivation was observed in cancer cells alone, but it did not affect them in co-culture, confirming the role of fibroblasts in supporting cancer cell proliferation.

A striking observation was that co-culture interactions alone, restored the nutrient stress response in cancer cells and fibroblasts. This was shown by the rescue of ER-stress, that as a part of the integrated stress response, induces the activating transcription factor 4 (ATF4) under nutrient deprivation[123]. In the case of fibroblast and breast cancer interactions, this rescue pinpoints the existence of compensatory mechanisms to face nutrient deprivation.

5.3 IFN signaling modulates lysosomal activity and the nutrient stress response

The next step was to identify the mechanism behind the rescue of the nutrient stress response in co-cultured cancer cells and fibroblasts. Since IFN-I signaling was strongly upregulated in the same conditions, I hypothesized a possible connection of IFN to the rescue on nutrient stress. Interestingly, conditioned media from glucose-starved fibroblasts treated with IFNβ diminished the expression of the ATF4 targets, DNA damage-inducible transcript 3 (DIIT3, also known as CHOP) and asparagine synthetase (ASNS) in breast cancer cells. In line with these results, blocking IFN-I signaling via STAT1 knock out, led to the increased expression of the same ATF4 targets (**Figure 7**).

Most recently, non-canonical aspects of type I IFN signaling had shown its role in remodeling lysosomal function[124,125]. Notably, the same DualRP experiment under low glucose, showed the upregulation of IFN targets linked to lysosomal activity when breast cancer cells and fibroblasts interact (**Figure S3**).

To investigate the contribution of IFN signaling in lysosomal activity, the pH-dependent fluorescent cleavage of an extracellular protein source (dqBSA) was quantified. Once internalized into lysosomes, the dqBSA fluorescence reflected increased lysosomal proteolysis in co-cultured cancer cells and fibroblasts, which was suppressed when IFN signaling was impaired (**Figure 8**). Collectively, IFN signaling via STAT1 constraints lysosomal activity of fibroblasts and cancer cells in co-culture and impacts the rescue from the nutrient stress response.

5.4 DualRP paired with diricore reveals amino acid limitations in fibroblasts and breast cancer cells *in vitro* and *in vivo*

Another advantage of DualRP, is the uncovering of metabolic vulnerabilities as amino acid restrictions via diricore (**Figure 9**). Under low glucose conditions, ribosomal stalling in glycine codons was detected in both cell types. Since glucose is the major source for glycine biosynthesis[126], this confirms that diricore uncovers the most restrictive amino acids in cells. In contrast, the ribosome stalling in alanine codons on cancer cells, was only rescued in co-culture with fibroblasts. While alanine and glycine are both synthesized from glucose, alanine is mainly sourced from pyruvate entering the TCA cycle[127]. Since pyruvate can be synthesized from glutamine, an abundantly present amino acid in culture media, it is highly possible that fibroblast contact triggers glutaminolysis in cancer cells to fuel the TCA cycle[57]. Previous reports showed that upon co-culture, breast cancer cells upregulate TCA cycle and mitotic response genes, whereas CAF preferentially upregulate glycolysis and glycogenesis[128].

A possible alternative mechanism is that fibroblasts provide alanine to breast cancer cells in an autophagy-dependent manner. As others report in pancreatic cancer, CAFs support tumour metabolism through autophagic alanine secretion[129]. Nonetheless, providing alanine or extracellular protein (BSA) in glucose-deprived breast cancer cells did not significantly impact the ribosome stalling in alanine codons. In contrast, isolated extracellular vesicles (EV) from fibroblast-conditioned medium led to a more pronounced rescue in alanine (**Figure S4**). Compelling evidence has shown that CAF-derived exosomes are another means of nutrient transfer to cancer cells in the

TME[67,116,130]. Therefore, analysis of the specific EV-cargo in CAFs could provide interesting insights on the alanine rescue in breast cancer cells.

To further validate DualRP *in vivo*, mice tailored-xenografts were injected with the same ribosome tagged lines. Remarkably, tumor growth was enhanced when breast cancer cells were co-injected with fibroblasts, as opposed to injecting cancer cells alone. Additionally, the largest tumor volumes were observed after injecting "primed" cells that had been co-cultured for three days (**Figure 10**). As previously shown by DualRP *in vitro*, cancer cells in contact fibroblasts increased their ECM remodeling capacity and activated multiple oncogenic signaling cascades that ultimately support tumor growth (**Figure 6A**). In terms of diricore analysis, the tumors resembled the alanine limitation detected by DualRP *in vitro*, which was also reduced in co-injection with fibroblasts. Altogether, the use of DualRP has been established in a robust manner to obtain consistent data *in vitro* and *in vivo.*

5.5 Evaluation of the immune response with Dual-RP tailored models *in vivo*

It is well known that immune cells undergo reprogramming of the metabolism in the TME[89,91,131]. However, the specific metabolic limitations of immune cells in the naïve TME are yet not fully understood. In order to uncover immune cell metabolic limitations, I extended the use of DualRP to T cells in TNBC tumors. For this purpose, a previously characterized Ribo-Tag transgenic mouse tailored for T cell-specific ribosome tagging was generated. In principle, traditional Ribo-tag mice express a mutation of the ribosomal protein L22 (RPL22) locus that allows the hemagglutinin (HA) epitope tagging of ribosomes when crossed with a Cre-recombinase driver mouse[101]. Therefore, to specifically investigate the T cell population, transgenic Ribo-Tag were crossed to CD4-Cre mice: RPL22HA x CD4Cre. To retrieve the T cell signatures from tumors, RPL22HA x CD4Cre mice were injected with the syngeneic TNBC E0771 line expressing homozygous GFP-RPL10a.

As part of the validation of DualRP, principal component analysis was conducted on the global gene expression data, revealing two distinct clusters within the tumors, one representing T cells and the other representing cancer cells (**Figure S5**). Gene

ontology analysis further supported these findings by confirming the downregulation of T cell activation programs in tumor-infiltrating T cells, indicating an immunosuppressed TME.

When comparing the diricore profiles from tumor cells to E0771 cells in culture, ribosome stalling was observed in proline, aspartate, glutamate and isoleucine codons. These findings correlate with previous reports where diricore detected tumor-specific proline vulnerability in breast cancer[103]. In cancer, proline availability supports ECM remodeling by collagen production[105]. Interestingly, glutamine-derived glutamate is also a precursor for proline biosynthesis[132]. Glutamate along with aspartate are substrates for *de novo* pyrimidine biosynthesis, which cancer cells rely on to ensure a continuous supply of deoxyribonucleoside triphosphates (dNTPs)[133,134].

On the other hand, cancer cells increase the uptake of branch-chain amino acids (BCAA; leucine, isoleucine and valine) from the TME[135]. BCAAs can activate mTORC1 signalling, which stimulates cancer protein translation, growth, and survival[136]. However, ribosome stalling in isoleucine but not leucine or valine codons remains puzzling. It should also be considered that culture conditions greatly differ from the physiological levels of amino acids. For example, the concentration of BCAA in Dulbecco's Modified Eagle Medium (DMEM) is 800 µM, compared to the (~50-200 µM) plasma physiological conditions[137].

In the case of immune cells, when diricore profiles from tumor-infiltrating T cells were compared to those of naïve splenocytes, limitations in alanine, aspartate, glycine and serine were detected. Since cancer cells often compete with immune cells for extracellular nutrients, this may reflect in the observed amino acid limitations. For instance, extracellular alanine is required during T-cell activation and memory T-cell restimulation[138]. By taking in exogenous alanine, T cells may conserve oxidized carbon for more pressing needs, including synthesis of aspartate[138]. The malate-aspartate shuttle is another transport system required to maintain synthesis of aspartate, which is necessary for the activation and differentiation of naïve T cells[139]. Even in glucose concentrations that are sufficient to support T cell activation, T cell expansion requires extracellular serine. This is because serine serves as a source of

glycine and one-carbon units for *de novo* nucleotide biosynthesis in proliferating T cells[140].

However, the significance of these amino acid limitations can only be accurately assessed within the context of therapy. Clinical trials have demonstrated promising outcomes in TNBC patients receiving immune checkpoint blockade[141]. To investigate the metabolic vulnerabilities of T cells under checkpoint inhibition, the same DualRP-tailored transgenic model was treated with an anti-PD1 murine antibody.

Interestingly, cancer cells from anti-PD1 treated tumors, displayed limitations in phenylalanine and leucine. A well described mechanism, is that activated T cells in the TME secrete interferon-γ (IFNγ), which induces the expression of indoleamine 2,3-dioxygenase 1 (IDO1) in cancer cells[142]. Conversely, IDO1 catabolizes tryptophan to generate metabolites along the kynurenine pathway to subvert T cell immunity, triggering a tryptophan limitation.[143] However, a more recent mechanism involving codon reassignment has been reported, wherein cancer cells produce proteins where phenylalanine is replaced with tryptophan when immune cells trigger a tryptophan shortage[144]. Leucine limitation confirms the high demand of BCAA in cancer cells and may be explored in the scope of future research[104,135,145].

Consistent with the previous diricore analysis, ribosome stalling in alanine, aspartate, serine and glycine was seen in T cells from tumors under checkpoint blockade. To explore if immunotherapy response is influenced by serine and glycine on the diet, I first validated the role of serine and glycine in T cell function *ex vivo* in different types of cancer.

5.6 Serine and glycine support T cell-dependent cancer killing

To evaluate if T cell-dependent cancer killing improves from extracellular serine, I performed T cell killing assays *ex vivo* with increasing concentrations of serine using the OVA-OTI antigen presentation system. Here, T cells from OT-I transgenic mouse recognize the 257-264 residues of OVA expressing cancer lines in the context of H-2Kb presentation[146]. Notably, T cell killing efficiency was substantially improved from higher concentrations of serine, particularly in TNBC and lung cancer lines. While T

cell killing was improved at higher serine levels, melanoma cells alone were also more dependent on serine to proliferate[147]. As already mentioned, serine serves as a source of glycine and one-carbon units for *de novo* nucleotide biosynthesis[126]. However, serine can also be made in the mitochondria from two glycine units. Since serine and glycine are interconvertible, these assays were compared to absolute serine/glycine withdrawal. Moreover, OT-I T cell activation was enhanced by the presence of serine/glycine, as shown by the secretion of pro-inflammatory cytokines such as interferon gamma (IFNγ) and granzyme B (GZB) upon contact with OVA-cancer cells (**Figure 15**).

5.7 The serine-glycine metabolic network is critical for T cell function

Serine biosynthesis and serine/glycine one-carbon metabolism constitute a crucial network to sustain multiple cellular processes including nucleotide biosynthesis, redox homeostasis and DNA/histone methylation[126,148]. The key metabolic enzymes in serine and glycine metabolism include phosphoglycerate dehydrogenase (PHGDH), phosphoserine aminotransferase 1 (PSAT1), phosphoserine phosphatase (PSPH) and serine hydroxymethyltransferase 1/2 (SHMT1/2) (**Figure 17**).

Upon activation, T cells upregulate enzymes of the serine, glycine, one-carbon metabolic network, and rapidly increase processing of serine into one-carbon metabolism[140]. Therefore, I adapted a co-culture system to validate the preferential activation in the serine-glycine metabolic network of interacting T cells and cancer cells. As shown by gene expression levels, the activation of serine biosynthesis genes in co-cultured T cells is enhanced compared to cancer cells (**Figure 16**). Furthermore, the expression of SHMT1 and SHMT2, which are responsible of the interconversion of serine to glycine entering the folate cycle in the cytoplasm and mitochondria[149], were upregulated in co-cultured T cells but not in cancer cells (**Figure S6**). The production of serine/glycine was also corroborated via $^{13}C_6$ glucose tracing (**Figure 18**). Here, the activation of T cells in co-culture led to the increase in serine/glycine biosynthesis in comparison to cancer cells that keep a constant flux independent of T cell-mediated killing. In line with these findings, enhanced expression of PHGDH and SHMT1 was exclusively found in the T cell fraction of the TNBC syngeneic tumors under checkpoint blockade (**Figure 17**).

Consequently, I evaluated the role of PHGDH and SHMT1 in the overall killing capacity of T cells via CRISPR-Cas9 mediated knock out of each target using the P14 x CD4-Cre x Rosa-Cas9-GFP mouse. In this antigen-specific model, the P14 TCR recognizes the lymphocytic choriomeningitis virus (LCMV)-derived peptide, gp33 residues 33–41, presented in the context of H-2Db[150]. As anticipated, blocking of PHGDH or SHMT1 impaired the T cell-mediated killing of TNBC, melanoma and lung carcinoma lines (**Figure 19**).

Additional supporting data was obtained by using a previously published T cell dysfunction signature framework[114] to predict the response to immunotherapy in the METABRIC breast cancer public repository. Indeed, the high expression of PHGDH in the cytotoxic T cell subset in breast tumors, correlated to increased patient survival (**Figure 17**). Furthermore, targeting SHMT1/2 for T-cell acute lymphoblastic leukemia therapy highlights the significance of the one-carbon folate pathway in T cells[151].

5.8 Serine/glycine dietary restriction in tumor-bearer mice has a negative impact on the response to checkpoint inhibition

After validating the contribution of the serine-glycine network in T cell function, I studied the impact of serine-glycine deprivation in tumor bearer mice treated with anti-PD1. Notably, the deprivation of serine and glycine from the diet had a detrimental effect on the response to checkpoint blockade. Specifically, animals on serine/glycine free-diet developed larger tumors despite the use of anti-PD1, resulting in poor survival rates compared to animals on a full diet (**Figure 19**). Importantly, the effect of the diet alone did not affect the overall survival of the animals, as both formulations were equicaloric, and serine and glycine can still be synthesized from glucose or glutamine.

In other reports, serine dietary restriction in combination with chemotherapy/ radiotherapy impaired the growth of breast cancer tumors[152,153]. Despite the ability of cancer cells to upregulate serine biosynthesis, DualRP and extensive validation revealed the preferential limitations of serine and glycine in tumor-infiltrating T cells. Collectively, it would be optimal to recognize the crucial role of serine and glycine in T cell activation on cancer patients undergoing immunotherapy.

VI. Conclusions

Triple negative breast cancer (TNBC) represents the most aggressive breast cancer type with reduced targeted therapy options. Fibroblasts and immune cells densely populate the breast tumor microenvironment (TME) and are central players in tumor progression and therapy resistance. Characterizing the interactions in the TME to identify key metabolic vulnerabilities may open new perspectives for TNBC treatment.

In this regard, I explored the use of Dual Ribosome Profiling (DualRP) as a novel approach to elucidate cell interactions and metabolic vulnerabilities in the TME. Compared to the existing techniques that disrupt tumors, or sort the cells for single-cell sequencing applications, DualRP does not expose the cells to additional stress and allows the analysis of metabolic signatures in the naïve state of the TME.

At the first stage of my project, I established DualRP as a robust technique to study fibroblast and breast cancer interactions *in vitro* and *in vivo*. After generating reliable systems of ribosomal fluorescent tagging, the cell-type specific translatomes from the mixed population were retrieved. Here, I found a contribution of type I IFN signaling in alleviating nutrient stress from glucose starvation, occurring uniquely in co-cultured fibroblasts and cancer cells. Interestingly, enhanced type I IFN signaling had an impact in lysosomal activity, and blocking via STAT1 decreased the state of lysosomal proteolysis, suggesting a potential compensatory mechanism. In addition, diricore analysis revealed specific amino acid limitations in alanine and glycine in cancer cells. These limitations were validated on DualRP xenografts, exposing the role of fibroblasts in supporting tumor growth when co-injected with cancer cells.

During the second stage, I focused on the characterization of the immune response with a DualRP-tailored transgenic mouse. With this model I could study the metabolic vulnerabilities of tumors in two dimensions: cancer cells and T cells. More importantly, the metabolic limitations in TNBC tumors after checkpoint inhibition, indicated a high demand of serine and glycine in tumor-infiltrating T cells.

Subsequently, I validated the effect of serine/glycine in T cell function *ex vivo*, demonstrating T cell killing efficiency and that pro-inflammatory cytokine release is significantly improved from increasing serine levels. In line with these observations, the serine/glycine metabolic network was upregulated only in the T cell fraction of tumors after checkpoint inhibition. I then extended the validation to other types of cancer including melanoma and lung cancer and observed upregulation of serine biosynthesis and one carbon metabolism genes in T cells upon co-culture. Given the evident increase in PHGDH and SHMT1 expression in T cells in contact with cancer cells *in vivo* and *in vitro*, I knocked out both genes in T cells what led to the impairment of T cell killing efficiency.

For the last stage, I tested the effect of serine/glycine dietary restriction in combination with immune checkpoint blockade in tumor-bearer mice. Here, serine/glycine withdrawal from the diet had a detrimental effect on tumor clearance in mice receiving anti-PD1. In the past, serine dietary restriction has been shown to improve clinical outcomes in breast cancer patients undergoing chemotherapy and radiotherapy. However, the metabolic demands in the tumor microenvironment, particularly those of T cells, should be carefully considered in patients treated with immune checkpoint blockade.

Altogether, I established a robust approach to study metabolic vulnerabilities in multiple compartments of the TME simultaneously, showing that different cell populations exhibit specific amino acid limitations that could be exploited for therapy. In the future, DualRP has the potential to be applied to more dimensions and to assess other complex intratumor interactions in different types of cancer.

VII. References

1. Łukasiewicz, S. *et al.* Breast Cancer-Epidemiology, Risk Factors, Classification, Prognostic Markers, and Current Treatment Strategies-An Updated Review. *Cancers (Basel).* **13**, (2021).
2. Sung, H. *et al.* Global Cancer Statistics 2020: GLOBOCAN Estimates of Incidence and Mortality Worldwide for 36 Cancers in 185 Countries. *CA. Cancer J. Clin.* **71**, 209–249 (2021).
3. Arnold, M. *et al.* Current and future burden of breast cancer: Global statistics for 2020 and 2040. *The Breast* **66**, 15–23 (2022).
4. Wilkinson, L. & Gathani, T. Understanding breast cancer as a global health concern. *Br. J. Radiol.* **95**, 20211033 (2022).
5. Dai, X. *et al.* Breast cancer intrinsic subtype classification, clinical use and future trends. *Am. J. Cancer Res.* **5**, 2929–2943 (2015).
6. Lüönd, F., Tiede, S. & Christofori, G. Breast cancer as an example of tumour heterogeneity and tumour cell plasticity during malignant progression. *Br. J. Cancer* **125**, 164–175 (2021).
7. Scabia, V. *et al.* Estrogen receptor positive breast cancers have patient specific hormone sensitivities and rely on progesterone receptor. *Nat. Commun.* **13**, 3127 (2022).
8. Tai, W., Mahato, R. & Cheng, K. The role of HER2 in cancer therapy and targeted drug delivery. *J. Control. release Off. J. Control. Release Soc.* **146**, 264–275 (2010).
9. Marra, A., Trapani, D., Viale, G., Criscitiello, C. & Curigliano, G. Practical classification of triple-negative breast cancer: intratumoral heterogeneity, mechanisms of drug resistance, and novel therapies. *npj Breast Cancer* **6**, 54 (2020).
10. Yoder, R. *et al.* Impact of low versus negative estrogen/progesterone receptor status on clinico-pathologic characteristics and survival outcomes in HER2-negative breast cancer. *npj Breast Cancer* **8**, 80 (2022).
11. Santonja, A. *et al.* Triple negative breast cancer subtypes and pathologic complete response rate to neoadjuvant chemotherapy. *Oncotarget* **9**, 26406–26416 (2018).
12. Ensenyat-Mendez, M. *et al.* Current Triple-Negative Breast Cancer Subtypes: Dissecting the Most Aggressive Form of Breast Cancer . *Frontiers in Oncology* **11**, (2021).
13. Lehmann, B. D. *et al.* Refinement of Triple-Negative Breast Cancer Molecular Subtypes: Implications for Neoadjuvant Chemotherapy Selection. *PLoS One* **11**, e0157368 (2016).
14. Lehmann, B. D. *et al.* Identification of human triple-negative breast cancer subtypes and preclinical models for selection of targeted therapies. *J. Clin. Invest.* **121**, 2750–2767 (2011).
15. Metzger-Filho, O. *et al.* Dissecting the Heterogeneity of Triple-Negative Breast

Cancer. *J. Clin. Oncol.* **30**, 1879–1887 (2012).
16. Bianchini, G., De Angelis, C., Licata, L. & Gianni, L. Treatment landscape of triple-negative breast cancer — expanded options, evolving needs. *Nat. Rev. Clin. Oncol.* **19**, 91–113 (2022).
17. den Brok, W. D. *et al.* Homologous Recombination Deficiency in Breast Cancer: A Clinical Review. *JCO Precis. Oncol.* 1–13 (2017). doi:10.1200/PO.16.00031
18. Pascual, J. & Turner, N. C. Targeting the PI3-kinase pathway in triple-negative breast cancer. *Ann. Oncol.* **30**, 1051–1060 (2019).
19. Deepak, K. G. K. *et al.* Tumor microenvironment: Challenges and opportunities in targeting metastasis of triple negative breast cancer. *Pharmacol. Res.* **153**, 104683 (2020).
20. García-Teijido, P., Cabal, M. L., Fernández, I. P. & Pérez, Y. F. Tumor-Infiltrating Lymphocytes in Triple Negative Breast Cancer: The Future of Immune Targeting. *Clin. Med. Insights. Oncol.* **10**, 31–39 (2016).
21. Sharpe, A. H. & Pauken, K. E. The diverse functions of the PD1 inhibitory pathway. *Nat. Rev. Immunol.* **18**, 153–167 (2018).
22. Brown, L. C. & Loi, S. Immune checkpoint inhibition in the treatment of early stage triple negative breast cancer: 2021 update. *Breast* **62 Suppl 1**, S29–S33 (2022).
23. Yi, H. *et al.* Immune Checkpoint Inhibition for Triple-Negative Breast Cancer: Current Landscape and Future Perspectives . *Frontiers in Oncology* **11**, (2021).
24. Li, Y. *et al.* Recent advances in therapeutic strategies for triple-negative breast cancer. *J. Hematol. Oncol.* **15**, 121 (2022).
25. Zheng, H., Siddharth, S., Parida, S., Wu, X. & Sharma, D. Tumor Microenvironment: Key Players in Triple Negative Breast Cancer Immunomodulation. *Cancers (Basel).* **13**, (2021).
26. Ren, X., Kang, B. & Zhang, Z. Understanding tumor ecosystems by single-cell sequencing: promises and limitations. *Genome Biol.* **19**, 211 (2018).
27. Lyssiotis, C. A. & Kimmelman, A. C. Metabolic Interactions in the Tumor Microenvironment. *Trends Cell Biol.* **27**, 863–875 (2017).
28. Baghban, R. *et al.* Tumor microenvironment complexity and therapeutic implications at a glance. *Cell Commun. Signal.* **18**, 59 (2020).
29. Hassan, G. & Seno, M. Blood and Cancer: Cancer Stem Cells as Origin of Hematopoietic Cells in Solid Tumor Microenvironments. *Cells* **9**, (2020).
30. Sahai, E. *et al.* A framework for advancing our understanding of cancer-associated fibroblasts. *Nat. Rev. Cancer* **20**, 174–186 (2020).
31. Anderson, N. M. & Simon, M. C. The tumor microenvironment. *Curr. Biol.* **30**, R921–R925 (2020).
32. Vinogradov, S., Warren, G. & Wei, X. Macrophages associated with tumors as potential targets and therapeutic intermediates. *Nanomedicine (Lond).* **9**, 695–707 (2014).
33. Hanahan, D. & Weinberg, R. A. Hallmarks of Cancer: The Next Generation. *Cell* **144**, 646–674 (2011).

34. Pavlova, N. N. & Thompson, C. B. The Emerging Hallmarks of Cancer Metabolism. *Cell Metab.* **23**, 27–47 (2016).
35. Dong, Y., Tu, R., Liu, H. & Qing, G. Regulation of cancer cell metabolism: oncogenic MYC in the driver's seat. *Signal Transduct. Target. Ther.* **5**, 124 (2020).
36. Hudson, C. C. *et al.* Regulation of hypoxia-inducible factor 1alpha expression and function by the mammalian target of rapamycin. *Mol. Cell. Biol.* **22**, 7004–7014 (2002).
37. Moldogazieva, N. T., Mokhosoev, I. M. & Terentiev, A. A. Metabolic Heterogeneity of Cancer Cells: An Interplay between HIF-1, GLUTs, and AMPK. *Cancers* **12**, (2020).
38. Keerthana, C. K. *et al.* The role of AMPK in cancer metabolism and its impact on the immunomodulation of the tumor microenvironment . *Frontiers in Immunology* **14**, (2023).
39. Zhang, P. *et al.* The role of autophagy in regulating metabolism in the tumor microenvironment. *Genes Dis.* **10**, 447–456 (2023).
40. Mulcahy Levy, J. M. & Thorburn, A. Autophagy in cancer: moving from understanding mechanism to improving therapy responses in patients. *Cell Death Differ.* **27**, 843–857 (2020).
41. Wang, H., Franco, F. & Ho, P.-C. Metabolic Regulation of Tregs in Cancer: Opportunities for Immunotherapy. *Trends in Cancer* **3**, 583–592 (2017).
42. Bader, J. E., Voss, K. & Rathmell, J. C. Targeting Metabolism to Improve the Tumor Microenvironment for Cancer Immunotherapy. *Mol. Cell* **78**, 1019–1033 (2020).
43. Anastasiou, D. Tumour microenvironment factors shaping the cancer metabolism landscape. **116**, 277–286 (2016).
44. Torresano, L., Nuevo-Tapioles, C., Santacatterina, F. & Cuezva, J. M. Metabolic reprogramming and disease progression in cancer patients. *Biochim. Biophys. Acta - Mol. Basis Dis.* **1866**, 165721 (2020).
45. Bott, A. J., Maimouni, S. & Zong, W.-X. The Pleiotropic Effects of Glutamine Metabolism in Cancer. *Cancers (Basel).* **11**, 770 (2019).
46. Vučetić, M., Cormerais, Y., Parks, S. K. & Pouysségur, J. The central role of amino acids in cancer redox homeostasis: Vulnerability points of the cancer redox code. *Front. Oncol.* **7**, (2017).
47. Koundouros, N. & Poulogiannis, G. Reprogramming of fatty acid metabolism in cancer. *Br. J. Cancer* **122**, 4–22 (2020).
48. Liberti, M. V & Locasale, J. W. The Warburg Effect: How Does it Benefit Cancer Cells? *Trends Biochem. Sci.* **41**, 211–218 (2016).
49. Vander Heiden, M. G., Cantley, L. C. & Thompson, C. B. Understanding the Warburg effect: the metabolic requirements of cell proliferation. *Science* **324**, 1029–1033 (2009).
50. Vazquez, A., Liu, J., Zhou, Y. & Oltvai, Z. N. Catabolic efficiency of aerobic glycolysis: the Warburg effect revisited. *BMC Syst. Biol.* **4**, 58 (2010).
51. Chang, C.-H. *et al.* Metabolic Competition in the Tumor Microenvironment Is a

Driver of Cancer Progression. *Cell* **162**, 1229–1241 (2015).
52. Mu, X. *et al.* Tumor-derived lactate induces M2 macrophage polarization via the activation of the ERK/STAT3 signaling pathway in breast cancer. *Cell Cycle* **17**, 428–438 (2018).
53. Snaebjornsson, M. T., Janaki-Raman, S. & Schulze, A. Greasing the Wheels of the Cancer Machine: The Role of Lipid Metabolism in Cancer. *Cell Metab.* **31**, 62–76 (2020).
54. Vasseur, S. & Guillaumond, F. Lipids in cancer: a global view of the contribution of lipid pathways to metastatic formation and treatment resistance. *Oncogenesis* **11**, 46 (2022).
55. Bayerl, F. *et al.* Tumor-derived prostaglandin E2 programs cDC1 dysfunction to impair intratumoral orchestration of anti-cancer T cell responses. *Immunity* **56**, 1341-1358.e11 (2023).
56. Zhang, J., Pavlova, N. N. & Thompson, C. B. Cancer cell metabolism: the essential role of the nonessential amino acid, glutamine. *EMBO J.* **36**, 1302–1315 (2017).
57. Yang, C. *et al.* Glutamine Oxidation Maintains the TCA Cycle and Cell Survival during Impaired Mitochondrial Pyruvate Transport. *Mol. Cell* **56**, 414–424 (2014).
58. Vettore, L., Westbrook, R. L. & Tennant, D. A. New aspects of amino acid metabolism in cancer. *Br. J. Cancer* **122**, 150–156 (2020).
59. Lieu, E. L., Nguyen, T., Rhyne, S. & Kim, J. Amino acids in cancer. *Exp. Mol. Med.* **52**, 15–30 (2020).
60. Patil, M. D., Bhaumik, J., Babykutty, S., Banerjee, U. C. & Fukumura, D. Arginine dependence of tumor cells: targeting a chink in cancer's armor. *Oncogene* **35**, 4957–4972 (2016).
61. Platten, M., Nollen, E. A. A., Röhrig, U. F., Fallarino, F. & Opitz, C. A. Tryptophan metabolism as a common therapeutic target in cancer, neurodegeneration and beyond. *Nat. Rev. Drug Discov.* **18**, 379–401 (2019).
62. Peng, H., Wang, Y. & Luo, W. Multifaceted role of branched-chain amino acid metabolism in cancer. *Oncogene* **39**, 6747–6756 (2020).
63. Gieniec, K. A., Butler, L. M., Worthley, D. L. & Woods, S. L. Cancer-associated fibroblasts—heroes or villains? *Br. J. Cancer* **121**, 293–302 (2019).
64. Glabman, R. A., Choyke, P. L. & Sato, N. Cancer-Associated Fibroblasts: Tumorigenicity and Targeting for Cancer Therapy. *Cancers (Basel).* **14**, (2022).
65. Belhabib, I., Zaghdoudi, S., Lac, C., Bousquet, C. & Jean, C. Extracellular Matrices and Cancer-Associated Fibroblasts: Targets for Cancer Diagnosis and Therapy? *Cancers (Basel).* **13**, (2021).
66. Linares, J., Marín-Jiménez, J. A., Badia-Ramentol, J. & Calon, A. Determinants and Functions of CAFs Secretome During Cancer Progression and Therapy . *Frontiers in Cell and Developmental Biology* **8**, (2021).
67. Li, C., Teixeira, A. F., Zhu, H.-J. & ten Dijke, P. Cancer associated-fibroblast-derived exosomes in cancer progression. *Mol. Cancer* **20**, 154 (2021).
68. Pavlides, S. *et al.* Warburg meets autophagy: cancer-associated fibroblasts

accelerate tumor growth and metastasis via oxidative stress, mitophagy, and aerobic glycolysis. *Antioxid. Redox Signal.* **16**, 1264–1284 (2012).
69. Yan, Y. *et al.* The effects and the mechanisms of autophagy on the cancer-associated fibroblasts in cancer. *J. Exp. Clin. Cancer Res.* **38**, 171 (2019).
70. Pavlides, S. *et al.* The reverse Warburg effect: aerobic glycolysis in cancer associated fibroblasts and the tumor stroma. *Cell Cycle* **8**, 3984–4001 (2009).
71. Pelon, F. *et al.* Cancer-associated fibroblast heterogeneity in axillary lymph nodes drives metastases in breast cancer through complementary mechanisms. *Nat. Commun.* **11**, 404 (2020).
72. Min, K.-W. *et al.* Cancer-associated fibroblasts are associated with poor prognosis in solid type of lung adenocarcinoma in a machine learning analysis. *Sci. Rep.* **11**, 16779 (2021).
73. Monteran, L. & Erez, N. The Dark Side of Fibroblasts: Cancer-Associated Fibroblasts as Mediators of Immunosuppression in the Tumor Microenvironment. *Front. Immunol.* **10**, 1835 (2019).
74. Zhang, C. *et al.* CAFs orchestrates tumor immune microenvironment—A new target in cancer therapy? . *Frontiers in Pharmacology* **14**, (2023).
75. Costa, A. *et al.* Fibroblast Heterogeneity and Immunosuppressive Environment in Human Breast Cancer. *Cancer Cell* **33**, 463-479.e10 (2018).
76. Gok Yavuz, B. *et al.* Cancer associated fibroblasts sculpt tumour microenvironment by recruiting monocytes and inducing immunosuppressive PD-1+ TAMs. *Sci. Rep.* **9**, 3172 (2019).
77. Fu, T. *et al.* Spatial architecture of the immune microenvironment orchestrates tumor immunity and therapeutic response. *J. Hematol. Oncol.* **14**, 98 (2021).
78. Raskov, H., Orhan, A., Christensen, J. P. & Gögenur, I. Cytotoxic CD8+ T cells in cancer and cancer immunotherapy. *Br. J. Cancer* **124**, 359–367 (2021).
79. Yang, Y. *et al.* High intratumoral CD8(+) T-cell infiltration is associated with improved survival in prostate cancer patients undergoing radical prostatectomy. *Prostate* **81**, 20–28 (2021).
80. Liu, S. *et al.* CD8+ lymphocyte infiltration is an independent favorable prognostic indicator in basal-like breast cancer. *Breast Cancer Res.* **14**, R48 (2012).
81. Elkoshi, Z. On the Prognostic Power of Tumor-Infiltrating Lymphocytes – A Critical Commentary . *Frontiers in Immunology* **13**, (2022).
82. Hadrup, S., Donia, M. & Thor Straten, P. Effector CD4 and CD8 T cells and their role in the tumor microenvironment. *Cancer Microenviron. Off. J. Int. Cancer Microenviron. Soc.* **6**, 123–133 (2013).
83. Luckheeram, R. V., Zhou, R., Verma, A. D. & Xia, B. $CD4^+$T cells: differentiation and functions. *Clin. Dev. Immunol.* **2012**, 925135 (2012).
84. Beatty, G. & Paterson, Y. IFN-gamma-dependent inhibition of tumor angiogenesis by tumor-infiltrating CD4+ T cells requires tumor responsiveness to IFN-gamma. *J. Immunol.* **166**, 2276–2282 (2001).
85. Li, C., Jiang, P., Wei, S., Xu, X. & Wang, J. Regulatory T cells in tumor microenvironment: new mechanisms, potential therapeutic strategies and future prospects. *Mol. Cancer* **19**, 116 (2020).

86. Dimeloe, S., Burgener, A.-V., Grählert, J. & Hess, C. T-cell metabolism governing activation, proliferation and differentiation; a modular view. *Immunology* **150**, 35–44 (2017).
87. Jones, N. *et al.* Metabolic Adaptation of Human CD4+ and CD8+ T-Cells to T-Cell Receptor-Mediated Stimulation . *Frontiers in Immunology* **8**, (2017).
88. Liu, S., Liao, S., Liang, L., Deng, J. & Zhou, Y. The relationship between $CD4^+$ T cell glycolysis and their functions. *Trends Endocrinol. Metab.* **34**, 345–360 (2023).
89. Rangel Rivera, G. O. *et al.* Fundamentals of T Cell Metabolism and Strategies to Enhance Cancer Immunotherapy . *Frontiers in Immunology* **12**, (2021).
90. Mafi, S. *et al.* mTOR-Mediated Regulation of Immune Responses in Cancer and Tumor Microenvironment . *Frontiers in Immunology* **12**, (2022).
91. Angelin, A. *et al.* Foxp3 Reprograms T Cell Metabolism to Function in Low-Glucose, High-Lactate Environments. *Cell Metab.* **25**, 1282-1293.e7 (2017).
92. Sosnowska, A. *et al.* Inhibition of arginase modulates T-cell response in the tumor microenvironment of lung carcinoma. *Oncoimmunology* **10**, 1956143 (2021).
93. van Baren, N. & Van den Eynde, B. J. Tryptophan-Degrading Enzymes in Tumoral Immune Resistance . *Frontiers in Immunology* **6**, (2016).
94. Abd El-Fattah, E. E. IDO/kynurenine pathway in cancer: possible therapeutic approaches. *J. Transl. Med.* **20**, 347 (2022).
95. Ingolia, N. T., Brar, G. A., Rouskin, S., McGeachy, A. M. & Weissman, J. S. The ribosome profiling strategy for monitoring translation in vivo by deep sequencing of ribosome-protected mRNA fragments. *Nat. Protoc.* **7**, 1534–1550 (2012).
96. Ingolia, N. T. Ribosome Footprint Profiling of Translation throughout the Genome. *Cell* **165**, 22–33 (2016).
97. Brar, G. A. & Weissman, J. S. Ribosome profiling reveals the what, when, where and how of protein synthesis. *Nat. Rev. Mol. Cell Biol.* **16**, 651–664 (2015).
98. Eastman, G., Smircich, P. & Sotelo-Silveira, J. R. Following Ribosome Footprints to Understand Translation at a Genome Wide Level. *Comput. Struct. Biotechnol. J.* **16**, 167–176 (2018).
99. Gerashchenko, M. V. & Gladyshev, V. N. Ribonuclease selection for ribosome profiling. *Nucleic Acids Res.* **45**, e6 (2017).
100. Heiman, M., Kulicke, R., Fenster, R. J., Greengard, P. & Heintz, N. Cell type–specific mRNA purification by translating ribosome affinity purification (TRAP). *Nat. Protoc.* **9**, 1282–1291 (2014).
101. Sanz, E., Bean, J. C., Carey, D. P., Quintana, A. & McKnight, G. S. RiboTag: Ribosomal Tagging Strategy to Analyze Cell-Type-Specific mRNA Expression In Vivo. *Curr. Protoc. Neurosci.* **88**, e77 (2019).
102. McGlincy, N. J. & Ingolia, N. T. Transcriptome-wide measurement of translation by ribosome profiling. *Methods* **126**, 112–129 (2017).
103. Loayza-Puch, F. *et al.* Tumour-specific proline vulnerability uncovered by differential ribosome codon reading. *Nature* **530**, 490–494 (2016).
104. Loayza-Puch, F. *et al.* TGFbeta1-induced leucine limitation uncovered by

differential ribosome codon reading. *EMBO Rep.* **18**, 549–557 (2017).
105. Kay, E. J. *et al.* Cancer-associated fibroblasts require proline synthesis by PYCR1 for the deposition of pro-tumorigenic extracellular matrix. *Nat. Metab.* **4**, 693–710 (2022).
106. Evers, T. M. J. *et al.* Deciphering Metabolic Heterogeneity by Single-Cell Analysis. *Anal. Chem.* **91**, 13314–13323 (2019).
107. Ahl, P. J. *et al.* Met-Flow, a strategy for single-cell metabolic analysis highlights dynamic changes in immune subpopulations. *Commun. Biol.* **3**, 305 (2020).
108. Hartmann, F. J. *et al.* Single-cell metabolic profiling of human cytotoxic T cells. *Nat. Biotechnol.* **39**, 186–197 (2021).
109. Alseekh, S. *et al.* Mass spectrometry-based metabolomics: a guide for annotation, quantification and best reporting practices. *Nat. Methods* **18**, 747–756 (2021).
110. Koch, B. *et al.* Generation and validation of homozygous fluorescent knock-in cells using CRISPR–Cas9 genome editing. *Nat. Protoc.* **13**, 1465 (2018).
111. Elia, I. *et al.* Tumor cells dictate anti-tumor immune responses by altering pyruvate utilization and succinate signaling in CD8(+) T cells. *Cell Metab.* **34**, 1137-1150.e6 (2022).
112. Guzmán, C., Bagga, M., Kaur, A., Westermarck, J. & Abankwa, D. ColonyArea: An ImageJ Plugin to Automatically Quantify Colony Formation in Clonogenic Assays. *PLoS One* **9**, e92444 (2014).
113. Efremova, M., Vento-Tormo, M., Teichmann, S. A. & Vento-Tormo, R. CellPhoneDB: inferring cell–cell communication from combined expression of multi-subunit ligand–receptor complexes. *Nat. Protoc.* **15**, 1484–1506 (2020).
114. Jiang, P. *et al.* Signatures of T cell dysfunction and exclusion predict cancer immunotherapy response. *Nat. Med.* **24**, 1550–1558 (2018).
115. Yang, H. *et al.* Methods Favoring Homology-Directed Repair Choice in Response to CRISPR/Cas9 Induced-Double Strand Breaks. *Int. J. Mol. Sci.* **21**, (2020).
116. Boelens, M. C. *et al.* Exosome transfer from stromal to breast cancer cells regulates therapy resistance pathways. *Cell* **159**, 499–513 (2014).
117. Broad, R. V *et al.* Inhibition of interferon-signalling halts cancer-associated fibroblast-dependent protection of breast cancer cells from chemotherapy. *Br. J. Cancer* **124**, 1110–1120 (2021).
118. Mustafa, S., Koran, S. & AlOmair, L. Insights Into the Role of Matrix Metalloproteinases in Cancer and its Various Therapeutic Aspects: A Review . *Frontiers in Molecular Biosciences* **9**, (2022).
119. Meurette, O. & Mehlen, P. Review Notch Signaling in the Tumor Microenvironment. *Cancer Cell* **34**, 536–548 (2018).
120. Pohl, S.-G. *et al.* Wnt signaling in triple-negative breast cancer. *Oncogenesis* **6**, e310–e310 (2017).
121. Erez, N., Truitt, M., Olson, P. & Hanahan, D. Cancer-Associated Fibroblasts Are Activated in Incipient Neoplasia to Orchestrate Tumor-Promoting Inflammation in an NF-κB-Dependent Manner. *Cancer Cell* **17**, 135–147 (2010).

122. Apte, R. S., Chen, D. S. & Ferrara, N. VEGF in Signaling and Disease: Beyond Discovery and Development. *Cell* **176**, 1248–1264 (2019).
123. Pakos-Zebrucka, K. *et al.* The integrated stress response. *EMBO Rep.* **17**, 1374–1395 (2016).
124. Zhang, H., Zoued, A., Liu, X., Sit, B. & Waldora, M. K. Type i interferon remodels lysosome function and modifies intestinal epithelial defense. *Proc. Natl. Acad. Sci. U. S. A.* **117**, 29862–29871 (2020).
125. Tian, Y., Wang, M.-L. & Zhao, J. Crosstalk between Autophagy and Type I Interferon Responses in Innate Antiviral Immunity. *Viruses* **11**, (2019).
126. Locasale, J. W. Serine, glycine and one-carbon units: cancer metabolism in full circle. *Nat. Rev. Cancer* **13**, 572–583 (2013).
127. Prochownik, E. V & Wang, H. The Metabolic Fates of Pyruvate in Normal and Neoplastic Cells. *Cells* **10**, (2021).
128. Becker, L. M. *et al.* Epigenetic Reprogramming of Cancer-Associated Fibroblasts Deregulates Glucose Metabolism and Facilitates Progression of Breast Cancer. *Cell Rep.* **31**, 107701 (2020).
129. Sousa, C. M. *et al.* Pancreatic stellate cells support tumour metabolism through autophagic alanine secretion. *Nature* **536**, 479–483 (2016).
130. Luga, V. *et al.* Exosomes mediate stromal mobilization of autocrine Wnt-PCP signaling in breast cancer cell migration. *Cell* **151**, 1542–1556 (2012).
131. Roy, D. G. *et al.* Methionine Metabolism Shapes T Helper Cell Responses through Regulation of Epigenetic Reprogramming. *Cell Metab.* **31**, 250-266.e9 (2020).
132. D'Aniello, C., Patriarca, E. J., Phang, J. M. & Minchiotti, G. Proline Metabolism in Tumor Growth and Metastatic Progression. *Front. Oncol.* **10**, 776 (2020).
133. Wang, W., Cui, J., Ma, H., Lu, W. & Huang, J. Targeting Pyrimidine Metabolism in the Era of Precision Cancer Medicine . *Frontiers in Oncology* **11**, (2021).
134. Wei, Z., Liu, X., Cheng, C., Yu, W. & Yi, P. Metabolism of Amino Acids in Cancer . *Frontiers in Cell and Developmental Biology* **8**, (2021).
135. Jung, M. K., Okekunle, A. P., Lee, J. E., Sung, M. K. & Lim, Y. J. Role of Branched-chain Amino Acid Metabolism in Tumor Development and Progression. *J. cancer Prev.* **26**, 237–243 (2021).
136. Takahara, T., Amemiya, Y., Sugiyama, R., Maki, M. & Shibata, H. Amino acid-dependent control of mTORC1 signaling: a variety of regulatory modes. *J. Biomed. Sci.* **27**, 87 (2020).
137. Chi, R. *et al.* Elevated BCAA Suppresses the Development and Metastasis of Breast Cancer. *Front. Oncol.* **12**, 887257 (2022).
138. Ron-Harel, N. *et al.* T Cell Activation Depends on Extracellular Alanine. *Cell Rep.* **28**, 3011-3021.e4 (2019).
139. Bailis, W. *et al.* Distinct modes of mitochondrial metabolism uncouple T cell differentiation and function. *Nature* **571**, 403–407 (2019).
140. Ma, E. H. *et al.* Serine Is an Essential Metabolite for Effector T Cell Expansion. *Cell Metab.* **25**, 345–357 (2017).
141. Thomas, R., Al-Khadairi, G. & Decock, J. Immune Checkpoint Inhibitors in Triple

Negative Breast Cancer Treatment: Promising Future Prospects . *Frontiers in Oncology* **10**, (2021).
142. Huang, X., Zhang, F., Wang, X. & Liu, K. The Role of Indoleamine 2, 3-Dioxygenase 1 in Regulating Tumor Microenvironment. *Cancers (Basel).* **14**, (2022).
143. Greene, L. I. *et al.* A Role for Tryptophan-2,3-dioxygenase in CD8 T-cell Suppression and Evidence of Tryptophan Catabolism in Breast Cancer Patient Plasma. *Mol. Cancer Res.* **17**, 131 LP – 139 (2019).
144. Pataskar, A. *et al.* Tryptophan depletion results in tryptophan-to-phenylalanine substitutants. *Nature* **603**, 721–727 (2022).
145. Son, S. M. *et al.* Leucine Signals to mTORC1 via Its Metabolite Acetyl-Coenzyme A. *Cell Metab.* **29**, 192-201.e7 (2019).
146. Clarke, S. R. *et al.* Characterization of the ovalbumin-specific TCR transgenic line OT-I: MHC elements for positive and negative selection. *Immunol. Cell Biol.* **78**, 110–117 (2000).
147. Locasale, J. W. *et al.* Phosphoglycerate dehydrogenase diverts glycolytic flux and contributes to oncogenesis. *Nat. Genet.* **43**, 869–874 (2011).
148. Amelio, I., Cutruzzolá, F., Antonov, A., Agostini, M. & Melino, G. Serine and glycine metabolism in cancer. *Trends Biochem. Sci.* **39**, 191–198 (2014).
149. Ducker, G. S. & Rabinowitz, J. D. One-Carbon Metabolism in Health and Disease. *Cell Metab.* **25**, 27–42 (2017).
150. LaFleur, M. W. *et al.* A CRISPR-Cas9 delivery system for in vivo screening of genes in the immune system. *Nat. Commun.* **10**, 1668 (2019).
151. Pikman, Y. *et al.* Targeting serine hydroxymethyltransferases 1 and 2 for T-cell acute lymphoblastic leukemia therapy. *Leukemia* **36**, 348–360 (2022).
152. Maddocks, O. D. K. *et al.* Modulating the therapeutic response of tumours to dietary serine and glycine starvation. *Nature* **544**, 372–376 (2017).
153. Tajan, M. & Vousden, K. H. Dietary Approaches to Cancer Therapy. *Cancer Cell* **37**, 767–785 (2020).

VIII. Supplementary Material

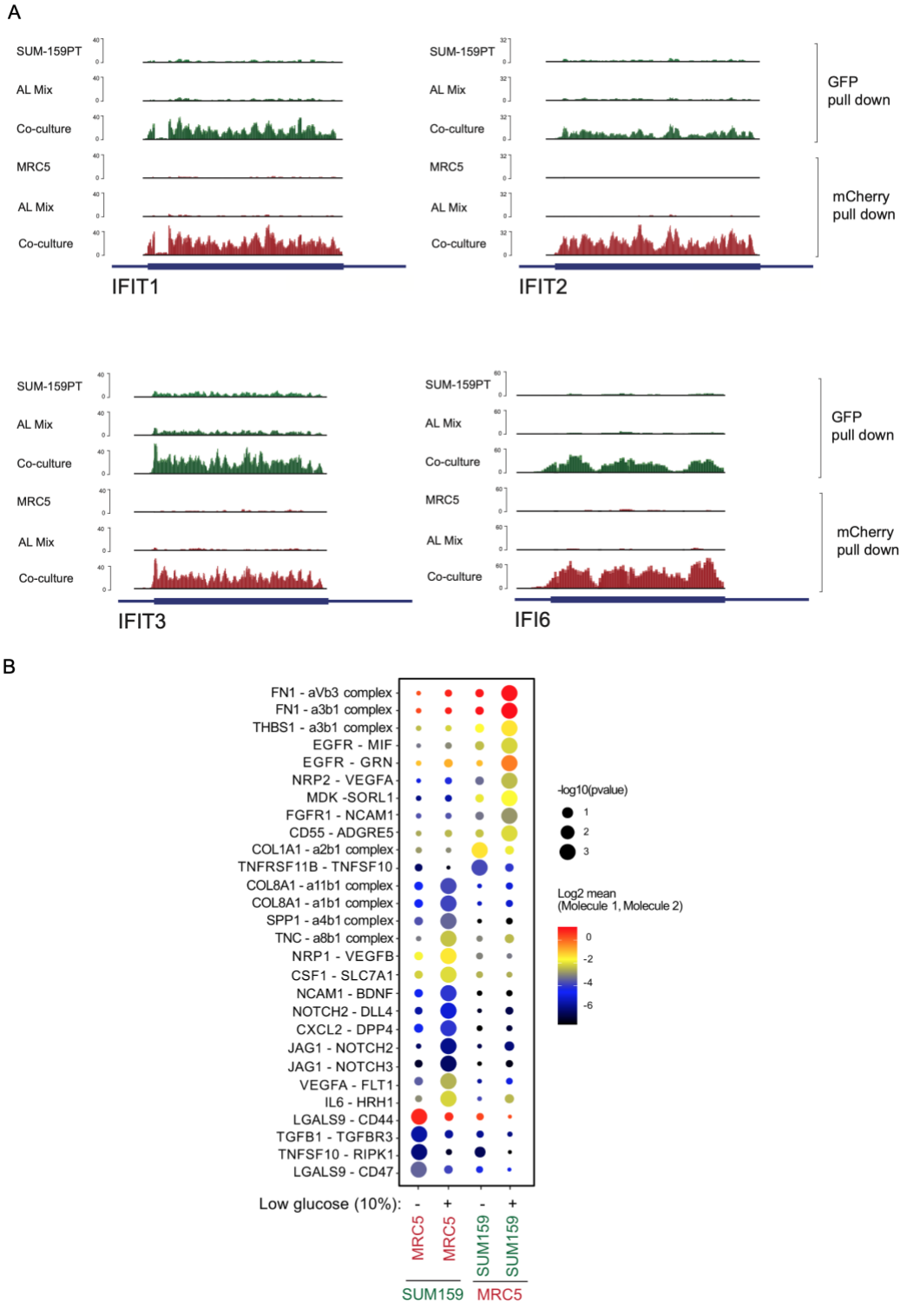

Figure S1 | Landscape of pathway deregulation with DualRP. (**A**) Induction of IFN type I responsive genes is present in co-cultured cancer cell and fibroblasts, but absent in the mixture after lysis (AL Mix). (**B**) Protein-protein interactions detected by CellPhoneDB confirm ECM remodeling, VEGF, NOTCH and IFN signaling activation in co-culture.

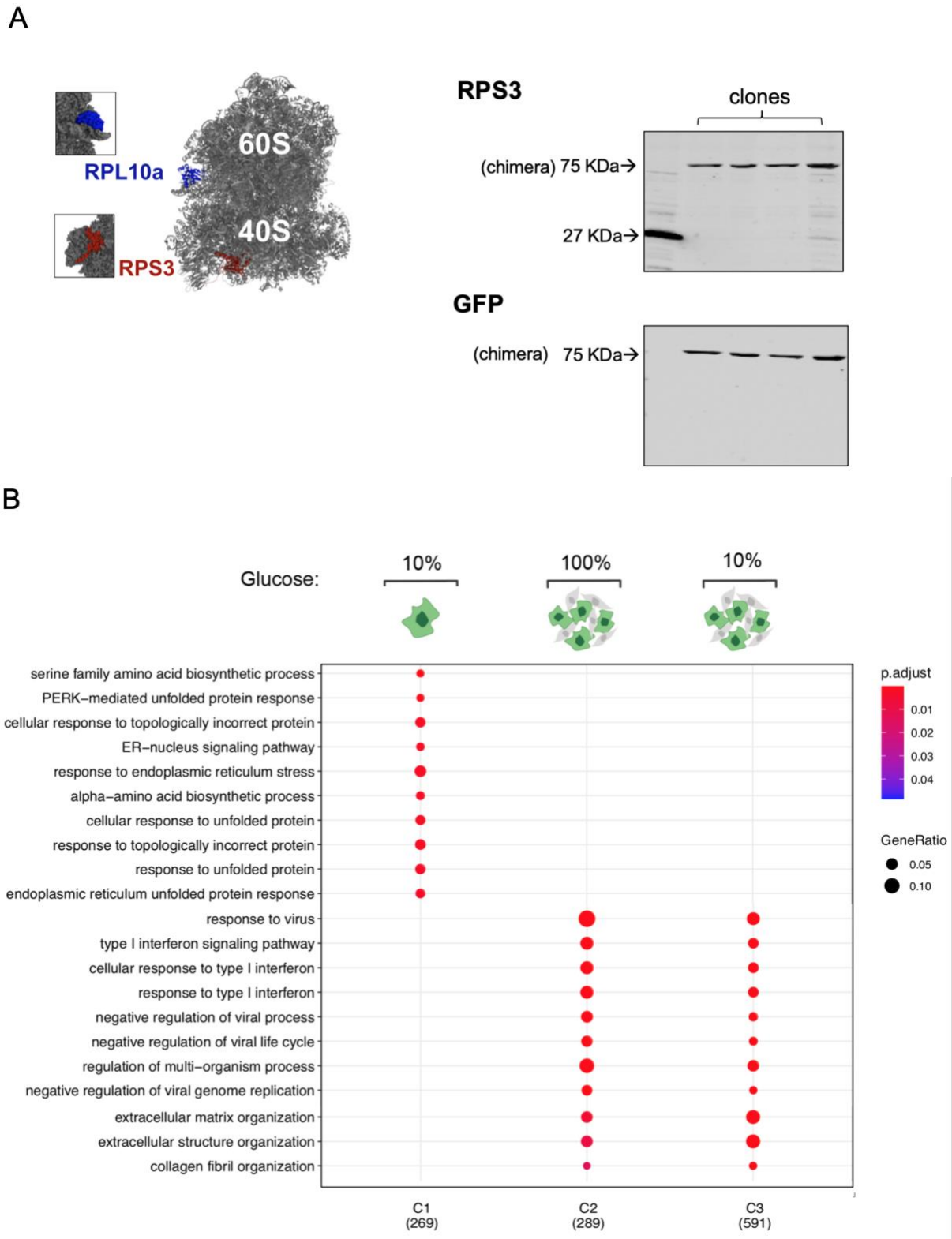

Figure S2 | Endogenous fluorescent tagging on RPS3. (**A**) Tagging of endogenous ribosomal protein S3 on 40S ribosome core and positive clones. (**B**) Pathway upregulation in SUM159-GFP-RPS3 clone co-cultured with fibroblasts. Gene ontology analysis by ClusterProfiler confirms the activation of IFN signaling and rescue of ER-stress under glucose starvation in co-culture. Dot size: number of differentially expressed genes for each pathway (gene ratio). Color: adjusted P value to the set of all family comparisons.

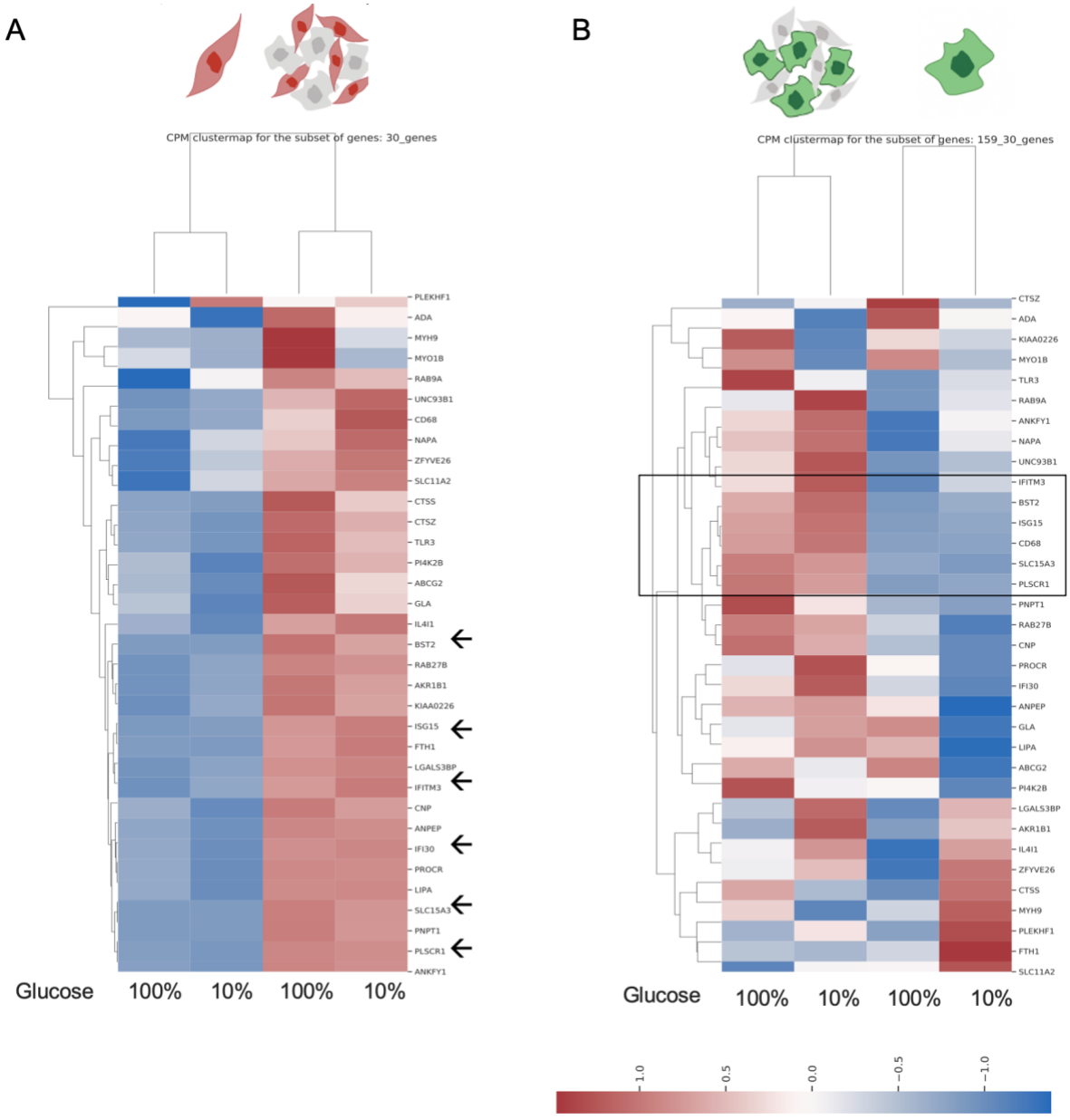

Figure S3 | Activation of IFN-signaling targets linked to lysosomal function. The induction of *ISG15, BST2, PLSCR1, IFI30, SLC15A3* and *IFITM3* is observed in (**A**) fibroblasts and (**B**) breast cancer cells in co-culture independently from glucose concentrations. CPM are represented from a subset of the top 30 genes deregulated in co-culture.

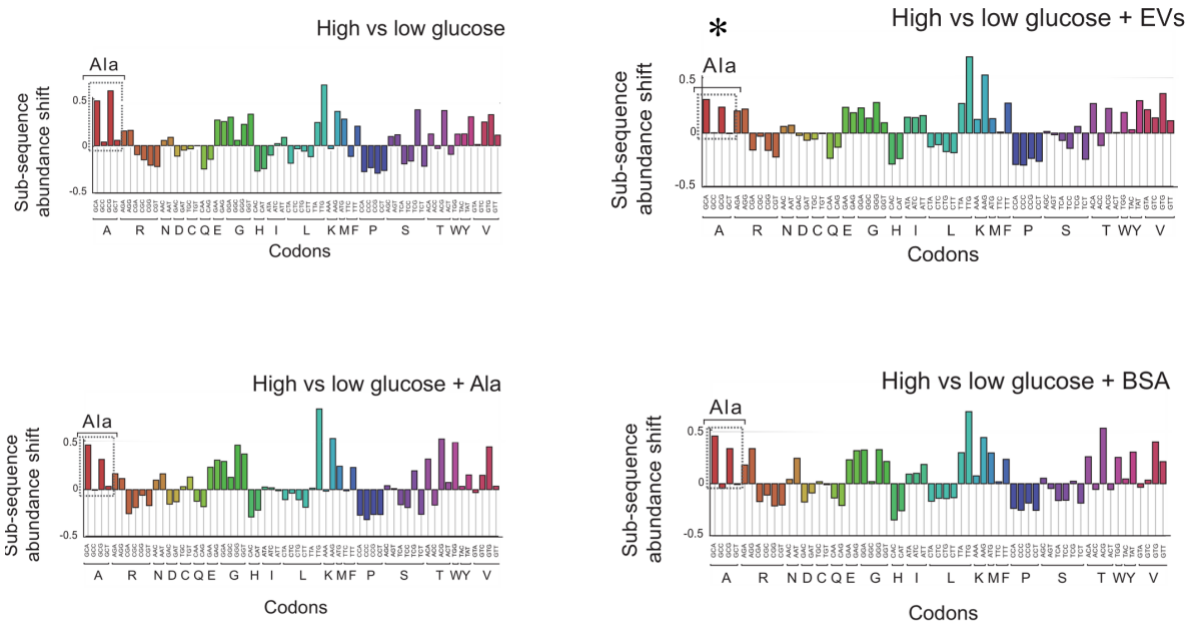

Figure S4 | Alanine limitation in breast cancer cells under glucose starvation. Diricore sub-sequence analysis in glucose-starved SUM159 breast cancer cells. The ribosome stalling in alanine codons (upper left) is not significantly changed after adding alanine (lower left) or extracellular protein like bovine serum albumin (lower right). In contrast, extracellular vesicles from fibroblasts grown under low glucose levels (upper right) decreased the limitation in alanine.

A

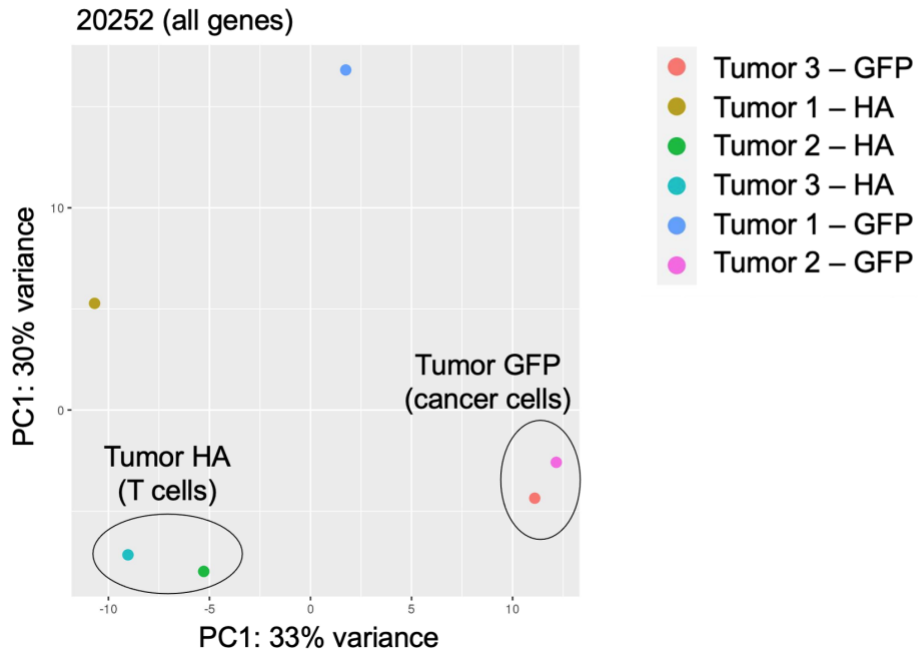

B

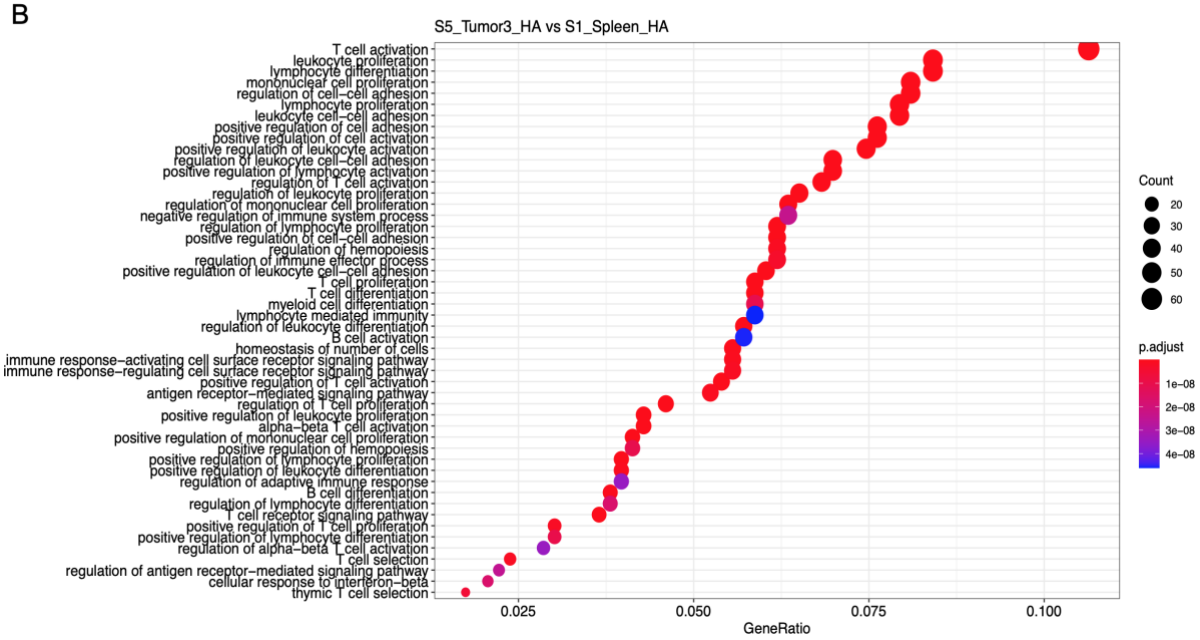

Figure S5 | DualRP detects T cell and breast cancer specific signatures *in vivo*. (**A**) Principal component analysis from TNBC tumors separates the global gene expression of cancer cells and T cells in two independent clusters. (**B**) Downregulation of T cell activation and proliferation signatures in tumor-infiltrating T cells compared to naïve splenocytes. Gene ontology enrichment analysis by ClusterProfiler. Dot size: number of differentially expressed genes for each pathway (gene ratio). Color: adjusted P value to the set of all family comparisons.

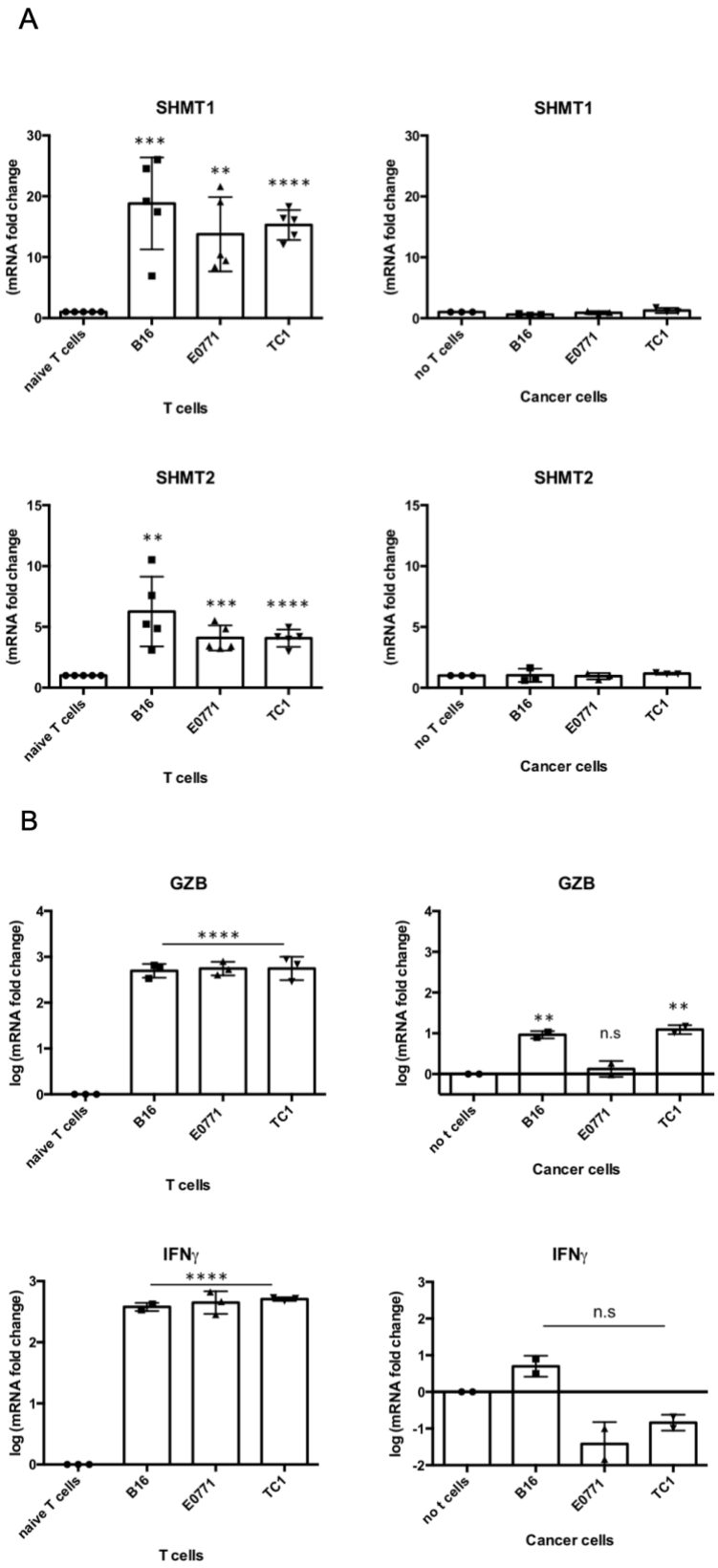

Figure S6 | qPCR analysis from cancer and T cells in co-culture. (**A**) Upregulation of SHMT1 and SHMT2 in activated T cells but not in cancer cells. (**B**) Cytokines associated with T cell activation after co-culture. Fold change is plotted from at least 3 biological replicates. T test parametric analysis calculates statistical significance with P<0.0001 (****), P<0.001 (***) and P< 0.005(**).